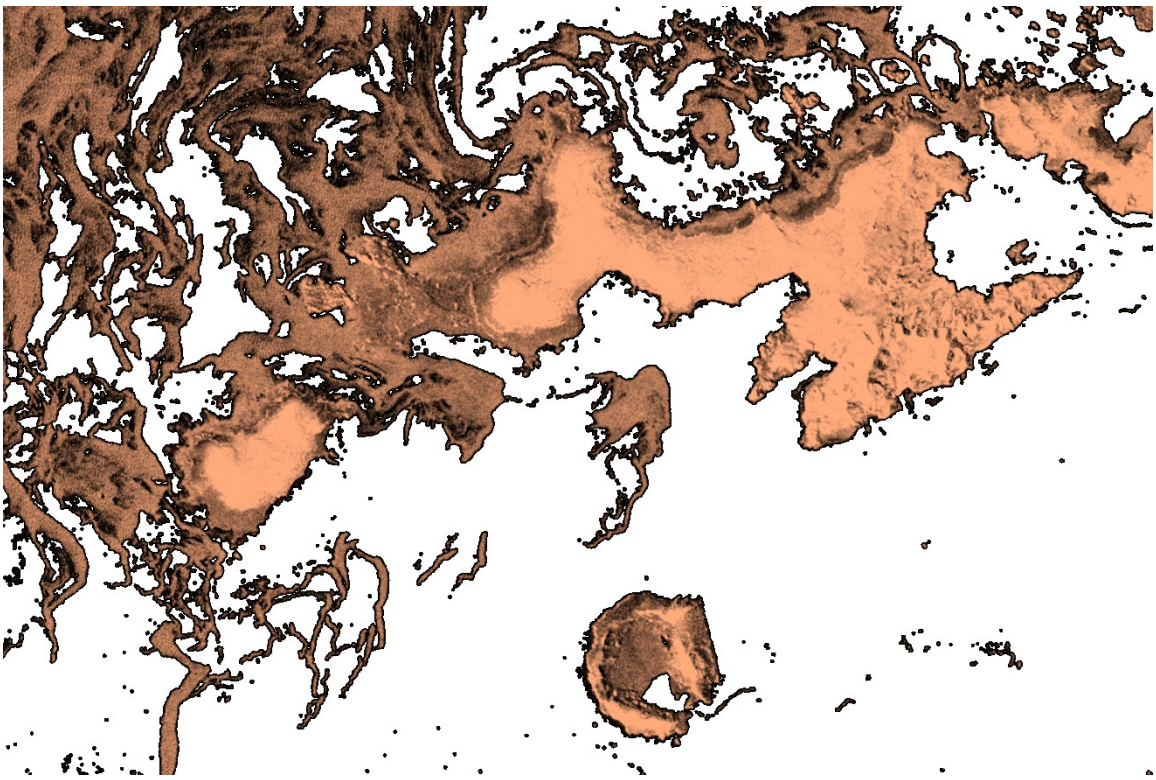


Analysis of the spatio-temporal sea level variability in extreme regions using in-situ and satellite remote sensing data: South Shetland region (Antarctica)

PhD Thesis

Olga Luengo Sánchez

Puerto Real, 2026

Università degli Studi di Ferrara

DOCTORAL COURSE IN

"EARTH AND MARINE SCIENCES (EMAS)"

CYCLE XXXVIII

COORDINATOR Prof. Giuseppe Cruciani

ANALYSIS OF THE SPATIO-TEMPORAL SEA LEVEL VARIABILITY IN EXTREME REGIONS USING IN-SITU AND SATELLITE REMOTE SENSING DATA: SOUTH SHETLAND REGION (ANTARCTICA)

Scientific/Disciplinary Sector: Physical Oceanography

Candidate

Dott. Olga Luengo Sánchez

Supervisor

Prof. Jesús Gómez Enri

Co-Supervisor

Prof. Manuel Berrocoso Domínguez

Year 2022/2025

UNIVERSIDAD DE CÁDIZ

FACULTAD DE CIENCIAS DEL MAR Y AMBIENTALES

DEPARTAMENTO DE FÍSICA APLICADA

ANALYSIS OF THE SPATIO-TEMPORAL SEA LEVEL VARIABILITY IN EXTREME REGIONS USING IN-SITU AND SATELLITE REMOTE SENSING DATA: SOUTH SHETLAND REGION (ANTARCTICA)

Memoria presentada por Olga Luengo Sánchez para optar al grado de Doctor en Ciencias y Tecnologías Marinas – EMAS (Earth and Marine Sciences)

2022/2025

Puerto Real, 2026

Los directores Dr. D. Manuel Berrocoso Domínguez, Catedrático del Departamento de Matemáticas de la Universidad de Cádiz y **Dr. D. Jesús Gómez Enri,** Profesor Titular del Departamento de Física Aplicada de la Universidad de Cádiz,

HACEN CONSTAR:

Que la presente memoria titulada **"Analysis of the spatio-temporal sea level variability in extreme regions using in-situ and satellite remote sensing data: South Shetland region (Antarctica)",** presentada por Olga Luengo Sánchez, resume su trabajo de Tesis, y considerando que reúne todos los requisitos legales, autorizan su presentación y defensa, para optar al Grado de Doctor por la Universidad de Cádiz y la Universidad de Ferrara.

Y para que así conste y surta los efectos oportunos, firman los presentes en Puerto Real (Cádiz) a __ de _____ de dos mil veintiseis.

Dr. D. Manuel Berrocoso Domínguez

Dr. D. Jesús Gómez Enri

This thesis was carried out under the Ph.D. Program: “Earth and Marine Science” run by the University of Cádiz (Spain) and the University of Ferrara (Italy). In addition, this research was supported by two projects: “Monitoring and surveillance of active geodynamic processes using GNSS geodetic deformation in different scenarios (Antarctica, Gulf of Cadiz and Latin America) (2017/2022) (ref.: ctm2017-84210-r) by the Spanish Ministry of Economy, Industry and Competitiveness”; and “Maintenance of geodetic, geothermal and oceanographic time series during the 2016/2017, 2017/2018, 2018/2019, 2019/2020, 2020/2021 and 2021/2022 campaigns (Deception and Livingston Islands, Antarctica) by the Spanish Polar Committee (Spanish Ministry of Science and Innovation). Finally, the research stay at the Institute of Polar Sciences of the National Research Council of Italy (CNR-ISP) was made possible through scholarships provided by the University of Cádiz (Plan Propio) and the University Marine Research Institute (INMAR).

Acknowledgements

Lo único que se puede hacer en la tesis a gusto del consumidor y me veo dudando, ¿será porque me quedan dos neuronas retumbando tras estos tres años? Seguro que sí, ¡vaya panorama ahora que se supone que empiezo una etapa más relajada! :)

Yo que digamos soy una persona con tendencia al habla, sin embargo (howeeever), a la hora de expresar sentimientos en público me puede la vergüenza y me vuelvo más silenciosa. Así que, este el momento de dar las gracias a todos. Podría quedarme aquí, pero no, ¡al lío!

En primer lugar, muchas gracias a mis tutores Manolo y Jesús por los tres años de no parar, esto de hacer tesis en modo rápido agiliza el trámite, pero estresa, y agradezco mucho la paciencia y la ayuda brindada. Muchas gracias Jesús por darme la oportunidad de hacer la tesis, e introducirme en el maravilloso y caótico mundo del EMAS. Y gracias Manolo por siempre tenderme la mano y guiarme a lo largo de estos años en todos los aspectos de esta compleja y bella vida científica. Y por supuesto, muchas gracias a mi tercer tutor, Miki, que, aunque no estés en papeles, desde que llegué al INMAR allá por 2017 me ayudaste y enseñaste.

Gracias a todos los compañeros y amigos que se han visto envueltos en las campañas antárticas tanto desde España como desde el paraíso. Son muchos años de mantenimiento de las series y de trabajo en equipo, así que sin ellos no podríamos haber hecho este trabajo.

Gracias a Amós y Belén por el tiempo, los conocimientos y las risas, tanto en el campo como en el despacho. Gracias a Xavi por la asistencia informática desde hace muchos años. A Vane por ponerle chispa a cualquier asunto y sacar el ojo crítico a pasear cuando hace falta. Y por supuesto, a Enrique, Alejandro y Jorge por la presión a los cafés; a veces una no sabe cuándo poner fin al bucle de Matlab del que no puedes salir.

Grazie ai veneziani, per avermi riportato alla realtà quando pensavo di conoscere l'italiano e mi sono trovata di fronte al meraviglioso mondo della lingua veneta.

Ora sul serio, grazie mille Francesco per avermi accolto a Venezia come se fossi parte della vostra famiglia; e grazie anche a Valentina, Tito e Ana per le lezioni di pizza e le buonissime cenette. Devo confessare ora, davanti a tutti, che la mia pasta madre non è più tra noi…

Grazie a Elisa e Marta per avermi accolto fin dal primo giorno nei caffè quotidiani e per i buoni consigli. Grazie anche a Marco per i consigli sulle Dolomiti. E anche a Fede, Yocelyn, Hamid e Shiva per aver condiviso con me momenti di gioia.

Inoltre, al mio buon padrone di casa Massimiliano per avermi dato la possibilità di stare nel suo bellissimo appartamento che mi ha fatto sentire a casa.

Mil gracias a mis compañeros EMAS, porque, aunque ya son doctores y esto les queda lejos, cuando la burocracia en el mundo italiano se vuelve jeroglífica siempre han estado dispuestos a ayudar.

Gracias por supuesto a mis amigos y doctores premium Juanito y Marinita. Ya desde hace mucho me ayudáis y animáis a seguir en la compleja y a veces desagradecida vida académica. Marina es la mayor organizadora de saraos científicos y encima magnífica profe, no se me ocurría nadie mejor para empezar dando clases. Mi amigo Juanito, conocido por salvarme el culo en ruinas informáticas desde 2018, siempre llega dando unos toques de humor negro, perspectiva y buena crítica.

Desde hace ocho años tengo una amiga que tiene plaza fija porque siempre está, algunos la conocerán como Valle pero en mi casa es más: Lleti, Lletita, Lletuski, Lleta Valleta, Lleta y de vez en cuando Valle. Gracias Lletita, la vida contigo es mejor y más fácil.

También gracias a mi amiga Meri alias piña colada, por ser un ser bueno en un cuerpo tan pequeño (aunque a veces te puede sorprender con el genio de un demonio por alguna causa injusta). Incluso cuando la vida se pone en modo difícil, ahí está la Meri esquivando balazos y dándote abrazos.

Por supuesto, gracias a Isa por fingir tantos años que no sabe jugar al pádel para subirle la autoestima a cualquier contrincante, a Esteli por la alegría a cualquier hora del día, a Alba por ser la cara calmada del grupo (ni confirmo ni desmiento que luego tiene menos vergüenza que Isa incluso) y a jAna Montana por ser entre otras muchas cosas el aire fresco que siempre necesitamos para saber que de la UCA también se sale.

Y a mis amigas de siempre de la uni, Sole, Isa, María y Miriam; y a Mikel. Porque desde hace 15 años (año arriba, año abajo) nos queremos siempre.

Gracias a mis amigos de aquí (porque yo soy gaditana ya después de 15 años), del pueblo, de Fuenla, de Logroño y de todas partes, porque en años donde por logística y lío nos vemos poco siempre los reencuentros son maravillosos. Y a pesar de las chapas cada vez que nos vemos, no han dejado de preguntar por la tesis sabiendo lo que venía después. Uno de mis amigos de aquí es Choco, también conocido por ser entrenador de fútbol (por si algún padre/madre o tutor lee esto), gracias sobre todo por ese tono de voz que se escucha desde Antequera y por ser un gran amigo y mejor compañero de piso.

Paso a mi parte favorita, *la famigliia*, empezando por mis padres, que son los mejores, para mi ¡y para más gente! Son unos motivados de la vida y no hay proyecto que se les escape, y así quieren que nos enfrentemos a la vida mi hermano y yo. A veces más fácil, a veces más difícil, pero siempre nos apoyan. Así que, bendita suerte :) Gracias por todo, por venir hasta Cádiz y ayudarnos, por dar calma y por abrir ventanas a la vida, os quiero mucho.

Gracias a mi hermano, que a pesar de que de entre las ovejas, se considere la más oscura, es a la que más le brilla el pelo. Me gustaría destacar su tranquilidad, la valoro mucho, y por qué os preguntaréis, porque si no seríamos un dúo diabólico. Además de su ser polifacético, a unos niveles que sorprende: te puede hacer una tirolina con una cuerda y una tubería, unas cortinas antivirus, lo que quieras en 3D, unas clases de esgrima o de escalada (correr no le pidas), montar una máquina de corte de piedra, dar formaciones, gestionar personal en los altos hornos y también puede ser el más rápido en Airbus y que eso, por lo que sea, no esté tan bien visto jaja. FLS siempre es un buen ejemplo a seguir, no sigue patrones y eso hace que el resto siempre queramos estar con él.

Mención especial para mi prima HERMANA (léase con la entonación de una niña diminuta llamada María SS), que seguramente sea la persona que, junto a mis padres, más me ha acompañado en todas las etapas de la vida, mil gracias por estar siempre conmigo. Es mejor, y más fácil enfrentarse a la vida con una persona desde que naces, te quiero mucho.

Por supuesto gracias al resto de mi familia, a mis tíos y mis primos ¡que siempre están atentos a las novedades científicas! Y a mí suegrita, por todos los buenos días y por sus ganas de saber inglés para leerse esta tesis.

Para el final dejo lo mejor, mi morrete (HH), también conocido como Viti, Vituki, Vitorino o Víctor vecino. En primer lugar, gracias por las risas de todos los días. La verdad es que es una suerte poder dejar a las neuronas chocar al final del día y que el otro esté igual o incluso peor. La vida se hace más fácil y sobre todo más divertida desde que somos un equipo. Quizá lo más importante a lo largo de una tesis es distraer a un cerebro agobiado y que alguien prácticamente te obligue a salir del ordenador, y ahí nunca fallas. Ya sea con jaleos desde el jardín, las clases de kite, hacer un poco de mezcla, ir a escalar, mover troncos, la extrema urgencia de planear un nuevo proyecto o con cualquier otra cosa, pero siempre con un poquito de esto y un poquito de lo otro para que haya factor sorpresa. Por cosas como estas, y por otras aún más serias, como la paciencia infinita en tiempos complejos y siempre recordarme que el proyecto más valioso ya lo tengo en casa, ¡millones de gracias! Ah, y porque sí, porque te quiero.

Me gustaría terminar recordando que aunque la ciencia dice que uno de cada diez amigos y familiares se leen tus artículos, todos los celebran como si fuesen de Nature.

Por eso y mucho más, ¡muchísimas gracias a toda la gente que quiero y me quiere de una manera u otra! al resto, ¡suerte en la vida que yo tengo mucha!

P.d. Si alguno se atreve a leer la tesis espero que la disfrute.

Table of Contents

List of Figures V

List of abbreviations and acronyms XIII

Summary XVII

Riassunto XIX

Resumen XXI

Thesis outline XXIII

CHAPTER 1 1

Introduction 1

CHAPTER 2 7

Hypothesis and Objectives 7

CHAPTER 3 11

Study Area 11

3.1 Study area 13

3.2 Expanded study area 16

CHAPTER 4 19

Data and Methodology 19

4.1 Data 21

4.1.1 Oceanographic stations 21

4.1.1.1 Antarctic tide gauge stations 21

4.1.1.2 Pacific tide gauge stations 22

4.1.2 Meteorological stations 22

4.1.2.1 In-situ atmospheric temperature 22

4.1.2.2 In-situ atmospheric pressure 23

4.1.3 Reanalysis atmospheric pressure of ERA 5 23

4.1.4 Dynamic Atmospheric Correction (DAC) 24

4.1.5 Satellite altimetry from Sentinel 3A/3B 24
4.1.6 Sentinel-1 SAR images 26
4.2 Methodology for the establishment of the in-situ series 27
4.2.1 Harmonic analysis by least squares fitting and tide prediction 28
4.2.2 Correction of displacements in the records 29
4.2.3 Data validation through harmonic analysis 33
CHAPTER 5 35
Assessment of satellite altimetry accuracy (Sentinel-3A/B) with in-situ sea level data at Livingston Island, Antarctica 35
5.1 Statement of the chapter 37
5.2 Study area 37
5.3 Data 37
5.4 Methodology 37
5.4.1 Altimeter SLA 38
5.4.2 Tide gauge SLA 39
5.4.3 Comparison between series 40
5.5 Results 42
5.5.1 Determination of the optimal altimetric SLA for comparison 42
5.5.2 Validation of SLA time series 44
5.6 Discussion 46
5.7 Conclusions 51
5.8 Connecting text 52
CHAPTER 6 53
Long-term seawater temperature records at Livingston and Deception Islands, Antarctica 53
6.1 Statement of the chapter 55
6.2 Study area 55
6.3 Data 55

6.4 Methodology 56

6.5 Results 57

6.5.1 Temperature time series 57

6.5.2 Statistical description of the series 66

6.6 Discussion 68

6.7 Conclusions 72

6.8 Connecting text 73

CHAPTER 7 75

Meteotsunamis triggered by the Hunga Tonga-Hunga Ha'apai eruption in Livingston and Deception Islands, Antarctica. Aliasing, generation place and importance of the water body geometry in determining their amplitude and time-frequency behaviour 75

7.1 Statement of the chapter 77

7.2 Study area 77

7.3 Data 77

7.4 Methodology 78

7.4.1 Wavelet analysis: Maximum overlap Discrete Wavelet Transform and Continuous Wavelet Transform 78

7.4.2 Assessing the effects of aliasing on the meteotsunami records 79

7.4.3 Computation of the amplification factor by using simulations from a 2D hydrodynamic model 81

7.4.4 Wave refraction maps 82

7.5 Results and discussion 83

7.5.1 Observations of atmospheric pressure and sea level perturbations at Livingston and Deception Islands after the HTHH eruption 83

7.5.2 Origin of the meteotsunamis recorded at Livingston and Deception Islands 88

7.5.3 Analysis of the frequency content characterising the meteotsunami records in LIVMAR and DECMAR 91

7.5.4 Analysis of the three-month record prior to the meteotsunami event 91

7.5.5 Meteotsunami records at LIVMAR and DECMAR 93

7.5.6 Inferring the differences in meteotsunami arrival time between LIVMAR and DECMAR as deduced from numerically-computed long wave refraction map 95

7.6 Conclusions 97

CHAPTER 8 99

Discussion 99

CHAPTER 9 107

Conclusions 107

Future Research Lines 111

References 115

APPENDIXES i

Appendix I iii

Complementary analyses to Chapter 5 iii

Statement of the appendix v

Georeferencing of sea level records v

- Standard methodology v

Alternative tests carried out at CNR-ISP ix

- Test A - Referencing through interannual predictions ix
- Test B - Referencing using DAC series x

Comparative Analysis of SLA from Copernicus and GPOD Altimetry Products xi

Appendix II xiii

Curriculum Vitae xiii

Appendix III xix

Articles already published xix

List of Figures

Figure 3.1 a Antarctic region, simplified bathymetric map and tectonic setting of the region. Morphological features: SSBK (South Shetland Block), SST (South Shetland Trench), BB (Bransfield Basin), HFZ (Hero Fracture Zone), SFZ (Shackleton Fracture Zone). **b** South Shetland Archipelago including: King George, Nelson, Robert, Greenwich, Livingston, Deception, Snow, Low and Smith islands. Submarine volcanoes; Humpback, Three Sisters and Orca. **c** Livingston Island, tide gauge at LIVMAR station at Johnsons Cove (red triangle) and Juan Carlos I Antarctic base with atmospheric station (JCI, green dot). **d** Deception Island, tide gauge at DECMAR station at Colatinas Point (red triangle) and Gabriel de Castilla Antarctic base with atmospheric station (GdC, green dot). 14

Figure 3.2 a Global map of the stations used in this study. Red star denotes the HTHH volcano, while in-situ instruments, including tide gauges and weather stations, are indicated by pink and yellow dots, respectively. **b** Zoom-in with the bathymetry of the study area showing the subduction zone near the South Shetland Islands. **c** Location of tide gauges and meteorological stations in Deception and Livingston islands. The bathymetry is represented in shades of blue, with the lightest tones indicating the shallowest areas and the darkest tones indicating the deepest. Bathymetry derived from the GEBCO 2023 Grid and visualised with QGIS. 17

Figure 4.1 a Pressure tide gauge records of LIVMAR station. **b** Pressure tide gauge records of DECMAR station. Each record spans approximately one year and is identified by a different colour. 22

Figure 4.2 Study area. The green lines represent the ascending and descending orbits of S3B (#0374 and #0109 respectively) and the red lines represent the ascending and descending orbits of S3A (#0317 and #0052 respectively). The location of the tide gauge station (LIVMAR) is marked with a red dot. The map was produced using the Quantarctica package for the Quantum Geographic Information System (QGIS), developed by the Norwegian Polar Institute. 25

Figure 4.3 a Pressure record from Sensor 1 at Livingston Island in 2015. **b** Pressure record from Sensor 2 for the same period. Both series show an identical displacement occurring at the same time, thereby ruling out sensor malfunction as the cause for this campaign. 29

Figure 4.4 Predictions and record superimposed. The dotted line corresponds to the average of the average level of the harmonic analysis (z0 AA) and the discontinued line to the average level of the days before the displacement (z0 days before). 30

Figure 4.5 Predictions and record superimposed of Livingston Island after applying the necessary correction in the presence of displacements. The dotted line corresponds to the average of the average level of the harmonic analysis (z0 AA) and the discontinued line to the average level of the days before the displacement (z0 days before). 31

Figure 4.6 Complete record for Livingston Island after the correction of the displacement present in the 2015 record. 31

Figure 4.7 a Pressure record from the LIVMAR oceanographic station. **b** Tide prediction for the same period, based on harmonic constituents calculated from the observed series. **c** Superposition of the in-situ measurements and the predicted series. 32

Figure 4.8 a Reconstructed sea level time series for the LIVMAR station (2015–2024), compiled from annual datasets. **b** Equivalent reconstruction for the DECMAR station. Each record spans approximately one year and is identified by a different colour. 33

Figure 5.1 Tide records obtained by Eq. (4.2). Each record spans approximately one year and is identified by a different colour. The red line represents the temporal coverage of S3A data and the green line S3B data. 39

Figure 5.2 In-situ dataset filtered with u_tide by removing the tidal contribution from the most significant harmonic constituents of each record, trend and mean sea level. Zoom-in of the **Figure 5.1**, section of the tide gauge record that corresponds to the period of altimeter data. Each colour represents a different year. 40

Figure 5.3 a SDD values for the series obtained by confronting the %SWH and M values for S3A. **b** SDD values for the series obtained by confronting the %SWH and M values for S3B. The M and %SWH combination selected is displayed with a white box. Minimum values of SDD are in dark blue and maximum in red. 43

Figure 5.4 Detrended SLA of the S3A altimeter (red) and tide gauge (blue) after 10 iterations of removing data exceeding ±3σ. The gaps are NaN values that belong to the outliers or missing values. Shaded grey areas correspond to the Antarctic winters. 44

Figure 5.5 Detrended SLA of the S3B altimeter (green) and tide gauge (blue) after 10 iterations of removing data exceeding ±3σ. The gaps are NaN values that belong to the outliers or missing values. Shaded grey areas correspond to the Antarctic winters. 45

Figure 5.6 a SAR image of Livingston Island obtained with Sentinel-1 (04/09/2021). The red line is the descending track #052 of S3A. **b** Zoom-in of the study area. **c** SLA along the study section (Figure 5.6b, red continuous line). Numbers (1, 5 and 16) mark analysed positions. **d** S3A SAR waveforms from Level-1B data. 49

Figure 5.7 a SAR image of Livingston Island obtained with Sentinel-1 (24/09/2020). The green line is the ascending track #374 of S3B. **b** Zoom-in of the study area. **c** SLA along the study section (Figure 5.7b, green continuous line). Numbers (5, 11 and 13) mark analysed positions. **d** S3B SAR waveform from Level-1B data. 50

Figure 6.1 a Air temperature at Livingston Island sampled every 20 min from December 2015 to December 2024 (JCI, blue). **b** Air temperature at Deception Island sampled every 20 min from December 2015 to December 2024 (GdC, red). The gaps in the record are due to missing or anomalous data. 56

Figure 6.2 a Water temperature series at LIVMAR station (blue). **b** Water temperature series at DECMAR station (red), where temperature anomalies are due to volcanic activity. Gaps in the graphs are due to missing data caused by equipment power failures. 58

Figure 6.3 a Water temperature records for the period December 2014 to February 2025 at stations LIVMAR (blue). **b** Water temperature records for the period December 2014 to February 2025 at DECMAR station (red). 59

Figure 6.4 a Maximum water temperature records at LIVMAR (blue) and DECMAR (red) stations during austral summers between December 2014 to February 2023. **b** Water temperature records below -1.8 °C at LIVMAR (blue) and DECMAR (red) stations during austral winters between December 2014 to February 2023. The black dashed line indicates a temperature of -1.8 °C, the freezing point. 60

Figure 6.5 Graphs of austral summers from 2014 to 2025 are presented. The red lines represent the DECMAR station, while the blue lines correspond to the LIVMAR station. The dashed vertical lines mark the start and end of the austral winter (December 21 and March 20, respectively). November and April are also included to show the temperature trends before and after summer. 61

Figure 6.6 Graphs of austral winters from 2015 to 2024 are presented. The red lines represent the DECMAR station, while the blue lines correspond to the LIVMAR station. The shaded grey area highlights temperatures below -1.8°C. The dashed vertical lines mark the start and end of the austral winter (June 22 and September 23, respectively). May and October are also included to show the temperature trends before and after winter. 63

Figure 6.7 Evolution over the years of the number of data in which the temperature record temperatures equal to or below -1.8 °C for each station. LIVMAR station is blue and the DECMAR station is red. From 2021 to 2023 there is no data under -1.8 °C at DECMAR station. 64

Figure 6.8 a Monthly averages of water temperatures from January 2015 to December 2024 at LIVMAR station. The blue shaded area corresponds to the standard deviation. **b** Monthly averages of water temperatures from January 2015 to December 2024 at DECMAR station. The black dashed line indicates a temperature of -1.8 °C, the freezing point. The blue shaded area corresponds to the standard deviation and red line to the mean of all years. 65

Figure 6.9 Monthly mean temperatures superimposed of LIVMAR (blue) and DECMAR (red) stations. 66

Figure 6.10 STL decomposition to DECMAR (red) and LIVMAR (blue) stations. **a** Raw series of seawater temperatures. **b** Trend of the series. **c** Seasonal component of the records. **d** Remainder of the series. 68

Figure 6.11 a Bathymetric map of the Bransfield Strait and circulation pattern as described in Sangrà et al. 2011, Sangrà et al. 2017 and Veny et al. 2022. The bathymetry used is from the International Bathymetric Chart of the Southern Ocean (IBSCO). Green dots are locations of the seismic swarm of 2015 (adapted from Almendros et al., 2018). The white star is the location of Orca volcano and the blue dots are the locations of the earthquakes higher than 4 Mw from United States Geological Survey (USGS) catalog during this period of geodynamic activity. Red triangles are the locations of the oceanographic stations DECMAR and LIVMAR. **b** Sketch profile of the main components of the currents in the Bransfield Strait adapted from Sangrà et al. 2011 and Veny et al. 2022. The acronyms are: TBW (Transitional Bellingshausen Water, red), BC (Bransfield Current), CC (Antarctic Coastal Current), AE (Anticyclonic Eddy), PF (Polar Front), TWW (Transitional Weddel Water, green), SSI (South Shetland Islands) and CDW tongue (Circumpolar Deep Water). 70

Figure 7.1 a b c Scalograms of the 1-minute record of the Old Harbor (a), Nawiliwili (b) and La Jolla (c) stations. White horizontal lines indicate the maximum frequency of the 10-minute scalograms (~2.5 cph). **d e f** Scalograms of the 10-minute record of the Old Harbor (d), Nawiliwili (e) and La Jolla (f) stations. Records start on 14/01/2022 at 18:10 for Nawiliwili and La Jolla, and on 16/01/2022 at 12:40 for Old Harbor. The red vertical line indicates the time of the eruption of the HTHH volcano (15/01/2022 at 04:10 UTC)..... 81

Figure 7.2 Idealised bathymetries used for computing the amplification factors of long waves as a function of the incident long-wave frequency (Figure 7.8). **a** For the water body housing LIVMAR station (Livingston Island). **b** For the water body housing DECMAR station (Deception Island). The open boundaries are identified by a pink line. 82

Figure 7.3 a Time series of atmospheric pressure from JCI station. **b** Time series of atmospheric pressure from GdC station. **c** Bottom pressure from LIVMAR station. **d** Bottom pressure from DECMAR station. The vertical red line indicates the time of the eruption of the HTHH volcano (15/01/2022 at 04:10 UTC). The black arrows mark the points at which anomalies in the records become visually noticeable. The record of JCI is analysed with the one of LIVMAR and the GdC record with the DECMAR record due to the proximity between stations..... 84

Figure 7.4 Wavelet filtered records for January 15 and 16 2022. **a** Filtered atmospheric pressure at JCI station. **b** Filtered atmospheric pressure at GdC station. **c** Filtered atmospheric pressure at LIVMAR station. **d** Filtered atmospheric pressure at DECMAR station. Dashed horizontal lines in 7.4c and 7.4d give the (1-σ) interval. The vertical red line in all the plots indicates the time of the eruption of the Hunga Tonga-Hunga Ha'apai volcano (15/01/2022 - 4:10 UTC). The grey squares indicate the first record associated with the atmospheric perturbation (Figures 7.4a and 7.4b) and grey dots indicate the first record associated with the meteotsunami (Figures 7.4c and 7.4d). The dotted black line indicates the theoretical arrival time for atmospheric pressure waves if the mean propagation velocity is as calculated from all stations used in this article (see **Table 7.1**). Dashed black line indicates the theoretical arrival at the tide gauges if it were a conventional tsunami originating in the trench near HTHH. The record of JCI is analysed with the one of LIVMAR and the GdC record with the DECMAR record due to the proximity between stations. 86

Figure 7.5 Atmospheric pressure filtered data (wavelet-based) recorded at the meteorological stations: Easter Island (blue), JCI (orange), Juan Fernandez Island (yellow), Antofagasta (purple) and GdC (green). Black dots indicate the first (eastward) and second pulse (westward) of the atmospheric perturbation. 87

Figure 7.6 a Ocean wave propagation phase speed map (Mercator projection), showing HTHH volcano (red star), tide gauge and meteorological stations (yellow dots). Black line represents the shortest distance from the HTHH volcano to the JCI station taking into account the curvature of the Earth. **b** Bathymetry profile between HTHH and JCI (black line in Figure 7.6a) for the shortest distance between HTHH volcano and JCI. The mean depth along the line depicting the shortest distance is 4433.63 m. **c** Same as Figure 7.6a for the propagation speed. 90

Figure 7.7 a Scalogram of the 10-minute record of LIVMAR station for the 3-month period. **b** Scalogram of the 10-minute record of DECMAR station for the 3-month period. White area is the cone of influence where the edge effects can distort the results. 92

Figure 7.8 Amplification factors as a function of incident long-wave frequency, for the idealised water bodies housing LIVMAR (dotted line) and DECMAR (solid line) tidal gauge stations (shown in **Figure 7.2**). 93

Figure 7.9 a Scalogram of the 10-minute record of LIVMAR station for the selected period of the HTHH eruption. **b** Scalogram of the 10-minute record of DECMAR station for the selected period of the HTHH eruption. Records begin on 14/01/2022 at 23:20 and the red vertical line indicates the time of the eruption of the HTHH volcano (15/01/2022 at 04:10 UTC). 95

Figure 7.10 Refraction map of a long-wave front entering the western side of the studied region. Front evolution is shown at 6-minute intervals (t). The coastline is indicated by the thick black contour. In addition, some bathymetric contours are presented with thin grey lines and with labels indicating the bottom depth in metres. The two pink dots correspond to the pressure sensors of LIVMAR and DECMAR stations. 96

Figure I.1 Levelling scheme between pressure sensors (Ps1, Ps2 and Auxiliary Ps), Tide Gauge Benchmark (TGBM) and the GPS station. D and D' are the measurements of the pressure sensors; Δn the distance between the TGBM and the GPS station; F is the measure between the Auxiliary Ps and the TGBM, and X is the sum of D, F and Δn. K is the sea level to the ellipsoid. GRS80 is the reference ellipsoid chosen to reference the final records. vi

Figure I. 2 Terrestrial representation surfaces. H represents orthometric height, h represents ellipsoidal height, and N represents the undulation of the geoid. viii

Figure I.3 Sea level records referenced to the GR80 ellipsoid. Each colour represents a different year. The years that appear twice are due to the record being referenced twice, as several measurements were taken of the ellipsoid..... viii

Figure I.4 Sea level series from the tide gauge referenced to the GRS80 ellipsoid. Each colour identifies an annual series..... ix

Figure I.5 Sea Surface Height of LIVMAR station. Each colour represents a different record. x

Figure I.6 DAC correction serie (grey colour) and SLA records (different colours)..... x

List of abbreviations and acronyms

AEMET	Spanish Meteorological Agency
AE	Anticyclonic Eddy system
BAS	British Antarctic Survey
BB	Bransfield Basin
BC	Bransfield Current
CDW	Circumpolar Deep Water
CLS	Collecte Localisation Satellites
CNES	Centre National d'Études Spatiales
CWT	Continuous Wavelet Transform
DAC	Dynamic Atmospheric Correction
DWT	Discrete Wavelet Transform
ECMWF	European Centre for Medium-Range Weather Forecasts
ESA	European Space Agency
EU	European Union
EUMETSAT	European Organisation for the Exploitation of Meteorological Satellites
EW	Extra Wide
FFT	Fast Fourier Transform
GdC	Gabriel de Castilla (AEMET station)
HFZ	Hero Fracture Zone
HH	Horizontal polarisation

HTHH	Hunga Tonga–Hunga Ha'apai
IBSCO	International Bathymetric Chart of the Southern Ocean
IMBIE	Ice Sheet Mass Balance Inter-comparison Exercise team
IPCC	Intergovernmental Panel on Climate Change
JCI	Juan Carlos I (AEMET station)
LAGC	Astronomy, Geodesy and Cartography Laboratory of the University of Cádiz
LEGOS	Laboratoire d'Études en Géophysique et Océanographie Spatiales
MODWT	Maximum Overlap Discrete Wavelet Transform
NOAA	National Oceanic and Atmospheric Administration
PF	Peninsular Front
P-PRO	Earth Console Parallel Processing Service
PSMSL	Permanent Service for Mean Sea Level
QGIS	Quantum Geographic Information System
RMSE	Root Mean Squared Error
SAR	Synthetic Aperture Radar
SAMOSA	SAR Altimetry MOde Studies and Applications
S3A	Sentinel-3A
S3B	Sentinel-3B
SDD	Standard Deviations of Differences
SFZ	Shackleton Fracture Zone
SLA	Sea Level Anomaly

SHOA	Hydrographic and Oceanographic Service of the Chilean Navy
SSI	South Shetland Islands
SRAL	Synthetic Aperture Radar Altimeter
SSB	Sea State Bias
SSBK	South Shetland Block
SST	South Shetland Trench
STL	Seasonal and Trend decomposition procedure based on LOESS
SWH	Significant Wave Height
TBW	Transitional Bellingshausen Water
TGBM	Tide Gauge Benchmark
TWW	Transitional Weddell Water
WCRP	World Climate Research Programme Global Sea Level Budget Group
WMO	World Meteorological Organisation

Summary

This thesis analyses sea level variability in the South Shetland Islands through the integration of satellite altimetry, long-term in-situ oceanographic observations, and the analysis of extreme geophysical events. The study provides new insights into the processes that drive polar coastal environments.

The validation of Sentinel-3A and Sentinel-3B altimetric sea level anomaly products against tide gauge data showed that the agreement between satellite and in-situ measurements was highly sensitive to processing parameters and environmental conditions. Optimised settings, particularly the use of nine surrounding measurements to the crossover and a sea state bias correction of 5% of the significant wave height, yielded the lowest discrepancies with tide gauge records. Sea ice was identified as the main limitation for altimetry in the region, introducing data gaps and contaminating altimeter returns. These results highlight the importance of methodological refinement, including adaptive masking and improved retracking, to increase the robustness of polar altimetry.

Temperature series from LIVMAR (Livingston Island) and DECMAR (Deception Island) stations revealed clear seasonal cycles modulated by local processes. Volcanic and tectonic activity, such as the 2020 Orca seamount activity, were associated with thermal anomalies, while glacier meltwater discharge was linked to earlier and more variable minima at Livingston. Three phases of thermal evolution were identified over the last decade, reflecting the combined effects of regional atmospheric variability and local geophysical forcing.

In addition, the January 2022 Hunga Tonga–Hunga Ha'apai eruption generated atmospheric Lamb waves that were detected at Antarctic meteorological stations and triggered meteotsunamis at Livingston and Deception Islands. The responses at both sites highlight how atmospheric forcing generated long ocean waves that, once established, were shaped by local basin geometry in terms of amplitude and frequency.

Overall, the results demonstrate that sea level variability in the South Shetland Islands is driven by the combined influence of large scale climatic factors, local volcanic and glacial processes, and extreme remote events. By integrating multiple approaches, this thesis contributes to reducing uncertainties in global sea level monitoring and to a more comprehensive understanding of sea level variability in this region of Antarctica.

Riassunto

Questa tesi analizza la variabilità del livello del mare in vicinanza delle Isole South Shetland, attraverso l'integrazione di altimetria satellitare, osservazioni oceanografiche in-situ e l'analisi di eventi geofisici estremi. Lo studio fornisce nuove prospettive sui processi che regolano gli ambienti costieri polari.

La validazione dei prodotti altimetrici di anomalia del livello del mare dei satelliti Sentinel-3A e Sentinel-3B rispetto ai dati mareografici ha mostrato che la concordanza tra le misure satellitari e quelle in-situ è altamente sensibile ai parametri di elaborazione e alle condizioni ambientali. L'ottimizzazione delle impostazioni, in particolare l'utilizzo di nove misure circostanti nei punti di crossover e una correzione del bias per lo stato del mare pari al 5% dell'altezza d'onda significativa, hanno prodotto le discrepanze minori rispetto ai livelli registri dai mareografi. Il ghiaccio marino è stato identificato come la principale limitazione per l'altimetria satellitare nella regione, a causa di lacune nei dati e contaminazione degli echi altimetrici. Questi risultati evidenziano come il perfezionamento metodologico, che comprende l'impiego di tecniche di filtraggio adattativo e algoritmi di retracking avanzati, sia fondamentale per migliorare l'affidabilità delle misure altimetriche in ambiente polare.

Le serie di temperatura delle stazioni mareografiche LIVMAR (Livingston Island) e DECMAR (Deception Island) hanno rivelato cicli stagionali ben definiti, modulati da processi locali. L'attività vulcanica e tettonica, tra cui quella registrata sulla montagna sottomarina Orca nel 2020, è risultata associata ad anomalie termiche, mentre il deflusso di acqua di fusione glaciale è stato collegato a minimi di temperatura più precoci e variabili presso Livingston. Negli ultimi dieci anni sono state identificate tre fasi di evoluzione termica, che riflettono gli effetti combinati della variabilità atmosferica regionale e delle forzanti geofisiche locali.

L'eruzione del vulcano sottomarino Hunga Tonga–Hunga Ha'apai, nel gennaio 2022, d'altra parte ha generato onde atmosferiche di Lamb rilevate anche presso stazioni meteorologiche antartiche, e ha innescato meteotsunami a Livingston e Deception Island. Le risposte osservate in entrambi i siti mostrano come la forzante atmosferica abbia generato onde oceaniche di lungo periodo, modulate dalla geometria locale dei bacini in termini di ampiezza e frequenza.

Nel complesso, la variabilità del livello del mare nelle Isole South Shetland risulta controllata dall'influenza combinata di fattori climatici su larga scala, processi vulcanici e glaciali locali, ed eventi estremi anche remoti. Integrando approcci diversi, il contributo di questo studio aiuta a ridurre le incertezze sul monitoraggio del livello marino a scala globale, e fornisce una più completa comprensione della sua variabilità nella regione antartica presa in esame.

Resumen

Esta tesis analiza la variabilidad del nivel del mar en las islas Shetland del Sur a través de la integración de altimetría satelital, observaciones oceanográficas in-situ y el análisis de eventos geofísicos extremos. El estudio proporciona nuevas perspectivas sobre los procesos que controlan los entornos costeros polares.

La validación de los productos altimétricos de anomalía del nivel del mar de Sentinel-3A y Sentinel-3B frente a los datos de mareógrafos mostró que la concordancia entre las mediciones satelitales e *in situ* es altamente sensible a los parámetros de procesado y a las condiciones ambientales. Los ajustes optimizados, en particular, el uso de nueve mediciones circundantes a los puntos de cruce del altímetro y una corrección del sesgo por estado del mar del 5% de la altura significativa de ola, dieron lugar a las menores discrepancias respecto a los registros mareográficos. El hielo marino fue identificado como la principal limitación para la altimetría en la región, generando lagunas de datos y contaminando el retracking del altímetro. Estos resultados evidencian la necesidad de perfeccionar la metodología, mediante un filtrado adaptativo de los datos y mejoras en los algoritmos de retracking, con el objetivo de aumentar la fiabilidad de la altimetría en regiones polares.

Las series de temperatura de las estaciones LIVMAR (isla Livingston) y DECMAR (isla Decepción) revelaron ciclos estacionales claros modulados por procesos locales. La actividad volcánica y tectónica, como la registrada en el monte submarino Orca en 2020, se asoció a anomalías térmicas, mientras que la descarga de agua de deshielo glaciar estuvo vinculada a temperaturas mínimas más tempranas y variables en Livingston. En la última década se identificaron tres fases de evolución térmica, reflejando los efectos combinados de la variabilidad atmosférica regional y del forzamiento geofísico local.

Asimismo, la erupción del Hunga Tonga–Hunga Ha'apai en enero de 2022 generó ondas de Lamb atmosféricas que fueron detectadas en estaciones meteorológicas antárticas y desencadenaron meteotsunamis en las islas Livingston y Decepción. Las respuestas en ambos emplazamientos evidencian cómo el forzamiento atmosférico generó ondas oceánicas largas que, una vez establecidas, fueron moduladas por la geometría local de las cuencas en términos de amplitud y frecuencia.

En conjunto, los resultados demuestran que la variabilidad del nivel del mar en las islas Shetland del Sur está controlada por la influencia combinada de factores climáticos a gran

escala, procesos volcánicos y glaciares locales, y eventos extremos remotos. Mediante la integración de múltiples enfoques, esta tesis contribuye a reducir las incertidumbres en la monitorización global del nivel del mar, así como una comprensión más integral de la variabilidad del nivel del mar en esta región de la Antártida.

Thesis outline

This thesis is presented as a research work structured into chapters that combine both original content and peer-reviewed scientific articles that have been published. The organisation follows a logical progression from the general context and motivation of the study to the research outcomes, their discussion, and the final conclusions.

- Chapter 1. Introduction

The first chapter provides a general background on the main topics addressed in this thesis and establishes the overall framework of the research, contextualising the scientific motivation.

- Chapter 2. Hypothesis and objectives

Chapter 2 defines the central hypotheses of the thesis and the specific objectives that guide the research.

- Chapter 3. Study area

This chapter describes the geographical and scientific context of the Bransfield Strait, with a focus on Livingston and Deception Islands, and extends to the Pacific region in relation to the Hunga Tonga–Hunga Ha'apai eruption.

- Chapter 4. Data and Methods

Chapter 4 outlines the datasets used, the instrumentation, and the common methodologies applied across the main chapters to establish the series.

- Chapter 5. Assessment of Satellite Altimetry Accuracy (Sentinel-3A/B) with In-Situ Sea Level Data at Livingston Island, Antarctica. Luengo-S, O., De Biasio, F., Bruno, M., Vignudelli, S., Berrocoso, M., & Gómez-Enri, J. (2025). *Advances in Space Research.* https://doi.org/10.1016/j.asr.2025.12.088

This chapter evaluates the performance of Sentinel-3A/B altimetry in Antarctica by comparing nearly a decade of in-situ sea level records with satellite measurements.

- Chapter 6. Long-term seawater temperature records at Livingston and Deception Islands, Antarctica. Luengo-S, O., Rosado, B., Jiménez-Morales, V., De Gil, A., Gómez-Enri, J., Bruno, M., & Berrocoso, M. (2025). *Frontiers In Marine Science*, *12*. https://doi.org/10.3389/fmars.2025.1566852

Motivated by the sensitivity of altimetry to sea ice conditions identified in Chapter 5, this chapter examines the long-term seawater temperature series from both stations to characterise the seasonal thermal cycle, interannual variability, and the temperature thresholds associated with sea-ice formation.

- Chapter 7. Meteotsunamis triggered by the Hunga Tonga-Hunga Ha'apai eruption in Livingston and Deception Islands, Antarctica. Aliasing, generation place and importance of the water body geometry in determining their amplitude and time-frequency behaviour. Luengo-S, O., Bruno, M., Gómez-Enri, J., & Berrocoso, M. (2025). *Bulletin Of Volcanology*, *87*(6). https://doi.org/10.1007/s00445-025-01831-2

Following the analysis of long-term environmental variability in Chapter 6, Chapter 7 examines the impact of short-term extreme events, focusing on the meteotsunami generated by the Hunga Tonga-Hunga Ha'apai eruption.

- Chapter 8. Discussion

This chapter discusses the results and integrates the findings from the previous chapters, highlighting the original contributions, limitations, and the interconnections among them.

- Chapter 9. Conclusions

The main conclusions of the thesis, summarising them in relation to the stated hypotheses and objectives are described in this chapter.

- Future Research Lines

This section outlines possible approaches for future research, methodological improvements and interdisciplinary collaborations aimed at improving understanding of sea level variability in the South Shetland Islands.

Lastly, the **References** cited throughout the thesis are presented at the end of the manuscript, together with the **Appendixes**, which include additional methodologies, the author's curriculum vitae, and the published articles.

CHAPTER 1

Introduction

Observations of sea level change are essential for evaluating trends related to global warming, improving our understanding of the climate system, and validating global climate models (Cazenave & Remy, 2011; Leuliette et al., 2004; Meyssignac et al., 2023).

Since the early 1990s, satellite altimeters have measured sea level with high precision, with the current estimate of a global average rise rate of approximately 3.3 mm per year based on these long-term observations (Beckley et al., 2017; Hamlington et al., 2024; Meyssignac et al., 2023; Nerem et al., 2018; Nerem & Mitchum, 2001; WCRP Global Sea Level Budget Group, 2018), although regional variations exist. Satellite radar altimetry has demonstrated its effectiveness in providing high-quality global sea level data, in both offshore and coastal zones (Mostafavi et al., 2021; WCRP Global Sea Level Budget Group, 2018). In coastal regions, significant progress has been made in recent years (Benveniste et al., 2019), although further improvements are still required (Vignudelli et al., 2019).

Multiple studies assess the accuracy of altimetry measurements in coastal regions by comparing them with in-situ sea level data from tide gauges (Dieng et al., 2021; Fenoglio-Marc et al., 2015; Y. Fu et al., 2021; Gómez-Enri et al., 2018; Peng et al., 2024; Pham et al., 2024; R. D. Ray et al., 2023; Valle-Rodríguez et al., 2023). Sea level variability is typically examined using Sea Level Anomaly (SLA) relative to a mean sea surface, with tidal, sea state, and atmospheric components filtered out (Laignel et al., 2023). Despite these efforts, comparing the two instruments remains a challenge (Oreiro et al., 2014). This issue becomes especially critical in remote and data-scarce regions, such as Antarctica, where assessing the consistency and limitations of available data sets is essential in order to improve our understanding of regional sea level trends and their implications for the global climate system (Bruni et al., 2022; Ray et al., 2021).

Due to its importance, Antarctica has received growing attention, as changes in its ice and sea level help reveal how sea level is evolving (Church et al., 2013; Galassi & Spada, 2017) and the subsequent impact on ocean circulation (Armitage et al., 2018; Zhou et al., 2020). The Antarctic ice sheet is an important indicator of climate change and driver of sea level rise (The IMBIE team, 2018). Using satellite data, some authors indicate that the Antarctic ice melt has raised sea levels by 7.4 mm since 1992 (Alevropoulos-Borrill et al., 2024; ESA, 2023; Intergovernmental Panel on Climate Change (IPCC), 2023). Most of the altimetric studies in polar regions are focused on monitoring sea ice variations (Auger et al., 2022; Dotto et al., 2018; Garnier et al., 2022), and in turn the ability to determine water level in the Arctic and Antarctic seas is hampered by the frequent presence of sea ice (Andersen et al., 2019; Armitage et al., 2016; Prandi et al., 2012; Rye et al., 2014). However, despite the

difficulties caused by ice, studies on sea level have been published (Armitage et al., 2016; Auger et al., 2022; Bulczak et al., 2015; Lawrence et al., 2021). Furthermore, artificial intelligence has recently been used to classify ice and determine ice-free areas in order to identify sea-ice leads and measure the sea level in those locations (Mugunthan et al., 2023; Passaro et al., 2021).

Sea level records in Antarctica are both valuable and scarce due to the extreme conditions and the challenges of maintaining measurement stations in the region. When discussing long-term time series, the complexity of data collection increases and is especially true regarding in-situ data acquisition during the austral winter, when changing sea ice and reduced daylight hours hinder operations (Passaro et al., 2021; Venables et al., 2023). Therefore, conducting observations throughout the year is of significant scientific importance. Some of the longer Antarctic tide gauge sea level series are available at the repository of the Permanent Service for Mean Sea Level (PSMSL). However, these have cut-offs and are only available on a monthly basis. The most recent ones belong to the British Antarctic Survey (BAS; Rothera and Faraday Antarctic stations) and the Hydrographic and Oceanographic Service of the Chilean Navy (SHOA; Prat Antarctic station). The data are available through the UHSLC Legacy Data Portal (UHSLC, n.d.).

Oceanographic data in Antarctica are limited in number and temporal coverage, but remain essential for investigating the processes that govern sea level variability. Among the most influential of these processes are oceanic and atmospheric temperature changes, which strongly affect sea ice dynamics and freshwater input from glacial melt. In this context, the Southern Ocean has undergone significant changes in recent decades, resulting in major impacts on global climate. It has absorbed a large amount of climate change-related heat, which has been transferred from the atmosphere and stored in its subsurface water masses (Auger et al., 2021; Frölicher et al., 2015; IPCC, 2022). The western Antarctic Peninsula is a warming spot in Antarctica (Jones et al., 2016; Vorrath et al., 2020), experiencing a rise in atmospheric temperature of 0.54 °C during the 20th century (Steig et al., 2009; Turner et al., 2005; Vaughan et al., 2003) and a minor cooling trend from 2000 to 2010 (Carrasco et al., 2021; Turner et al., 2020). Additionally, between the 1990s and the 2000s, subsurface temperatures in various water bodies around the western Antarctic peninsula experienced an increase of up to 1 °C (Cook et al., 2016).

Sea ice forms during the winter, but its presence and persistence can vary according to changes in air temperature and the strength and direction of the wind (Venables et al., 2023).

One of the conditions for the generation of the sea ice is water temperature; freezing point of surface water in these polar waters is considered to be around -1.9 °C (Damini et al., 2022; Hofmann et al., 1996; Hunt et al., 2003; Jacobs et al., 1992; Joughin & Padman, 2003). The freezing point of water is a function of salinity, thus the input of glacial ice melt will act to influence further sea ice production (Meredith et al., 2008). In addition, it is pressure-dependent, freezing point decreases with increasing pressure (Foldvik & Kvinge, 1974).

While sea level variability in Antarctica is largely controlled by processes such as glacial melt, sea ice formation and temperature fluctuations, it can also be modulated by short-term, high-frequency atmospheric disturbances. Among these, violent explosive eruptions trigger significant compression waves in the atmosphere, detectable through atmospheric pressure variations. Such atmospheric disturbances can generate tsunamis, widely known as meteotsunamis (Defant, 1961; Nomitsu, 1935; Omira et al., 2022; Rabinovich & Monserrat, 1998; Saito et al., 2021). When these disturbances are produced by volcanic eruptions, they are commonly referred to as volcano-meteorological tsunamis (Paris, 2015; Tahira et al., 1996).

The most accepted mechanisms to explain the generation of meteotsunamis in the open sea are based on two main factors: (i) The generation of a small sea surface wave by inverse barometer response of the ocean to the leading (and more energetic) atmospheric pressure front; and (ii) The non-linear energy transfer to the previously created sea surface wave from the less energetic secondary atmospheric pressure waves, moving behind the leading wave (Harkrider & Press, 1967; Omira et al., 2022). It is also known that this energy transfer is maximised when the propagation speed of the atmospheric disturbance matches the propagation speed of the sea surface long waves, giving place to the occurrence of the Proudman resonance (Proudman, 1929) and the subsequent amplification of the sea surface waves while they propagate out from the generation region. Once generated in the open ocean, meteotsunamis may experience further amplification as they propagate across continental slopes and shelves, especially in coastal embayments or harbours with geometries favourable for resonance (M. S. Kim et al., 2021; Monserrat et al., 2006; Rabinovich, 2009).

The largest meteotsunami ever recorded was generated by the 1883 Krakatoa eruption, although the scarcity of observational instruments at the time prevented a detailed global analysis (Harkrider & Press, 1967; Latter, 1981; Satake et al., 2020). In contrast, recent technological advances and a much denser instrumentation throughout the world oceans

have made a deeper analysis of the effects of the eruption of the Hunga Tonga-Hunga Ha'apai volcano (HTHH) possible by using tide gauges, seismographs, barometers and DART buoys (Anup et al., 2024; Heidarzadeh et al., 2022; Matoza et al., 2022; Ramírez-Herrera et al., 2022; Ren et al., 2023).

Acoustic-gravity waves (Lamb waves; Lamb, 1932) propagate horizontally in the atmosphere and are expected to transfer energy to the ocean over large distances (Amores et al., 2022; Wang et al., 2022). These atmospheric waves might suffer significant modifications due to the meteorological conditions (temperature and wind) affecting their magnitude (Lacanna & Ripepe, 2013) and under standard conditions they travel at speeds of about ~310 m/s (Harkrider & Press, 1967; Harrison, 2022; Heidarzadeh et al., 2022; Kataoka et al., 2022). This is slightly slower than the speed of sound at ground level and might fade over long distances (Kataoka et al., 2022; Nishida et al., 2014). As mentioned, Lamb waves generally move significantly faster than long oceanic waves. The speed of the latter mainly depends on water depth and typically reaches about 200 m/s in the deep ocean (Kasahara, 1977). The character and strength of the resonance is related to the Froude number (Fr), defined as the ratio between the propagation speed of the atmospheric disturbance (U) and that of the ocean waves (c). When Fr approaches unity, the so-called Proudman resonance occurs (Monserrat et al., 2006; Vilibić, 2008), enabling efficient energy transfer from the atmosphere to the ocean. In this context, atmospheric disturbances can transfer energy that amplifies ocean waves by several orders of magnitude compared to the inverse barometer response (Vilibić, 2008). There are several works where significant meteotsunamis generated in the HTHH volcanic explosion are travelling with the same propagation speed as the Lamb wave even when the long wave propagation velocity c is quite lesser than that of the atmospheric wave (Anup et al., 2024; Tonegawa & Fukao, 2022; Yamada et al., 2022). In addition, Omira et al. (2022) report that the meteotsunamis generated by the leading front of the atmospheric disturbance can be amplified by the energy transference from the secondary atmospheric disturbance that follows the leading front. In this case, the Proudman resonance is not required, although the secondary disturbances must propagate at slower speeds than the leading front. This resonance mechanism is somewhat more complex since it involves a triad of interacting waves; a sea level disturbance moving in the same direction as the leading atmospheric disturbance, a sea level disturbance moving in the opposite direction and the secondary atmospheric disturbance (Kadri & Akylas, 2016).

CHAPTER 2

Hypothesis and Objectives

This thesis hypothesizes that sea level variability around Deception and Livingston Islands (Antarctica) is strongly influenced by a combination of extreme environmental conditions, including sea ice formation, volcanic activity, atmospheric pressure fluctuations, and changes in both surface and deep circulation patterns in the adjacent areas. Satellite altimetry (Sentinel-3A/B), when appropriately corrected, can provide reliable sea level measurements in polar regions, allowing for direct comparison with in-situ tide gauge records. Furthermore, it is hypothesized that sea ice formation in the South Shetland Islands is tightly coupled with surface water temperature thresholds. Finally, that volcanic events, both local and remote, can trigger transient phenomena such as meteotsunamis, detectable through high-resolution sea level records.

The main objective of this thesis is to analyse the spatial and temporal variability of sea level in the vicinity of Deception and Livingston Islands, using both in-situ and satellite observations. Emphasis is placed on the influence of extreme conditions such as sea ice dynamics, volcanic activity, and atmospheric pressure on sea level signals.

To achieve this goal, the following specific objectives have been defined:

i. **To establish long-term sea level time series** using in-situ tide gauge data, incorporating corrections for jumps introduced by extreme environmental conditions, such as sea ice coverage, and local volcanic effects.

ii. **To evaluate the accuracy of satellite altimetry products (Sentinel-3A/B)** in polar coastal regions by comparing them with in-situ measurements optimizing correction parameters for high-latitude conditions.

iii. **To evaluate the quality of altimeter measurements** data derived from Sentinel-3 altimetry in the South Shetland Islands as a function of sea ice presence. This assessment was supported by the visual inspection of Sentinel-1 SAR imagery to delineate sea ice extent and by the analysis of Sentinel-3 altimetry waveforms to characterise surface conditions.

iv. **To analyse the long-term seawater temperature records** at Livingston and Deception stations, identifying trends, seasonality, and interannual variability, and to assess the influence of both local factors (e.g., volcanic activity) and regional climatic processes on the marine thermal dynamics.

v. **To assess the influence of volcanic activity (both local and remote)** on sea level variability, with particular attention to the detection of meteotsunamis using high-frequency tide gauge records.

The outcomes of this research will contribute to an improved understanding of polar sea level dynamics and support the validation of satellite altimetry in extreme environments, with implications for climate monitoring and geophysical hazard assessment in Antarctic regions.

CHAPTER 3

Study Area

3.1 Study area

The study focuses on the Bransfield Strait, where Deception and Livingston Islands are located. These islands host the two Spanish Antarctic Research Stations, Juan Carlos I on Livingston Island and Gabriel de Castilla on Deception Island, established there due to their strategic location and exceptional geodynamic characteristics.

The South Shetland archipelago is located in the Bransfield Strait, about 100 km away from the Antarctic Peninsula. This region is considered a highly geodynamical complex area due to the interaction of several tectonic plates; two major ones: The South American plate and Antarctic plate; and three microplates: Scotia, Phoenix and South Shetland (Baraldo, 1999; Bohoyo et al., 2002; González-Casado et al., 2000; Henriet et al., 1992; L. A. Lawrence et al., 1997; Ramírez, 2007). The central Bransfield Basin has a tectonic configuration associated with active subduction and an expansive back-arc center forming a NE-SW-axis spreading rift (**Figure 3.1a**) (Barker & Austin, 1998; Barker, 1982; Grad et al., 1992; Martí et al., 2013). Besides, it is characterised by the presence of active volcanism with emerging volcanoes (Deception, Penguin and Bridgeman; Smellie et al., 1990); and numerous submarine volcanic edifices which can be seen in **Figure 3.1b** (Orca, Three Sisters etc; Almendros et al., 2020; Barker & Austin, 1998; Dählmann et al., 2001).

Livingston Island is the second largest island of the South Shetland Islands (**Figure 3.1b** and **Figure 3.1c**); it has a surface area of 974 km^2. The island is covered with glaciers and ice caps, with approximately 90% of its surface permanently covered by ice, and only the west side and some coastal areas are snow-free in the summer (Calleja et al., 2019; Recondo et al., 2022; Sugiyama et al., 2019). In one of these ice-free areas, called the Hurd Peninsula (Sugiyama et al., 2019), the Juan Carlos I base is located. Johnson Cove Bay, according to Vidal et al. (2012), has salinity values around 33.5 psu.

Deception Island is a horseshoe-shaped active volcano located in the southern limit of the Bransfield Basin (**Figure 3.1d**). It has a central flooded caldera, Port Foster, which opens onto Bransfield Strait through a shallow and narrow sill called Neptune Bellows (K. L. Smith et al., 2003). The Spanish Antarctic base Gabriel de Castilla is located on the western inner shore of Port Foster. Volcanic activity on the island has been documented in three eruptive phases over the last two centuries (1818-1828, 1906-1912 and 1967-1970) and has been monitored by geophysical and geodetic techniques (Jiménez-Morales et al., 2022; Rosado et al., 2019; Smellie, 2001). At the surface, the main indicators of current volcanic activity are the existence of fumarolic areas and thermal springs (Berrocoso et al., 2018). Despite this, about 57% of the island's land surface is currently covered by ice (Smith, 2005).

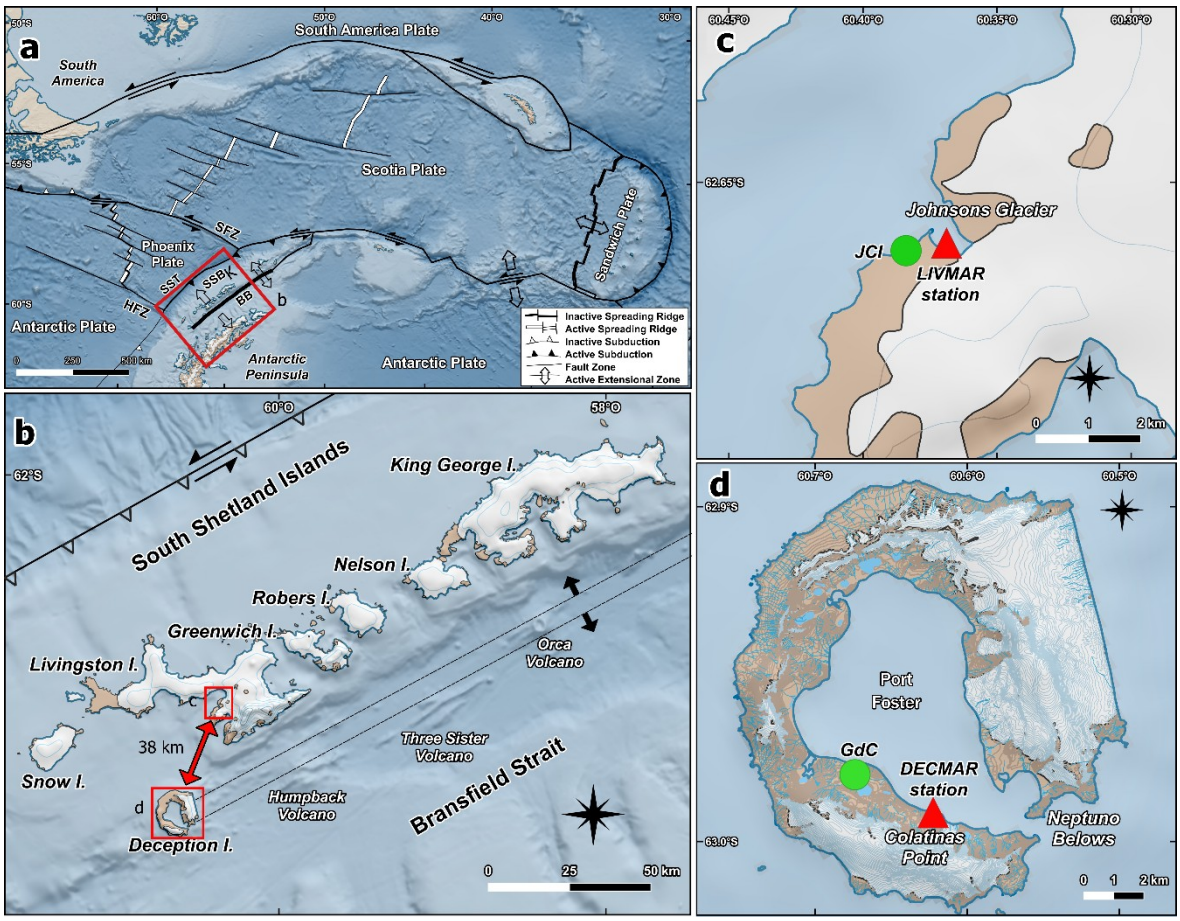


Figure 3.1 a Antarctic region, simplified bathymetric map and tectonic setting of the region. Morphological features: SSBK (South Shetland Block), SST (South Shetland Trench), BB (Bransfield Basin), HFZ (Hero Fracture Zone), SFZ (Shackleton Fracture Zone). **b** South Shetland Archipelago including: King George, Nelson, Robert, Greenwich, Livingston, Deception, Snow, Low and Smith islands. Submarine volcanoes; Humpback, Three Sisters and Orca. **c** Livingston Island, tide gauge at LIVMAR station at Johnsons Cove (red triangle) and Juan Carlos I Antarctic base with atmospheric station (JCI, green dot). **d** Deception Island, tide gauge at DECMAR station at Colatinas Point (red triangle) and Gabriel de Castilla Antarctic base with atmospheric station (GdC, green dot).

Due to its volcanic environment, Deception Island exhibits surrounding waters with unique physicochemical properties, including variations in temperature, turbidity, and chemical composition (Barnes & Conlan, 2007; Caselli et al., 2007; Elderfield, 1972; Martín, 2021), as well as its geodynamic activity (Jiménez Morales et al., 2017; Rosado et al., 2019). Flexas et al. (2017) describes that a strong seasonal influence governs the hydrodynamic circulation inside Port Foster. During summer, due to the atmospheric warming of the sea surface a thermocline is generated leading to a two-layer laminar structure. In the upper layer, circulation is anticlockwise, while in the deeper layer, it is clockwise (Flexas et al., 2017). As autumn arrives, this configuration transitions into a single homogeneous water column, with temperatures near freezing (around -1.85°C) by the end of winter (Lenn et al., 2003). According to Vidal et al. (2012) salinity values in Port Foster were around 33.6-33.7 psu.

The Bransfield Strait is a semi-enclosed region located in the Atlantic sector of the Southern Ocean, at the boundary of the Weddell Sea and Drake Passage, separating the South Shetland Islands from the Antarctic Peninsula (Huneke et al., 2016). At the shelf slope, hydrographic data-based estimates of relative geostrophic circulation indicated the presence of the Bransfield Current (BC), a strong baroclinic current flowing northeastward along the South Shetland Islands (SSI) slope (Sangrà et al., 2017; Veny et al., 2022). Sangrà et al. (2011, 2017) propose that the BC surrounds the northeastern tip of the SSI and recirculates southwestwards along the northern flank of the SSI, within the Drake Passage, this model is based on in-situ hydrographic observations and laboratory experiments, suggesting that the BC behaves as a buoyant gravity current. In addition, Veny et al. (2022) state that the BC is a circulation pattern present throughout the year in the Bransfield Strait.

Water masses in the strait are primarily influenced by freshwater runoff from the surrounding islands (Polukhin et al., 2021) as well as by the interaction of two distinct water masses on the surface: water from the Bellingshausen Sea (Transitional Bellingshausen Water, TBW), which flows into the strait from the west and is pushed against the SSI, and modified water from the Weddell Sea (Transitional Weddell Water, TWW), which enters from the east and moves along the Antarctic Peninsula forming the Antarctic Coastal Current (CC) (García et al., 1994; Pérez et al., 2019; Sangrà et al., 2011, 2017; Seliverstova et al., 2023; Tokarczyk, 1987; Veny et al., 2022). The less dense and warmer water (TBW) flows over the denser and colder water (TWW) driven by the buoyancy-induced pressure gradient and constrained by the Coriolis force (Sangrà et al., 2011; Sangrà et al., 2017; Veny et al., 2022). The Peninsular Front (PF) forms when TBW and TWW encounter, also there is an anticyclonic eddy system (AE) between the BC and the PF, and a modified warmer Circumpolar Deep Water (CDW) tongue beneath the Bransfield Front (Sangrà et al., 2011; Sangrà et al., 2017).

Coastal surface waters in Antarctic regions, which interact with the atmosphere and are altered by meteoric water (mostly from glacial melt), are generally much colder than the upper circumpolar deep water (Barnes et al., 2006; Klinck, 1998). This source of meteoric water provides up to 5% of the near surface ocean during the austral summer. Seasonality is meaningful, with freezing-point temperatures during the winter beginning to rise as solar forcing increases, reaching the warmest waters during the summer and lower salinities (Clarke et al., 2008; Lenn et al., 2003; Meredith et al., 2008). Longer records of near shore temperatures in these regions show a marked seasonal cycle with a pattern where there is a marked variation in temperature between summer maxima and winter minima (Barnes et al., 2006). Mahoney et al. (2011) demonstrated that seawater freezing points in McMurdo vary

between -1.8 °C and -1.9 °C depending on salinity (33.7–34.8 psu). Hunt et al. (2003) obtained seawater temperature records for 2020 at Cape Armitage site and for two consecutive years at McMurdo station; both sites belong to McMurdo Sound. Maximum temperatures reached values of -0.3 °C (Cape Armitage) and -0.4 °C (McMurdo station); and the lowest temperatures at around -1.8 °C. Cárdenas et al. (2018) recorded a water temperature ranging between -1.7 °C and 3.0 °C from January 2016 to February 2017 around Doumer Island (Western Antarctic Peninsula).

Previous studies in the Bransfield Strait showed that the tidal regime is mixed with semidiurnal predominance (Oreiro et al., 2014). The M_2 constituent is the most important with an amplitude around 0.40 m, whereas the O_1, K_1 and S_2 constituents are around 0.28 m (López et al., 1994, 1999). Regarding the study area, Dragani et al. (2004) described the amplitude and phases of the main constituents in two locations of Deception Island, obtaining an amplitude and phase of the M_2 of 0.40 m and 280º, respectively, and an amplitude of 0.20 m for the S_2.

3.2 Expanded study area

Continuing with the study area of the thesis, but focusing on a phenomenon affecting a larger scale, the study area is extended to include regions of the Pacific (see **Figure 3.2a**). This expansion is motivated by the recent activity of the HTHH volcano, located in the southwest Pacific (20°32'9.60"S 175°22'55.20"W), along the Kermadec intra-oceanic arc formed by the subduction of the Pacific Plate beneath the Indo-Australian Plate (Schellart et al., 2006). The volcanic cone emerged following the 2014/2015 eruption when the islands of Hunga Tonga and Hunga Ha'apai merged due to pyroclastic material deposition (Brenna et al., 2022).

The latest eruptive phase began in December 2021 and culminated on 15 January 2022 at 04:10 UTC with a powerful eruption producing a massive plume, atmospheric waves, and ocean waves that traversed the Pacific Ocean, separating the islands once again (Brenna et al., 2022; Kubo et al., 2022; Omira et al., 2022; Ramírez-Herrera et al., 2022; USGS, 2022). According to Kataoka et al. (2022), Omira et al. (2022), and Heidarzadeh et al. (2022), the meteotsunamis generated by the HTHH eruption propagated concentrically from the northwest (red star in **Figure 3.2a**) towards the study area (**Figure 3.2b** and **Figure 3.2c**).

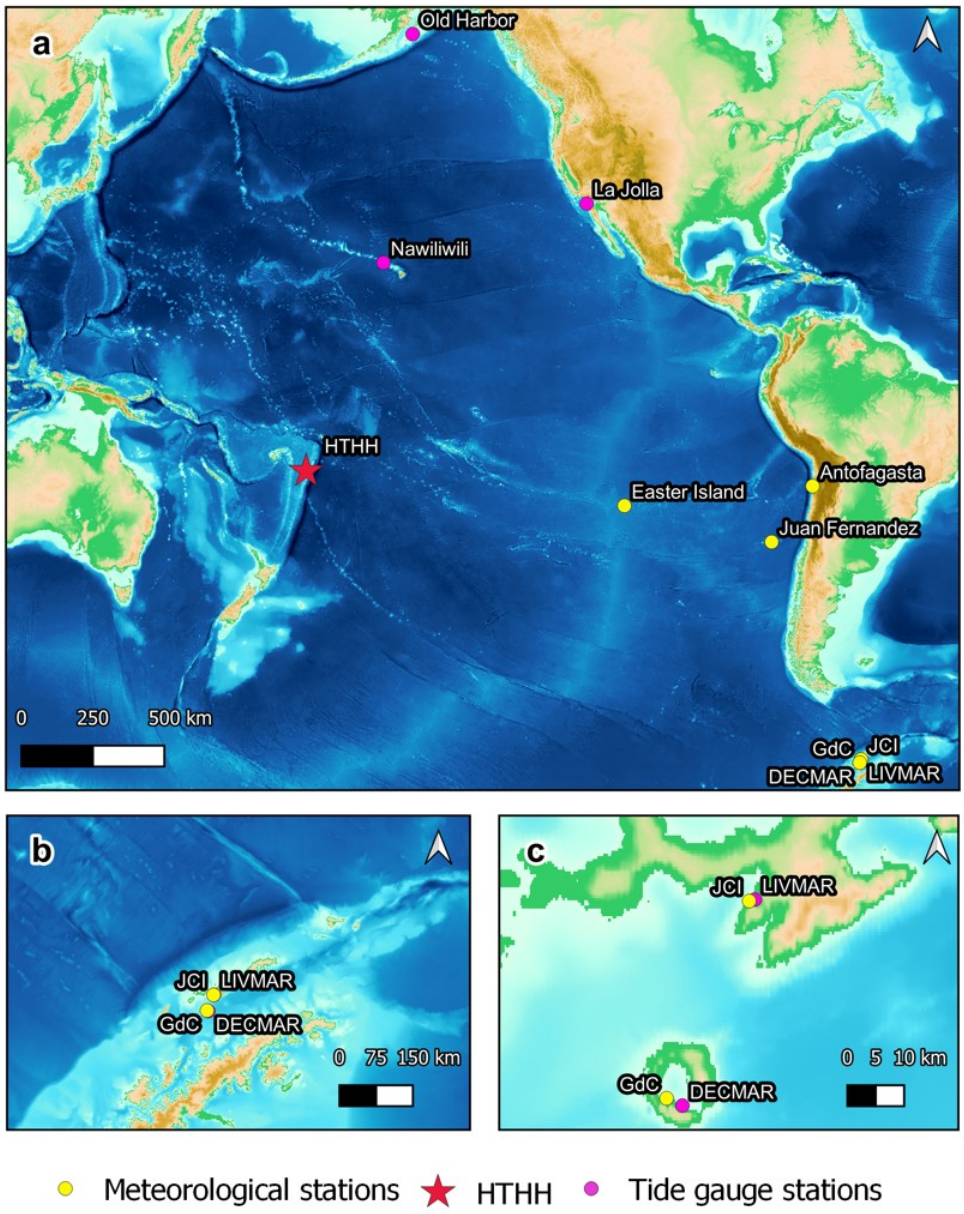


Figure 3.2 a Global map of the stations used in this study. Red star denotes the HTHH volcano, while in-situ instruments, including tide gauges and weather stations, are indicated by pink and yellow dots, respectively. **b** Zoom-in of the bathymetry of the study area showing the subduction zone near the South Shetland Islands. **c** Location of tide gauges and meteorological stations in Deception and Livingston islands. The bathymetry is represented in shades of blue, with the lightest tones indicating the shallowest areas and the darkest tones indicating the deepest. Bathymetry derived from the GEBCO 2023 Grid and visualised with QGIS.

CHAPTER 4

Data and Methodology

4.1 Data

4.1.1 Oceanographic stations

4.1.1.1 Antarctic tide gauge stations

During the 2007–2008 survey, the Astronomy, Geodesy and Cartography Laboratory of the University of Cádiz (LAGC) began recording tide levels at Deception Island. However, at Livingston Island, data collection did not begin until the 2009–2010 survey. Establishing a definitive system for recording the time series on both islands required several years of testing. At first rigid cables were used for tying the instruments, but harsh weather conditions during the austral winter, along with the formation of sea ice, often caused the cables to break, hindered data acquisition. Lei et al. (2018) show similar problems with the sensor anchoring cable and massive sea ice. Furthermore, during certain campaigns, jumps appear in the records. Likewise, Pytharouli et al. (2018), observed jumps in their records and mention that they could be due to datum shifts or instrument failures. Finally, after several attempts, flexible mooring ropes were used, allowing for relatively continuous long-term records on both islands since 2015.

In this study, sea level and temperature records from two stations located on Livingston Island (LIVMAR in **Figure 3.1c**, 62°39'38.70"S 60°22'11.62"W) and Deception Island (DECMAR in **Figure 3.1d**, 62°59'19.02"S 60°37'18.45"W) were used; see Universidad de Cádiz & Berrocoso Domínguez, 2024. The location of LIVMAR station is at Johnsons Cove, at the base of the tide glacier Johnsons, and DECMAR station is at Colatinas Point near Neptune Bellows. The stations are equipped with two AQUAlogger 520PT instruments, which measure both pressure and seawater temperatures with an accuracy of ± 0.2% bar ± 0.05 °C, and resolutions of 0.01% bar 0.007 °C, respectively. As the AQUAlogger instruments are pressure sensors located on the seabed, sea level records derived from pressure are referred to throughout this thesis as ‘tide gauge records’ for simplicity. The instruments were programmed to record data every 20 minutes. This is the minimum possible sampling interval to use the battery for a whole year, as battery replacement work on the sensors can only be carried out during the austral summer. Due to the unavailability of remote connection, each station has two instruments which record simultaneously in case one of them fails during the year. Moreover, as there is no harbour at Livingston and Deception Islands, the instruments are located on the seabed (see **Figure 4.1**), which makes it difficult to process the series due to each year the sensors are at different depths and reference them to the ellipsoid becomes complicated (see Appendix I).

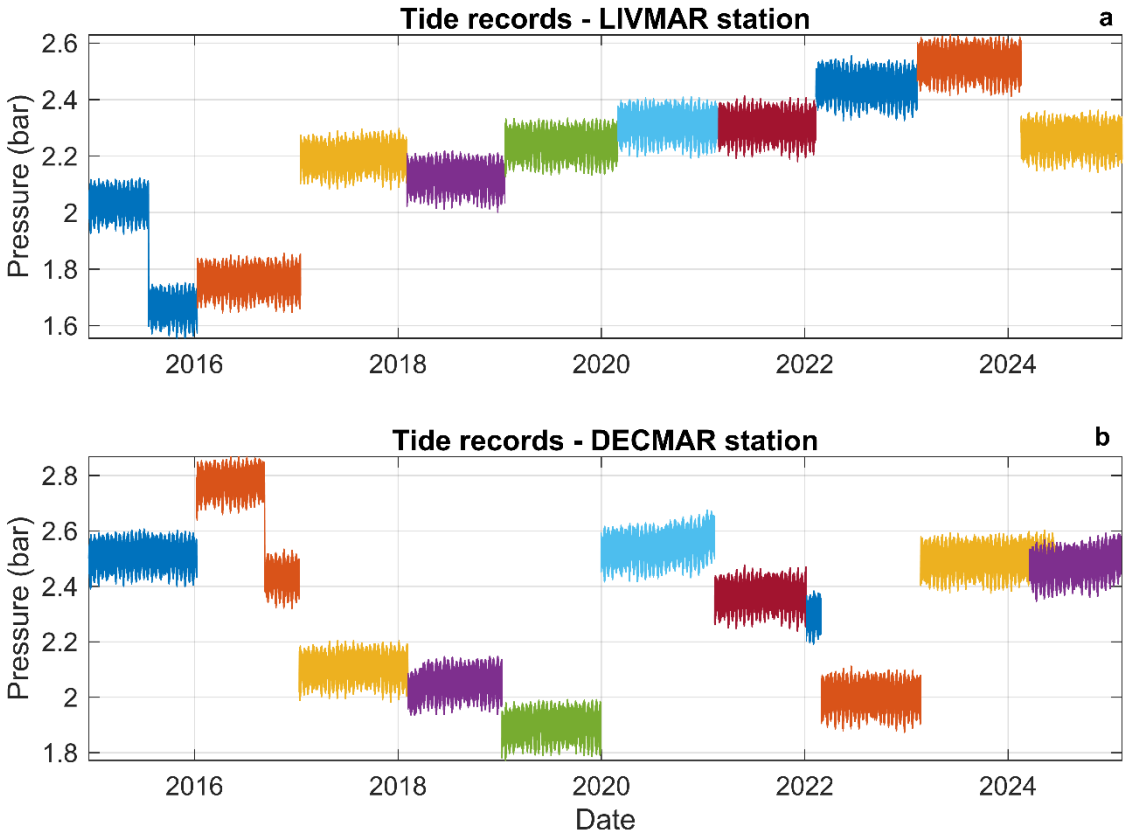


Figure 4.1 a Pressure tide gauge records of LIVMAR station. **b** Pressure tide gauge records of DECMAR station. Each record spans approximately one year and is identified by a different colour.

4.1.1.2 Pacific tide gauge stations

Tide gauge data from three stations operated by the National Oceanic and Atmospheric Administration (NOAA) in the Pacific Ocean were utilised for comparison. These data were sampled at 1-minute intervals. The stations included Nawiliwili, Kauai (21°57'18"N 159°21'24"W), which operated a pressure sensor; Old Harbor, Alaska (57°12'12"N 153°18'12"W), which was equipped with a radar sensor; and La Jolla, California (32°52'0"N 117°15'24"W), which used an acoustic tide gauge.

4.1.2 Meteorological stations

4.1.2.1 In-situ atmospheric temperature

The in-situ atmospheric temperature data come from the Spanish Meteorological Agency (AEMET), which operates two meteorological stations located next to LIVMAR station (JCI in **Figure 3.1c**, 62°39'47"S 60°23'16"W) and next to DECMAR station (GdC in **Figure 3.1d**, 62°58'37.16"S 60°40'3.63"W). AEMET started meteorological data acquisition in 1988

supporting the Spanish bases with weather forecastings. The stations are equipped with HMP155 Vaisala sensors that measure air temperature at 10-minute intervals, with an accuracy of ± 0.35°C. The sensors are positioned 12 metres above sea level (a.s.l.).

The air temperature series has been downloaded from AEMET OpenData from 2015 to 2024. Since raw data are often missing or of poor quality due to technical issues or adverse weather conditions (e.g., snow, ice, wind), the dataset is filtered to minimize errors (Recondo et al., 2022). In addition, in order to have the data at the same interval as the water temperature data, they were averaged every 20 min.

4.1.2.2 In-situ atmospheric pressure

Antarctic stations

The in-situ atmospheric pressure data in the Livingston and Deception islands are from the stations JCI and GdC operates by AEMET (**Figure 3.1d)**. The stations have a PTB101B sensors measuring the atmospheric pressure at a time sampling of 10 min, with an accuracy of ± 0.5 mbar. The series have been downloaded from AEMET OpenData from 2015 to 2024.

Chilean station

Auxiliary atmospheric pressure time series from three meteorological stations of the Chilean Meteorological Directorate were also used. They are located on Easter Island (27º8'60"S 109º25'48"W; 44 m a.s.l.), Juan Fernandez Island (33º39'36"S 78º55'48"W; 40 m a.s.l.) and Antofagasta (23º26'60" S 70º26'24"W; 31 m a.s.l.) (**Figure 3.2a**). The sensors are Vaisala, PTB 330 for Easter Island and PTB 110 for Juan Fernandez Island and Antofagasta. The stations have a sampling interval of 1 minute, so the time series were subsampled to a 10-minute interval in order to match the time sampling of the AEMET meteorological station. The instruments have an accuracy of 0.025% full scale and 0.01 HPa resolution.

4.1.3 Reanalysis atmospheric pressure of ERA 5

As complete series of in-situ atmospheric pressure were not available at LIVMAR, this thesis also employed reanalysis data from ERA5, the fifth generation of European Centre for Medium-Range Weather Forecasts (ECMWF) reanalysis for global climate and weather (Hersbach et al., 2020). These data enabled the characterisation of atmospheric forcing associated with sea level anomalies and provided continuous pressure fields over the study

area. The data were extracted over a geographical grid comprising both satellite crossover points and LIVMAR station, with a horizontal resolution of 0.25° × 0.25° and an hourly temporal resolution. To obtain the atmospheric pressure values at the exact location of the LIVMAR station, a bilinear spatial interpolation was applied to the surrounding grid points. Subsequently, as sea level data were required at a higher temporal resolution (every 20 minutes, consistent with the tide gauge data), a linear temporal interpolation was performed to resample the time series and fill intermediate values. This approach ensures spatial and temporal continuity while preserving the large-scale variability of the ERA5 fields.

4.1.4 Dynamic Atmospheric Correction (DAC)

Among the different corrections applied to the altimetry data, the Dynamic Atmospheric Correction (DAC) was specifically used to remove the atmospheric and barotropic contributions and thus isolate the sea level anomaly signal. The DAC correction includes both the high-frequency barotropic response of the ocean to atmospheric forcing, such as wind and pressure variations, and the static effects represented by the inverted barometer approximation (Carrère & Lyard, 2003; LEGOS/CNRS/CLS, 1992; Valle-Rodríguez et al., 2023). This correction is generated by Collecte Localisation Satellites (CLS), a French oceanographic service provider, using the Mog2D barotropic ocean model developed by the Laboratoire d'Études en Géophysique et Océanographie Spatiales (LEGOS). The corrected data are distributed via the AVISO+ platform, with support from the Centre National d'Études Spatiales (CNES), the French space agency (https://www.aviso.altimetry.fr/).

The DAC data were retrieved for an area covering the LIVMAR station, with a horizontal grid resolution of 0.25° × 0.25° and a temporal frequency of 6 hours. A bilinear interpolation was applied to obtain DAC values at the station coordinates, and a subsequent linear interpolation in time was used to match the 20-minute sampling interval of the tide gauge data. This ensures full spatiotemporal consistency between the DAC product and the in-situ sea-level observations while retaining the large-scale variability represented by the model.

4.1.5 Satellite altimetry from Sentinel 3A/3B

The European Union (EU) space programme includes the Earth observation component Copernicus, which provides information services based on satellite and in-situ data. Sentinel-3 is part of the EU Copernicus mission and is a constellation of two identical satellites: Sentinel-3A (S3A) launched on February 16, 2016, and Sentinel-3B (S3B) launched on April 25, 2018. Each satellite has a repeat cycle of 27 days with a subcycle of ~ 4 days (Donlon et al., 2012). One of the main objectives of the Sentinel-3 mission is to

measure sea surface topography; the Synthetic Aperture Radar Altimeter (SRAL) on board measures distance between the satellite and Earth's surface with a high precision and accuracy. Detailed information on these data can be found in the Sentinel-3 altimetry document library, accessible at https://sentiwiki.copernicus.eu/web/s3-mission. This study is based on data from the SRAL instrument on board S3A/S3B, which operates 100% in Synthetic Aperture Radar (SAR) mode.

For the selection of the altimetric data, the crossover points of S3A and S3B closest to LIVMAR were identified. **Figure 4.2** shows the satellite ground tracks of the study's crossover points, selected based on their proximity to the LIVMAR station, 38 km for S3A and 15 km for S3B. The crossover for S3A (approx. 62º44'15.8"S 61º04'47.93"W) consists of the ascending track #0317 and descending track #0052, covering the period from January 2018 to December 2024, which corresponds to the full years available in the data repository. For S3B (approx. 62º44'42.62"S 60º36'42.62"W), the crossover is formed by ascending track #0374 and descending track #0109, spanning from January 2019 to December 2024. Both satellites have a repeat orbit of 27 days, with Sentinel-3B's orbit being identical to Sentinel-3A's but offset by +/-140°.

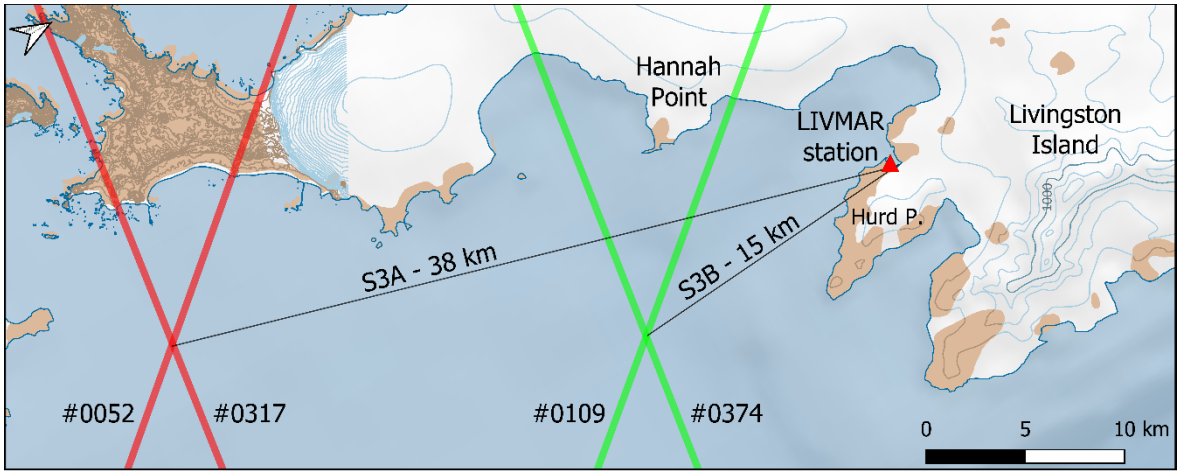


Figure 4.2 Study area. The green lines represent the ascending and descending orbits of S3B (#0374 and #0109 respectively) and the red lines represent the ascending and descending orbits of S3A (#0317 and #0052 respectively). The location of the tide gauge station (LIVMAR) is marked with a red triangle. The map was produced using the Quantarctica package for the Quantum Geographic Information System (QGIS), developed by the Norwegian Polar Institute.

Altimetry data from S3A/3B Level-2, generated by the European Organisation for the Exploitation of Meteorological Satellites (EUMETSAT) Marine Centre, were accessed through Copernicus Browser (https://browser.dataspace.copernicus.eu; EUMETSAT For

Copernicus & European Organisation For The Exploitation Of Meteorological Satellites, 2023). The Level-2 product (baseline collection 005) provides geophysical parameters derived from the SRAL measurements, including variables related to sea level variability, corrected for atmospheric and geophysical effects. The dataset consists of sea level observations acquired at a posting rate of 20 Hz, corresponding to a nominal along-track spacing of approximately 330 m between consecutive radar observations.

To complement the Level-2 observations, Level-1B SRAL data from S3A and S3B (baseline collection 004) were also retrieved (EUMETSAT For Copernicus & European Organisation For The Exploitation Of Meteorological Satellites, 2022). These data provide the full radar return waveform, whose shape of this waveform is highly dependent on the nature of the reflecting surface, and is useful for detecting differences between features on sea ice and those in open water (Armitage & Davidson, 2014; Fredensborg Hansen et al., 2021; Mugunthan et al., 2023; Tang et al., 2023). These return waveforms were inspected for observations coinciding with anomalous SLA values to assess the quality of the altimetric signal and to identify patterns characteristic of sea-ice covered surfaces, thereby complementing the analysis of the Level-2 observations.

4.1.6 Sentinel-1 SAR images

SAR imagery has become a primary tool for monitoring sea ice in polar regions due to its capacity to acquire data independently of sunlight and weather conditions (Lohse et al., 2021; Zakhvatkina et al., 2019). The Sentinel-1 mission, part of the EU Copernicus Programme, provides open-access SAR images, offering a valuable resource for Earth observation and sea-ice analysis (Zhao et al., 2020). Acquired by active microwave sensors, SAR imagery is particularly effective in polar environments where optical sensors are often limited by persistent cloud cover and extended periods of darkness (Gao et al., 2019; Khaleghian et al., 2021).

SAR images represent the intensity of radar backscatter from the Earth's surface, quantified by the backscattering coefficient. This information forms a reflectivity map of the imaged area: surfaces or objects which return stronger radar signals appear as bright areas, while smoother or flatter surfaces, which return less signal, are depicted as darker regions. This characteristic makes SAR particularly suitable for distinguishing between open water and various types of sea ice.

In this study, SAR imagery was used for the visual identification of sea ice extent in the area of interest. Data from the Copernicus Sentinel-1 archive were accessed via the Copernicus Browser (https://browser.dataspace.copernicus.eu). In order to identify seawater, an image acquired during the austral summer was taken as a reference, so that the presence of sea ice could be distinguished in the winter images. The specific images used were in Extra Wide (EW) swath mode and were displayed in greyscale using the gamma0 of the horizontal (HH) polarisation. The HH channel provided strong contrast between land and water surfaces and was particularly suitable for detecting hard targets and differentiating surface types. The images were calibrated to gamma0 and visualised in decibel scale, applying logarithmic scaling to enhance dynamic range and contrast.

4.2 Methodology for the establishment of the in-situ series

This section presents the methodologies followed to establish the sea level time series at both stations, which are subsequently used throughout the different chapters. The specific methodologies applied in each case are described in the corresponding chapters.

The bottom pressure records (previous **Figure 4.1**) are converted to sea level height following the hydrostatic Eqs. (4.1) - (4.2):

$$P = P_a + \rho g h \tag{4.1}$$

$$h = \frac{P - P_a}{\rho g} \tag{4.2}$$

where P is the bottom pressure, P_a is the annual mean atmospheric pressure, ρ the water density (1025 kg/m^3), g is the acceleration of gravity (9.82 m/s^2) and h is the sea level height.

The 10-minutes atmospheric pressure series (P_{atm}) used in Chapter 7 were corrected to sea level zero following the World Meteorological Organisation (WMO, 2023) formula designed for stations below 50 m altitude with which the correction parameter (C) is calculated (Eq. 4.3):

$$C = \frac{(P_{atm} + Hp)}{(29.27\, Tv)} \tag{4.3}$$

where P_{atm} is the observed pressure in hectopascals; Hp is the station elevation in metres (12 m); and Tv is the annual mean temperature in degrees Kelvin.

4.2.1 Harmonic analysis by least squares fitting and tide prediction

Harmonic analysis by least squares fitting to known astronomical frequencies is one of the most widely used methods to characterise the astronomical tide in sea level and current records (Godin, 1972). This approach assumes that the observed series can be expressed as the superposition of a finite number of harmonic constituents, each associated with an astronomical frequency derived from tidal potential theory (Cartwright & Tayler, 1971; Doodson, 1921). For each constituent, the analysis provides its amplitude and phase, which together describe the local tidal response.

In this study, the harmonic analyses were performed with the *t_tide* toolbox (Pawlowicz et al., 2002) and the *u_tide* package (Codiga, 2011). Both routines implement classical least-squares harmonic analysis, including nodal corrections and inference, in order to obtain reliable estimates of amplitudes and phases for each resolvable constituent. The fitted series can be expressed as a sum of sinusoidal components, with coefficients determined by minimising the squared error between observations and the harmonic reconstruction.

A key limitation of this method is imposed by record length. According to Rayleigh's criterion (Godin, 1972), two tidal constituents can only be distinguished if their frequency separation exceeds the inverse of the total record duration. Consequently, many of the constituents included in the harmonic development of the tidal potential are not individually resolvable in practice. A common approach is to group together those with very close frequencies, retaining the dominant component as the primary constituent and accounting for the others as satellites. In such cases, the amplitudes and phases initially obtained are apparent values, influenced by the unresolved satellites, and must be corrected through nodal modulation or inferred from reference stations where both components can be separated (Foreman & Henry, 1989).

Once the harmonic constants (amplitudes and phases) were obtained, they served as the basis for predicting the tide outside the observation window. The predictions were generated using two complementary tools: the *u_tide* package, which directly incorporates its own prediction module, and the *Tidex* programme (developed at the University of Cádiz), which produces tidal predictions when supplied with previously calculated harmonic constituents.

4.2.2 Correction of displacements in the records

As mentioned in Section 4.1.1.1, some records show vertical displacements, which could be caused by sea ice formation during the winter. Further evidence of this can be observed in **Figure 4.3**, where the data from the two moored sensors deployed at LIVMAR in 2015 reveal noticeable discontinuities in the tide measurements.

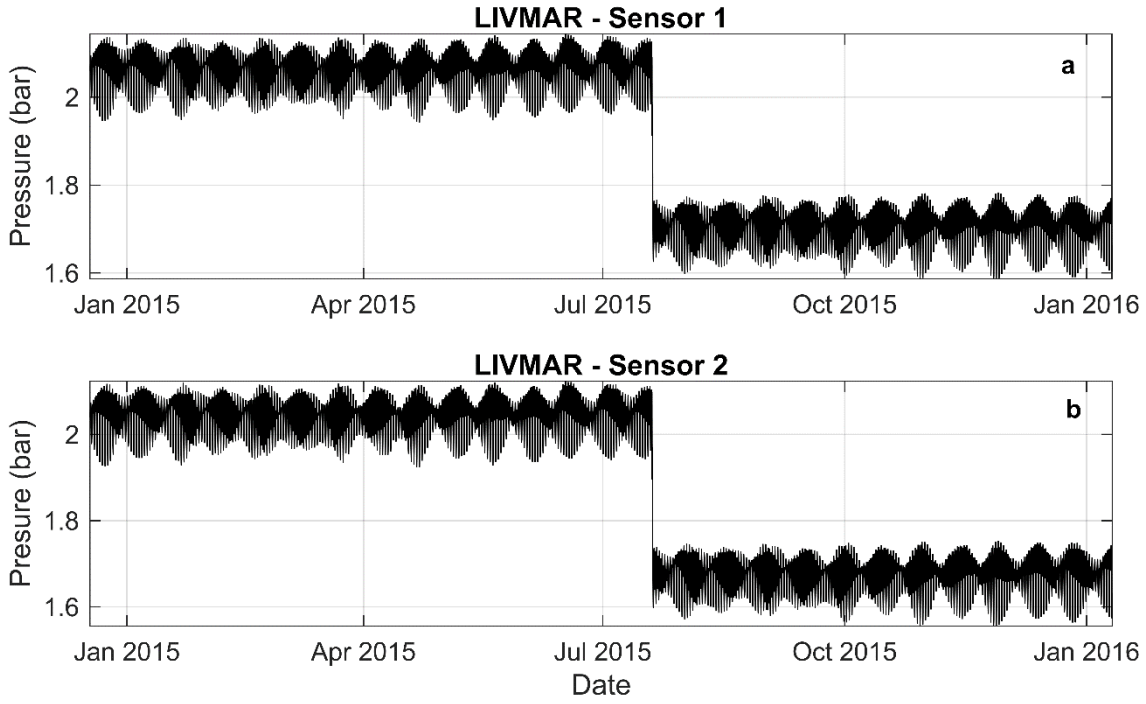


Figure 4.3 a Pressure record from Sensor 1 at Livingston Island in 2015. **b** Pressure record from Sensor 2 for the same period. Both series show an identical displacement occurring at the same time, thereby ruling out sensor malfunction as the cause for this campaign.

The applied method comprises several steps to correct the record's jumps. The first step was the performing a harmonic analysis over the period prior to the jump, which usually was 6 or 8 months long, depending on the campaign, using the Matlab's t_tide tool of Pawlowicz et al. (2002). Once the harmonic constants are obtained, tide predictions were made with the Tidex program for a period that covered the jump events. This program allows to calculate tidal predictions using as input the given harmonic constants list.

As the mean sea level used to make the prediction sometimes does not adjust well to the mean level of the period covered by the jump, two predictions were made; one using the mean sea level yielded by the harmonic analysis of the records spanning the period previous to the jump and another using the mean sea level covering a much less period of approximately 2 days, trying to better approach the actual mean sea level existing during the

jump event. The latter averaging period is slightly enlarged, when necessary, in order to have the same number of low as high tides and not produce biases in the computed mean sea level previous to the jump. The prediction that best matched the observation on the two days prior to the jump is finally selected.

An example of the method performance is illustrated in **Figure 4.4** which shows the two predictions superimposed on the observed record in order to identify the best fit to the record before the jump. In this case, it can be seen that the prediction fitting best is the one using the mean level yielded by the harmonic analysis of the days before the displacement (discontinued line).

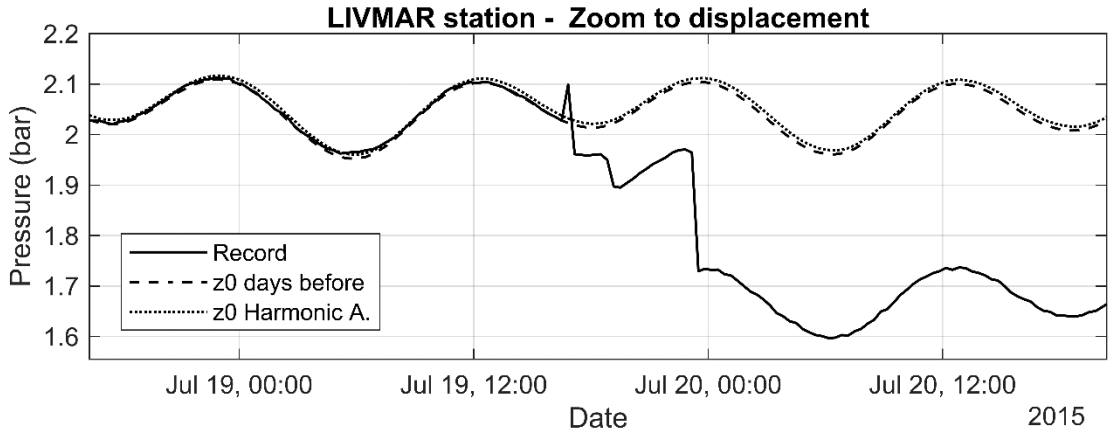


Figure 4.4 Predictions and record superimposed. The dotted line corresponds to the average of the average level of the harmonic analysis (z0 AA) and the discontinued line to the average level of the days before the displacement (z0 days before).

Once the most suitable prediction is chosen, the vertical displacement of the mean sea level is estimated by the difference between the recorded and predicted values after the jump. Later, this value is added to the subsequent data and a corrected record is obtained with the exception of the values recorded while the sensor kept moving until it reached a new resting position (**Figure 4.5**).

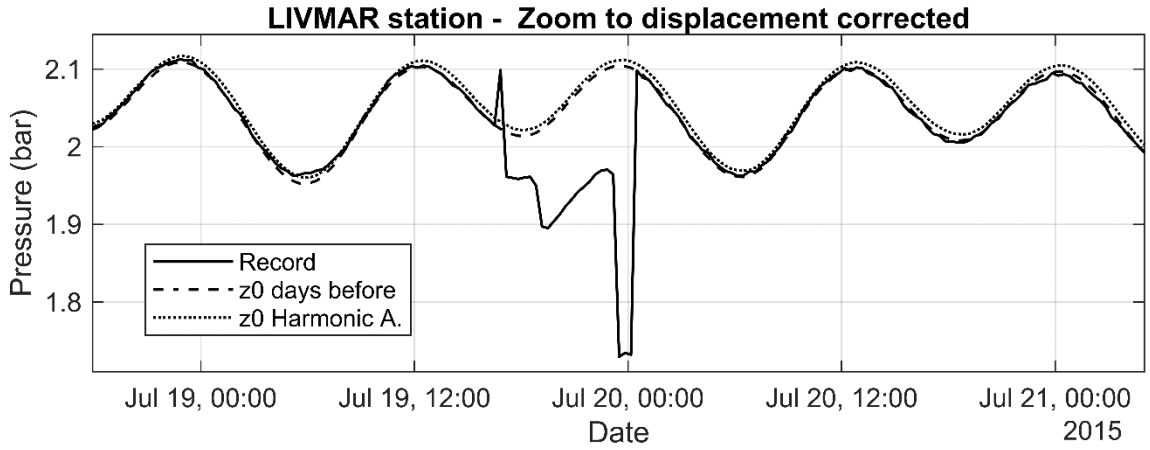


Figure 4.5 Predictions and record superimposed of Livingston Island after applying the necessary correction in the presence of displacements. The dotted line corresponds to the average of the average level of the harmonic analysis (z0 AA) and the discontinued line to the average level of the days before the displacement (z0 days before).

Finally, these latter values were replaced by those corresponding to the prediction at the same instants, and continuous corrected records were obtained for the whole recorded period (**Figure 4.6**).

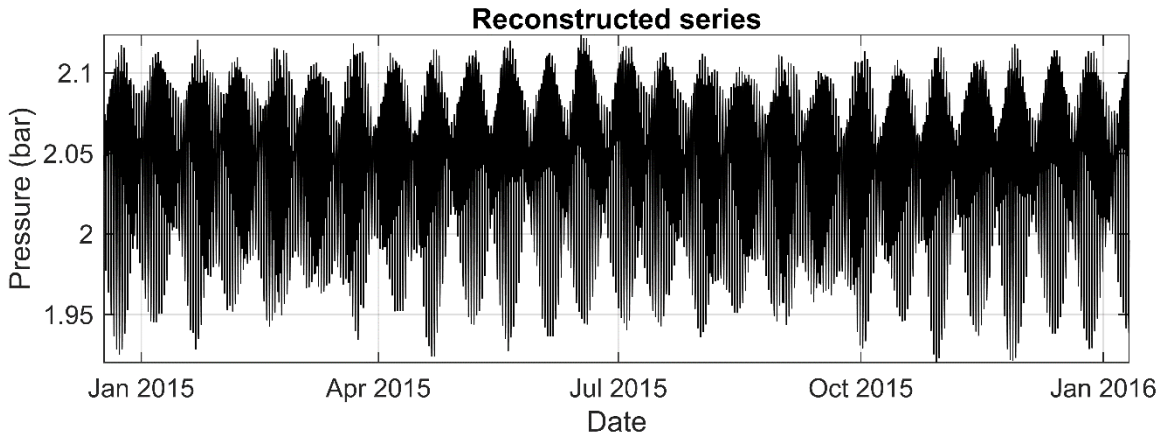


Figure 4.6 Complete record for Livingston Island after the correction of the displacement present in the 2015 record.

The new tidal constants provide tidal predictions that better match the observed records (**Figure 4.7**). In addition to scientific purposes, these constants will be used to calculate the tidal predictions used at the Spanish Antarctic bases in Antarctica to carry out work on the islands.

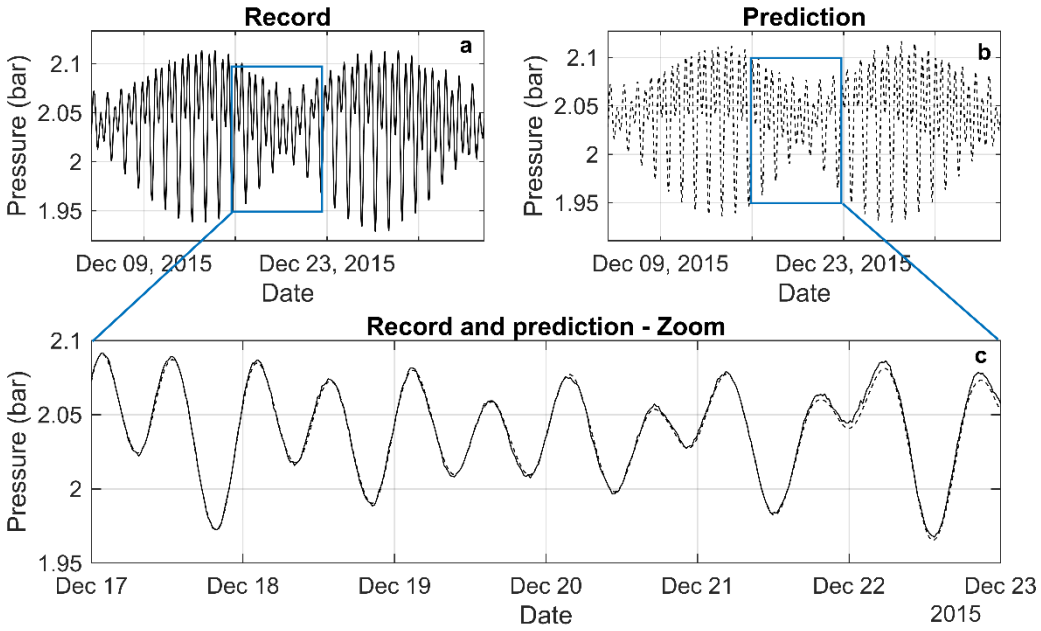


Figure 4.7 a Pressure record from the LIVMAR oceanographic station. **b** Tide prediction for the same period, based on harmonic constituents calculated from the observed series. **c** Superposition of the in-situ measurements and the predicted series.

The resulting datasets provide a consistent basis for examining sea level variability in the region. **Figure 4.8** presents the final, corrected sea level time series for both stations. Although reconstructed sea level time series are available for both stations, the DECMAR record exhibits pronounced long-term trends during specific periods (2018, 2020 and 2024). As the origin of these trends cannot be resolved within the methodological framework of this study, only the LIVMAR record is used for the computation of SLA in Chapter 5.

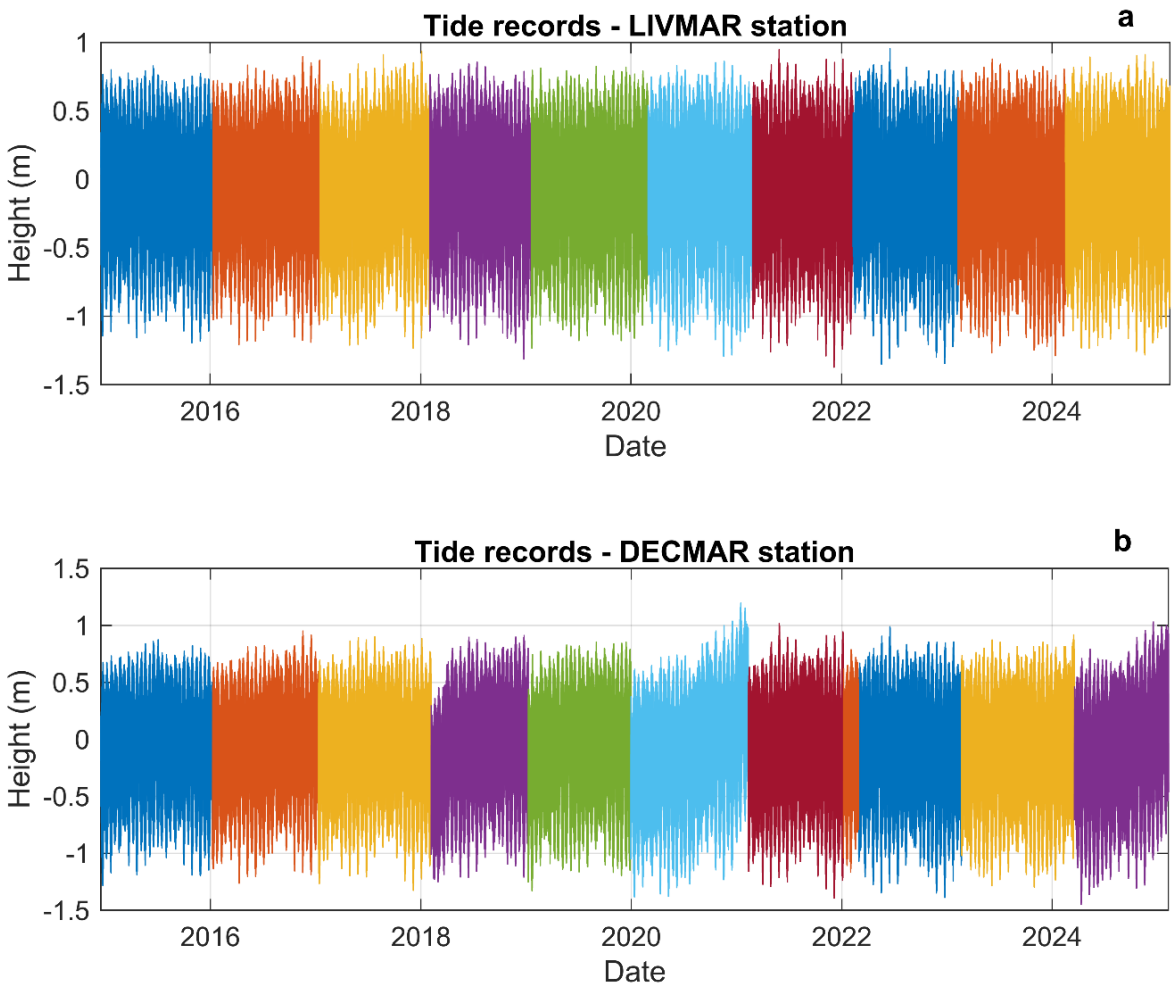


Figure 4.8 a Reconstructed sea level time series for the LIVMAR station (2015–2024), compiled from annual datasets. **b** Equivalent reconstruction for the DECMAR station. Each record spans approximately one year and is identified by a different colour.

4.2.3 Data validation through harmonic analysis

To assess the quality and consistency of the reconstructed sea level series, a harmonic analysis was performed as part of the data pre-processing. The *t_tide* package (Pawlowicz et al., 2002), as described in Section 4.2.1, was applied to the corrected records for the period 2015–2024.

Table 4.1 summarises the amplitude and phase of the main diurnal (K_1, O_1) and semi-diurnal (M_2, S_2) constituents for both stations. The results are consistent with reported in existing tide tables for the region (Dragani et al., 2004; Oreiro et al., 2014; Vidal et al., 2012). The low interannual variability observed between 2015 and 2024 further confirms both the reliability of the harmonic analysis and the robustness of the records.

Table 4.1 Amplitude and phase of harmonic components M_2, S_2, K_1, and O_1 for Livingston and Deception Islands (LIVMAR and DECMAR stations) in the period 2015/2024.

LIVMAR station	**AMPLITUDE (m)**				**PHASE (°)**			
	O_1	**K_1**	**M_2**	**S_2**	**O_1**	**K_1**	**M_2**	**S_2**
2015	0.27	0.27	0.40	0.20	48.69	67.45	277.24	338.35
2016	0.27	0.27	0.40	0.21	49.03	68.42	278.38	339.27
2017	0.26	0.26	0.40	0.21	48.26	67.50	276.98	338.23
2018	0.26	0.26	0.40	0.21	48.97	66.92	278.31	338.72
2019	0.26	0.26	0.40	0.21	49.29	69.46	278.92	341.43
2020	0.26	0.27	0.39	0.21	49.05	66.92	277.98	339.56
2021	0.26	0.26	0.39	0.20	49.30	67.04	278.47	338.40
2022	0.26	0.26	0.39	0.21	49.04	67.11	277.78	338.02
2023	0.27	0.27	0.40	0.21	48.44	67.36	278.32	339.80
2024	0.26	0.26	0.39	0.21	48.53	66.31	277.50	338.47
DECMAR station	**AMPLITUDE (m)**				**PHASE (°)**			
	O_1	**K_1**	**M_2**	**S_2**	**O_1**	**K_1**	**M_2**	**S_2**
2015	0.27	0.28	0.40	0.21	52.12	69.41	280.80	342.17
2016	0.27	0.27	0.40	0.21	51.01	68.64	279.38	340.39
2017	0.27	0.28	0.40	0.22	52.17	70.72	281.13	342.71
2018	0.27	0.27	0.40	0.22	51.98	67.28	279.94	339.91
2019	0.27	0.27	0.40	0.22	52.08	69.09	280.98	342.37
2020	0.27	0.28	0.40	0.21	52.55	70.44	280.82	343.55
2021	0.27	0.27	0.40	0.22	51.88	67.06	279.89	339.55
2022	0.27	0.27	0.40	0.21	51.87	67.98	280.05	340.33
2023	0.27	0.27	0.39	0.22	52.58	67.01	281.87	341.55
2024	0.27	0.28	0.40	0.21	51.78	66.98	281.65	340.69

The relative importance of diurnal and semi-diurnal constituents is expressed through the tidal form factor (F), calculated as (see Eq. 4.4; Pugh, 1987):

$$F = \frac{A_{K1} + A_{O1}}{A_{M2} + A_{S2}} \tag{4.4}$$

For both stations, $F \approx 0.88$, classifying the tides as mixed, mainly semi-diurnal (Defant, 1961). This implies two high and two low waters per tidal day, with inequalities in height and timing. These findings are in line with previous research (Dragani et al., 2004; Oreiro et al., 2014; Vidal et al., 2012) and validate the use of the reconstructed series for subsequent analyses.

CHAPTER 5

Assessment of satellite altimetry accuracy (Sentinel-3A/B) with in-situ sea level data at Livingston Island, Antarctica

Sea level records in Antarctica remain limited and challenging to obtain, particularly during winter months due to extreme weather and sea ice formation. This study presents one of the longest in-situ sea level time series available in Antarctica (2015–2024), recorded at Livingston Island, South Shetland Archipelago. The in-situ data were compared with satellite altimetry derived sea level anomalies (SLA) from Sentinel-3A (S3A, 2018–2024) and Sentinel-3B (S3B, 2019–2024). The optimal agreement with tide gauge data was achieved after adjusting the processing parameters, particularly the sea state bias correction and the number of observations averaged around the crossover point. Under these optimized settings, differences between in-situ and satellite measurements were typically within a few centimetres, showing statistically significant correlations. Seasonal analysis revealed that data quality decreases markedly during autumn and winter, when most missing or anomalous measurements coincide with sea- ice presence. In contrast, agreement improves notably during spring and summer. Sentinel-1 SAR imagery and satellite altimetry waveform analysis confirmed sea ice presence in most anomalous cases, with characteristic bimodal shapes and peak shifts observed over ice-covered surfaces. These findings underscore parameter adjustment and seasonal filtering to improve the reliability of satellite altimetry in polar regions, while highlighting the limitations imposed by ice conditions on radar signal retrieval. This study provides the first long-term validation of Sentinel-3A/B altimetry in Antarctica using nearly a decade of in-situ sea level data, extending previous assessments and demonstrating how combined SAR imagery and waveform analysis can effectively detect sea-ice contamination.

Luengo-S, O., De Biasio, F., Bruno, M., Vignudelli, S., Berrocoso, M., & Gómez-Enri, J. (2025). Assessment of satellite altimetry accuracy (Sentinel-3A/B) with in-situ sea level data at Livingston Island, Antarctica. Advances in Space Research. https://doi.org/10.1016/j.asr.2025.12.088

5.1 Statement of the chapter

The main objective of this study is to compare time series of SLA using altimeter data from the Copernicus Sentinel-3A and 3B satellites, along with in-situ pressure sensors. The validation was conducted in the coastal region of the subantarctic islands of the South Shetland Archipelago. The objective of this comparison is to assess the accuracy and reliability of satellite altimetry in monitoring sea level variations in polar regions. Furthermore, it is proposed that altimeter measurements over sea ice can result in SLA values being considered outliers. This proposal is based on the calculation of SDDs for the full year, as well as for summer and winter periods, together with the analysis of S3A/B radar waveforms. In contrast to previous validation studies, this work provides the first long-term evaluation of Sentinel-3A/B altimetry in Antarctic coastal waters, integrating concurrent in-situ observations, SAR imagery and waveform analysis to quantify the influence of sea ice on measurement accuracy.

5.2 Study area

The study area is as described in Chapter 3, this chapter focuses on Livingston Island and its vicinity (**Figure 4.2**).

5.3 Data

This study makes use of sea level data from the LIVMAR tide gauge, Level-1B and Level-2 altimetric data from the S3A and S3B missions (Section 4.1.5), and SAR imagery from Sentinel-1 (Section 4.1.6). These datasets are described in greater detail in the Data chapter. Regarding the analysis period, data from January 2018 to December 2024 are used to compare observations from S3A and the tide gauge, while the comparison between S3B and the tide gauge spans from January 2019 to December 2024.

5.4 Methodology

The general procedures for data pre-processing of in-situ data and validation are described in Section 4.2. Here, we describe only the specific steps related to the comparison between satellite altimetry and tide gauge data.

5.4.1 Altimeter SLA

Altimetry SLA was calculated using the Eq. (5.1):

$$SLA_{altimeter} = Altitude - Range - Range\ and\ Geophysical\ corrections - MSL \quad (5.1)$$

where *Altitude* is the distance between the satellite's centre of mass and the reference ellipsoid; *Range* is the retracked distance between the instrument and the mean-reflected surface, obtained using the SAMOSA 2.5 retracker (Ray et al., 2015); *Range and Geophysical Corrections* applied to Sentinel-3 data (summarized in **Table 5.1** and **Table 5.2**), with some selected according to the Copernicus SLA formulation and others based on available processing options, as documented in the SentiWiki website. Finally, *MSL* (mean sea level) is calculated as the annual mean level for each year and is removed for the corresponding period to ensure consistency with the tide gauge data.

To obtain geophysical parameters, the retracking process applies a curve-fitting technique that relies on the bounded Levenberg–Marquardt least-squares method (LEVMAR-LSE), using a window size of 128 range bins allowing the theoretical SAMOSA waveform to be optimally matched to the measured radar returns for precise ocean data retrieval (Dinardo et al., 2015; C. Ray et al., 2015).

Table 5.1 Range corrections applied to Sentinel-3 data, with some selected from the formula provided by Copernicus for calculating SLA, and others chosen from the available correction options. Information extracted from the SentiWiki website.

Range corrections	
Ionospheric correction	Calculated using dual-frequency measurements from the Ku and C bands.
Dry tropospheric correction	Computed from meteorological models at the altitude of the measurement.
Wet tropospheric correction	Computed using microwave radiometer data (which reflects atmospheric water vapor) interpolated to the SRAL time, and the Ku-band backscatter.
DAC	Computed using the inverse barometer correction and the high frequency fluctuations of the sea surface topography.

Table 5.2 Geophysical corrections applied to Sentinel-3 data, with some selected from the formula provided by Copernicus for calculating SLA, and others chosen from the available correction options. Information extracted from the SentiWiki website.

Geophysical corrections	
Solid earth tide height	Calculated Earth crust deformations from tidal forces, based on Cartwright and Tayler tables, excluding the permanent tide.
Ocean tide	Tide height using the FES2014b model (Lyard et al., 2021). It includes the corresponding loading tide.
Geocentric pole tide	Sea surface height due to pole tide. A scaling factor of 0.468 was applied following Birkett & Beckley, (2010).
Non-equilibrium long period ocean tide	This parameter is computed as a correction to equilibrium long period ocean tide.
Sea State Bias correction (SSB)	The SSB is computed by varying Significant Wave Height (SWH) percentages.

5.4.2 Tide gauge SLA

The sea level records used in this study are derived from water column pressure measurements, which are converted into heights using the hydrostatic equation (Eq. 4.1) and atmospheric pressure data from ERA5 (see Section 4.1.3).

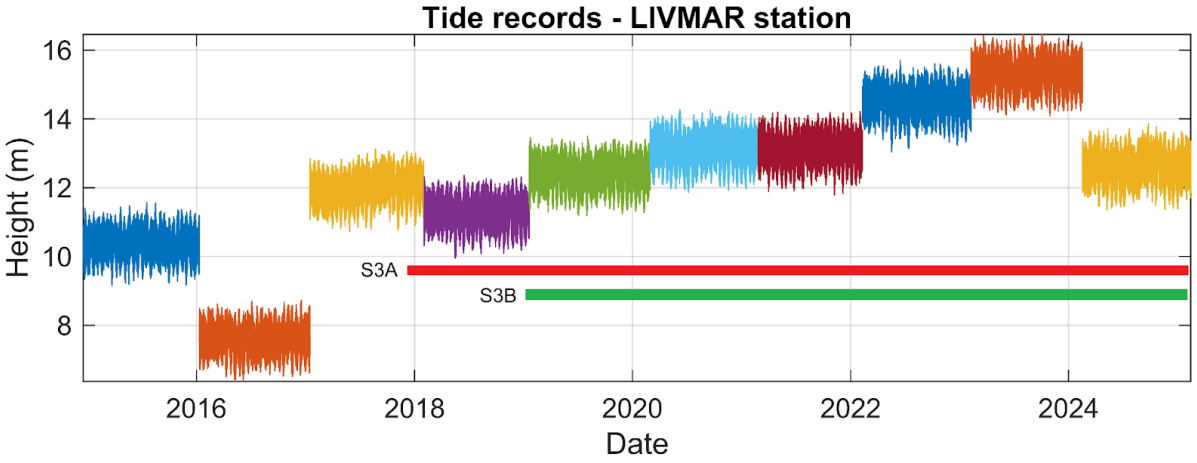


Figure 5.1 Tide records obtained by Eq. (4.2). Each record spans approximately one year and is identified by a different colour. The red line represents the temporal coverage of S3A data and the green line S3B data.

In order to have the same series as the altimeter series, DAC correction was applied. Therefore, SLA from tide gauge is obtained as Eq. (5.2),

$$SLA_{tide\ gauge} = h - Ocean\ tide\ correction - DAC - MSL \quad (5.2)$$

where, h is the height of the sea level obtained by Eq. (4.2), *Ocean tide correction* is done by the prediction calculated with u_tide, *DAC* is the correction due to atmospheric pressure and wind and *MSL* is the temporal mean of tide gauge measurements in each of the years.

The sea level records were processed with the *u_tide* package (Codiga, 2011), which determines and removes the harmonic tidal constituents, the mean sea level (MSL), and the trend. This procedure gives the residual tide. After all corrections have been applied, **Figure 5.2** shows the SLA time series from the tide gauge at the LIVMAR station for the period coincident with the altimetric data. Colours distinguish the individual years within the time series.

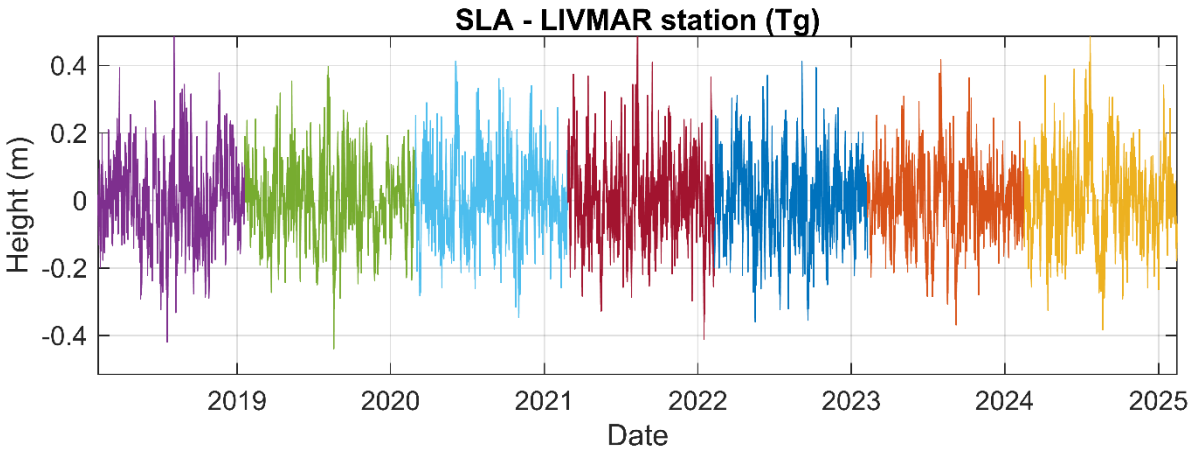


Figure 5.2 In-situ dataset filtered with u_tide by removing the tidal contribution from the most significant harmonic constituents of each record, trend and mean sea level. Zoom-in of the **Figure 5.1**, section of the tide gauge record that corresponds to the period of altimeter data. Each colour represents a different year.

5.4.3 Comparison between series

In order to be able to compare both sea level series, first of all, the altimeter series has to be generated. The procedure used to derive the SLA value for each overpass was explained in Section 5.4.1, and these values were subsequently used to build the time series.

To establish a starting point, the approximate centre point of the crossing of the tracks is identified (**Figure 4.2**). In order to identify the ideal number of data used per overpass and the appropriate %SWH, 176 combinations are composed by varying both parameters.

Before generating the time series, a quality-control step was applied to remove anomalous measurements along each track. A ±3 standard deviations (±3σ criterion) along-track filter was used to detect and discard outliers in the SLA values, ensuring that only consistent data were retained for further analysis.

The number of averaged data to calculate the SLA per overpass could vary by two from 1 to 21, as it is considered from the closest to the crossover point ± M, where M ranges from 0 to 10. It should be noted that the estimation of SLA is affected by the SSB, which in turn depends on the SWH. As in traditional altimetry, measurement noise increases with SWH (Halimi et al., 2014; Ray et al., 2015). Additionally, SSB causes wave height-dependent errors in SLA measurements, affecting their accuracy (Rieu et al., 2021). Since the SSB correction provided by Sentinel-3 is derived from Jason-2, a specific methodology has been applied to determine the most suitable correction, following approaches proposed by other authors (Aldarias et al., 2020; Fenoglio-Marc et al., 2015; Gómez-Enri et al., 2018; Valle-Rodríguez et al., 2023). Therefore, this step involves selecting the percentage of SWH used as SSB, with values from 0 to 15 in increments of 1.

As the tide gauge series has more data than the altimeter series, depending on the number of altimeter data taken (central data ± M) to compose the series, the tide gauge series shall be subsampled. As mentioned in Peng & Deng (2020), a greater temporal difference between altimeter and tide gauge SLAs can increase discrepancies. To minimise this effect, both datasets were matched within a maximum time difference of ±10 minutes, ensuring that each altimetric measurement was paired with the closest tide-gauge observation within this time window.

To determine the percentage of SWH that enables a greater similarity between both SLA time series, it was calculated the standard deviation of the differences was calculated (*SDD,* Equation 5.3), the mean absolute deviation (MAD, Equation 5.4) and the Pearson correlation (*r*, Equation 5.5) between the two-time series.

$$SDD = \sqrt{\frac{1}{n-1}\sum_{i=1}^{n}(d_i - \overline{d})^2} \tag{5. 3}$$

where d_i is the difference of the altimeter and tide gauge series, $\overline{d}$ is the mean of the differences and n is the total of the differences.

The MAD was computed as a complementary metric to quantify the average magnitude of the differences:

$$MAD = \frac{1}{n}\sum_{i=1}^{n}|d_i| \tag{5. 4}$$

The Pearson correlation coefficient between the two series X and Y was computed using the following equation:

$$r_{XY} = \frac{\sum_{i=1}^{n}(x_i - \overline{x})(y_i - \overline{y})}{\sqrt{\sum_{i=1}^{n}(x_i - \overline{x})^2}\sqrt{\sum_{i=1}^{n}(y_i - \overline{y})^2}} \tag{5. 5}$$

where x_i and y_i represent the individual paired observations of the variables X and Y, respectively; $\overline{x}$ and $\overline{y}$ denote their mean values; and n is the total number of paired observations.

Finally, once the series were constructed, a methodology to identify and remove outliers was carried out. A version similar to that used by other authors (Dinardo et al., 2018; Fenoglio et al., 2021; Meloni et al., 2019; Passaro et al., 2021; Peacock & Laxon, 2004) was used. It is based on the ±3 standard deviations (±3σ) criterion and is iteratively applied 10 times. Outliers identified in each series are also replaced as NaN in the corresponding series. To ensure comparability with the tide gauge data, the altimetric series were detrended and the annual mean was removed.

5.5 Results

5.5.1 Determination of the optimal altimetric SLA for comparison

For the time period of study, 188 overpasses would be expected for S3A (January 2018-December 2024) and 163 overpasses for S3B (November 2019-December 2024) at the crossover sites shown in **Figure 4.2**. A total of 177 (94%) overpasses for S3A and 150 (92%) overpasses for S3B were analysed, which is fewer than expected, as some overpasses are not available in the data archive. The reason for the missing cycles is unknown.

Before removing the outliers, the S3A series had 11 missing data points out of 177 overpasses, which increased to 24 after outlier removal, resulting in 86.4% of valid data for the comparison (153 overpasses). For S3B, there were 10 missing data points out of 150 overpasses before outlier removal, which increased to 20 after, leaving 86.6% of valid data for comparison (130 overpasses). Finally, the invalid altimeter data that coincided in time with the tide gauge data were replaced with NaN.

After evaluating all possible combinations of the number of data used (central data ± M) and the percentage of SWH for SSB correction (both derived from the altimetric data), as discussed in the previous section, the statistical comparison between the in-situ and altimetric sea-level series was performed using the SDD (**Figure 5.3**) and the MAD as performance metrics. For S3A, the combination of M = 9 and 5% SWH resulted in the lowest SDD and MAD values; the SDD distribution is shown in dark blue in **Figure 5.3a**. For S3B, the minimum SDD values are likewise shown in dark blue, with the optimal combination being M = 9 and 5% SWH, corresponding to the lowest observed SDD (**Figure 5.3b**). Although slightly lower values were found at higher M, increasing M beyond 15 did not further reduce the discrepancies. It should be noted that Figure 5 displays only the SDD results; however, both SDD and MAD were jointly considered to determine the optimal combination of parameters.

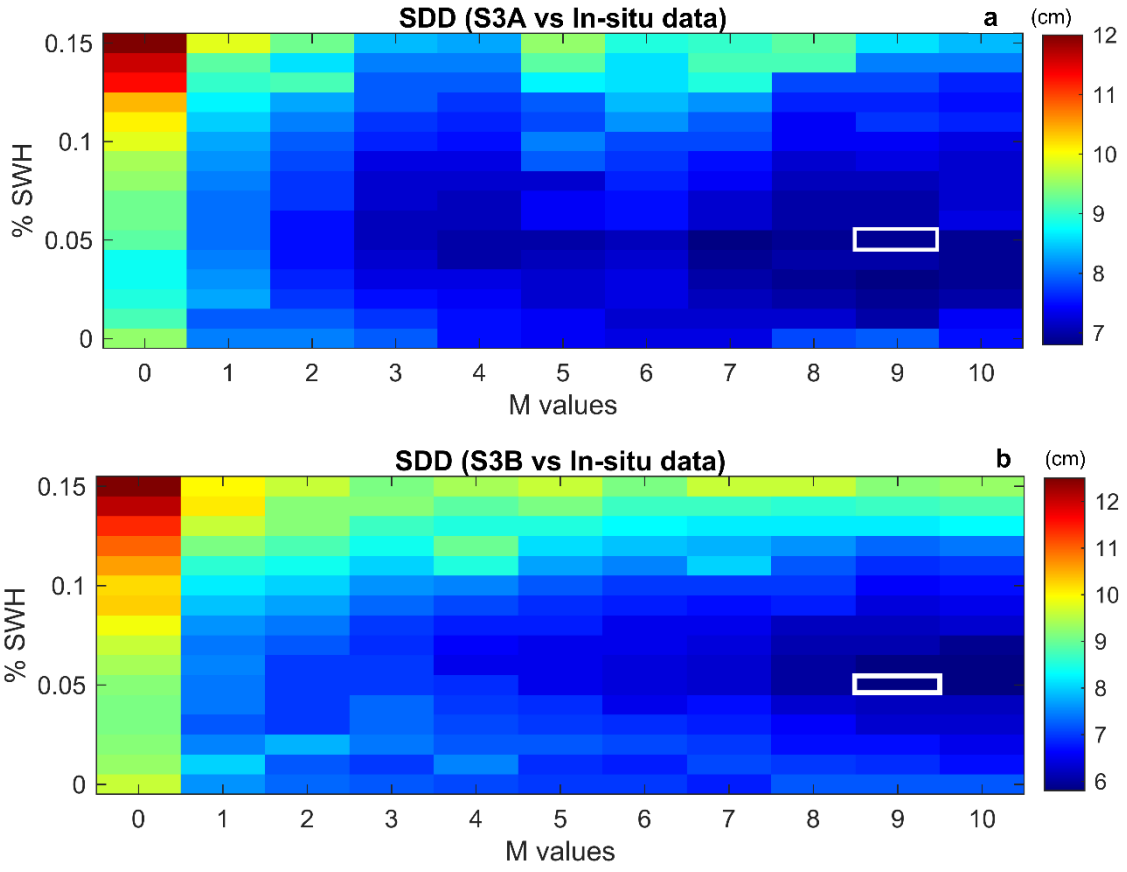


Figure 5.3 a SDD values for the series obtained by confronting the %SWH and M values for S3A. **b** SDD values for the series obtained by confronting the %SWH and M values for S3B. The M and %SWH combination selected is displayed with a white box. Minimum values of SDD are in dark blue and maximum in red.

5.5.2 Validation of SLA time series

Results are presented focusing on the agreement between altimeter and in-situ time series over monthly to seasonal periods, which represent the primary temporal scales of interest in this study. In the assessment of the sea level series from S3A altimeter against the in-situ data, the chosen combination of M (9) and SWH percentage (5%) resulted in an SDD of 6.9 cm, a MAD of 5.3 cm and an *r*-value value of 0.34. The confidence level derived from the *p*-value is 99.99%. **Figure 5.4** shows the final time series, with the altimeter SLA in red and the in-situ data in blue. The gaps in the figure represent either NaN values or missing data.

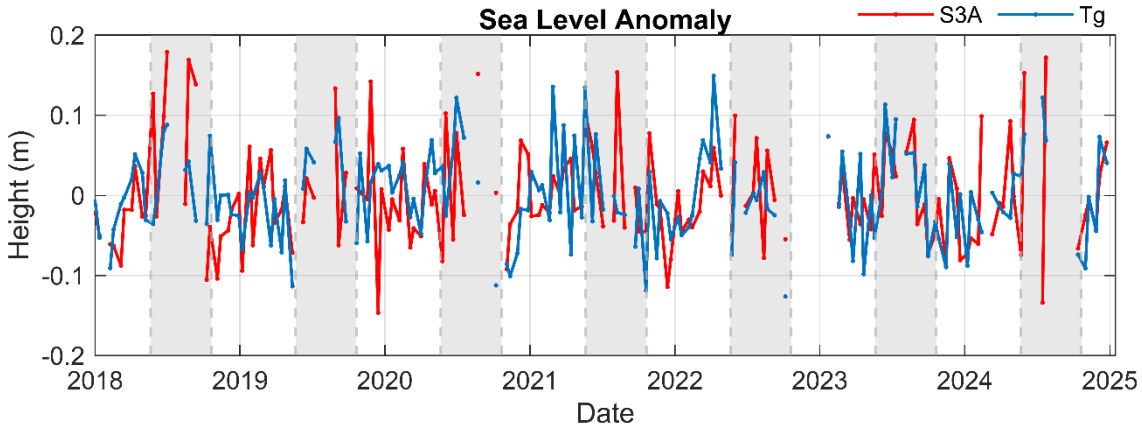


Figure 5.4 Detrended SLA of the S3A altimeter (red) and tide gauge (blue) after 10 iterations of removing data exceeding ±3σ. The gaps are NaN values that belong to the outliers or missing values. Shaded grey areas correspond to the Antarctic winters.

Regarding the comparison between the tide gauge and S3B data, the chosen combination of M (9) and %SWH (5%) resulted in an SDD of 5.8 cm, a MAD of 4.5 cm and an *r*-value of 0.37. Based on the *p*-value, the confidence level is estimated at 99.99%. **Figure 5.5** displays the final time series, with the altimetry SLA shown in green and the in-situ data in blue. Additionaly, the gaps in the figure represent either NaN values or missing data.

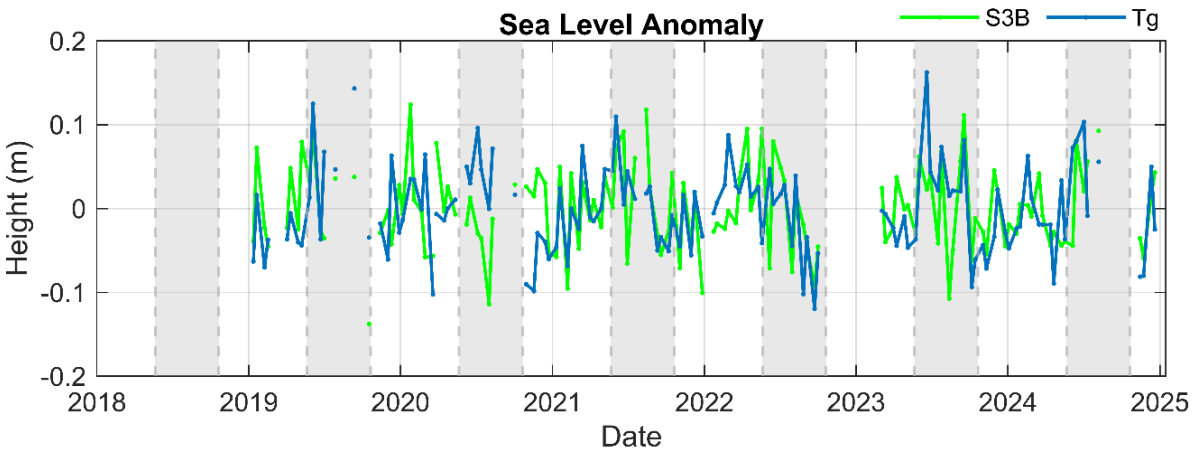


Figure 5.5 Detrended SLA of the S3B altimeter (green) and tide gauge (blue) after 10 iterations of removing data exceeding ±3σ. The gaps are NaN values that belong to the outliers or missing values. Shaded grey areas correspond to the Antarctic winters.

Sea ice affects the satellite radar signal, resulting in reduced quality of the return signal (Rose et al., 2019). In order to see if there is a relationship between the outliers found in the altimetric time series and the presence of sea ice that might occur during the southern winters, the percentage of invalid data during winters was calculated. In the final S3A series, 15.82% of the values (out of 177 overpasses) are classified as NaN, with 75% of these occurring during the autumn and winter months. Likewise, the final S3B dataset contains 13.3% missing data (from a total of 150 overpasses), of which 65% are also concentrated in the colder seasons.

Based on these results, the performance of the series was further evaluated by separating the data into two seasonal periods: spring/summer (23 September to 22 March) and autumn/winter (23 March to 22 September). This seasonal division reveals a notable improvement in agreement with tide gauge data during the warmer months. Specifically, the SDD between S3A and tide gauge decreases to 5.6 cm (corresponding MAD = 4.3 cm), and to 5.1 cm (MAD = 4.1 cm) for S3B and tide gauge. In contrast, during the colder season, the SDD increases to 8.1 cm (MAD = 6.4 cm) for S3A and 6.3 cm (MAD = 4.8 cm) for S3B.

5.6 Discussion

The comparison between altimetric SLA from S3A and S3B and in-situ tide gauge data revealed meaningful differences influenced by data processing parameters and seasonal variability. Altimetry and tide gauge measurements were matched within a maximum time difference of ±10 minutes to minimise temporal mismatch effects.

Firstly, the optimisation of SLA computation, specifically by varying the number of surrounding measurements (M) and the percentage of SWH used for sea state bias (SSB) correction, had a notable impact on the agreement with tide gauge observations. The lowest SDD was achieved with M = 9 and 5% SWH for both S3A and S3B. These outcomes highlight the importance of tuning altimetric processing parameters to enhance consistency with in-situ measurements. This is in line with previous studies that underscore the critical role of SSB correction in sea level estimation from different missions (Aldarias et al., 2020; Bonnefond et al., 2011; Fenoglio-Marc et al., 2015; Gómez-Enri et al., 2018; Valle-Rodríguez et al., 2023). The selected SWH percentages are also consistent with those reported in previous studies, including Fenoglio-Marc et al. (2015) and Aldarias et al. (2020). Other investigations have suggested slightly different optimal values, for example for CryoSat-2, Dinardo et al. (2018) reported 4.7% (SAR mode), while Valle-Rodríguez et al. (2023) estimated optimal values between 7% and 9% (LRM mode). Altogether, this evidence supports the use of a 5% SWH threshold as a commonly effective choice for S3A/B missions, though the ideal value may vary slightly depending on regional characteristics and local sea state dynamics.

To assess the advantage of the optimised approach, SLA was also computed using the SSB correction provided by EUMETSAT, which was specifically designed for Jason 2. The results show that, particularly for S3A, the SDD would increase to 7.3 cm if the default SSB correction were used in combination with M = 9 (and also an increase up to 6.4 cm for S3B). This comparison confirms that the customised configuration outperforms the standard product and highlights the added value of parameter tuning in improving agreement with in-situ observations.

Although these optimal configurations yielded relatively low discrepancies between both datasets, with MADs of 5.3 cm for S3A and 4.5 cm for S3B, and SDDs of 6.9 cm and 5.8 cm, respectively, the correlation coefficients remained moderate (r = 0.34 for S3A and r = 0.37 for S3B). This indicates that, while altimetry accurately captures the general sea-level signal, it does not fully reproduce the short-term variability observed by the tide gauges. However,

the confidence level associated with these correlations is 99.99% for both S3A and S3B, confirming that the relationship, though moderate, is statistically significant. Other authors have reported higher correlation values even in ice-affected regions, suggesting that better agreement is achievable under certain conditions (Auger et al., 2021; Fenoglio-Marc et al., 2015). The discrepancy may be attributed to the spatial averaging in altimetric measurements and potential residual errors due to sea ice contamination or geophysical corrections (Bonnefond et al., 2011; Ray et al., 2023; Vignudelli, 2011). In contrast, tide gauges, operating at fixed locations and with high temporal resolution, are more sensitive to local conditions. As noted by Vignudelli et al. (2019), Valle-Rodríguez et al. (2023), and others, the coastal zone is influenced by multiple local oceanic processes acting at different spatial and temporal scales. This reinforces the need to account for both the characteristics of the measuring instruments and the local oceanographic context when interpreting sea level data. In the case of Johnsons Cove, this difference could be accentuated by the continuous discharge of freshwater from the glacier in the vicinity of the tide gauge, which locally affects sea level.

Sea ice plays a significant role in degrading altimeter data quality, particularly during the austral winter, when its presence coincides with a marked increase in invalid or outlier measurements. In both Sentinel-3 missions, over 70% of missing values occurred in autumn and winter, underscoring the radar altimeter's sensitivity to icy conditions. This aligns with previous studies showing that sea ice interferes with the satellite radar signal, reducing return quality and causing waveform retracking errors (Peng et al., 2024; Prandi et al., 2012; Rose et al., 2019). A seasonal analysis reinforces this effect: agreement with tide gauge data improves notably during ice-free months, with standard deviations of differences (SDDs) dropping to 5.6 cm for S3A and 5.1 cm for S3B in spring and summer. This highlights the importance of accounting for sea ice in polar altimetry and suggests that future processing chains could benefit from dynamic masking or enhanced retracking algorithms tailored to icy surfaces (Passaro et al., 2021; Venables et al., 2023).

To investigate whether the outliers detected can be attributed to the presence of sea ice, Sentinel-1 SAR images corresponding to the dates of the outliers were acquired from Copernicus Browser to visually confirm the presence of ice in the study area. A total of five images were acquired for S3A and seven for S3B. In parallel, Sentinel-3 Level-1B altimetry data, also coincident with the anomalous observations, were retrieved to analyse the associated waveforms as other authors have done previously (Fredensborg Hansen et al., 2021; Mugunthan et al., 2023; Tang et al., 2023). Open water waveforms show a single sharp

peak with a steep rise and gradual decay, while mixed or irregular surfaces can produce more complex, multi-peaked shapes (Mugunthan et al., 2023). An example for ice conditions of S3A and S3B data is presented below.

In the case of S3A, the day 04/09/2021 was chosen, **Figure 5.6a** shows the sea ice situation with a Sentinel-1 SAR image, in which the black colour seems to correspond to open ocean, while the greys and their undertones consolidated sea ice or sea ice in formation. **Figure 5.6b** shows the track section that is used for the SLA calculation, and thus the section to be visually analysed. The SLA from the study section is shown in **Figure 5.6c**. Three points (1, 5, and 16) were selected for analysis. Points 1 and 5 might be considered representative of typical SLA values (**Figure 5.4**), while point 16 corresponds to an anomalous value. The waveforms associated with these points are shown for comparison (**Figure 5.6d**). All three waveforms exhibit a bimodal shape, characterized by two distinct peaks associated with icy surfaces, with the effect being more pronounced at position 5 (Shu et al., 2020). As noted by authors such as Tang et al. (2023), this pattern may result from impurities or air bubbles within the ice. In addition, it can be observed that the anomalously high SLA value at position 16 corresponds to a leftward shift of the waveform, indicating that the leading edge appears earlier than expected.

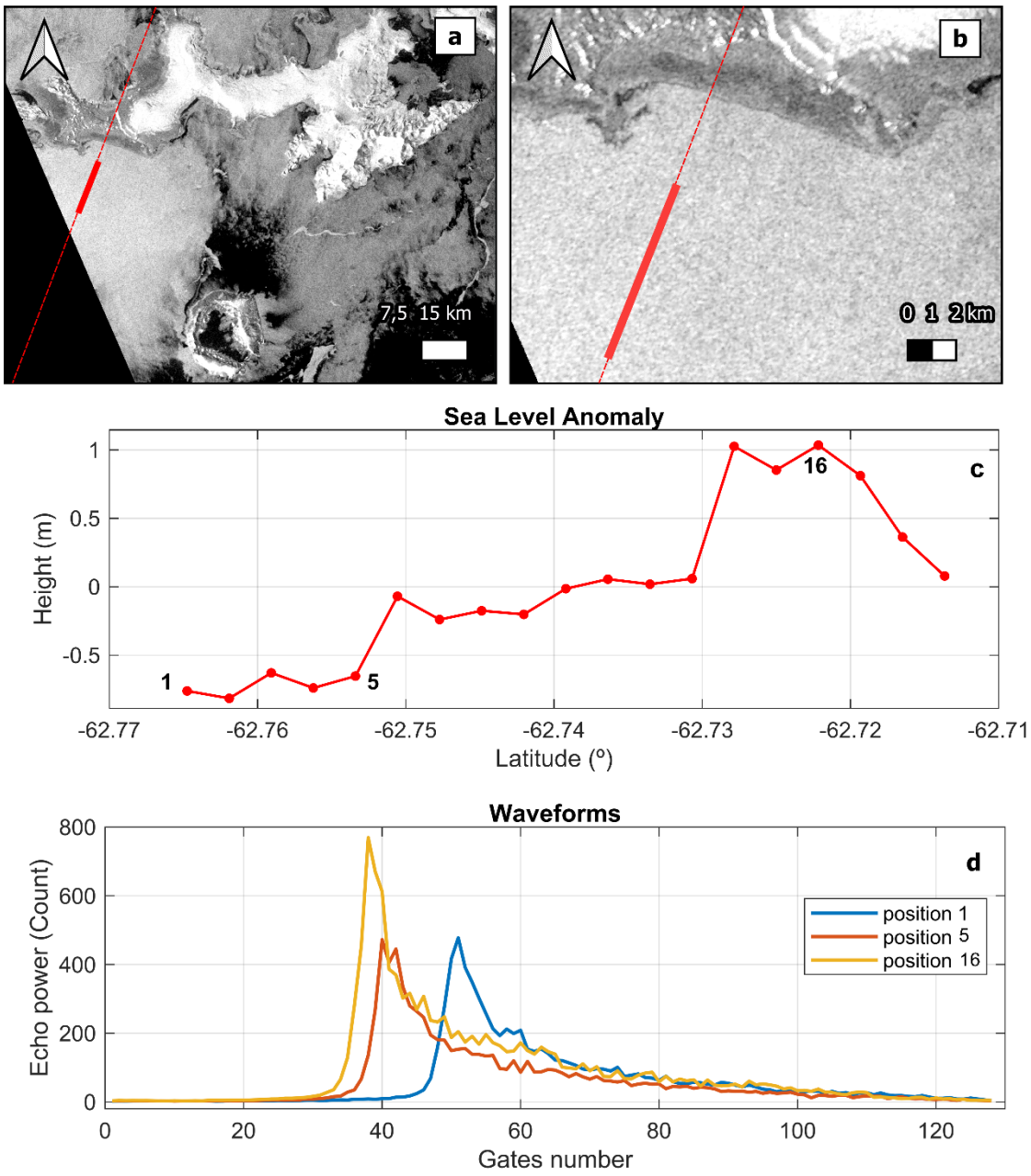


Figure 5.6 a SAR image of Livingston Island obtained with Sentinel-1 (04/09/2021). The red line is the descending track #052 of S3A. **b** Zoom-in of the study area. **c** SLA along the study section (Figure 5.6b, red continuous line). Numbers (1, 5 and 16) mark analysed positions. **d** S3A SAR waveforms from Level-1B data.

With regard to S3B, the date 24/09/2020 was selected. **Figure 5.7a** illustrates the sea ice conditions for that day. **Figure 5.7b** highlights the portion of the track used for SLA computation and selected for visual inspection. **Figure 5.7c** shows the SLA values along the studied track section, where points 5, 11, and 13 were selected due to their anomalously low SLA values. For these three points, the corresponding waveforms are shown in **Figure 5.7d**. All three waveforms exhibit a bimodal structure, and a noticeable rightward shift in the

waveform is observed when SLA decreases. This waveform pattern is consistent with previous descriptions of returns affected by growing or consolidating sea ice (Mugunthan et al., 2023; Shu et al., 2020).

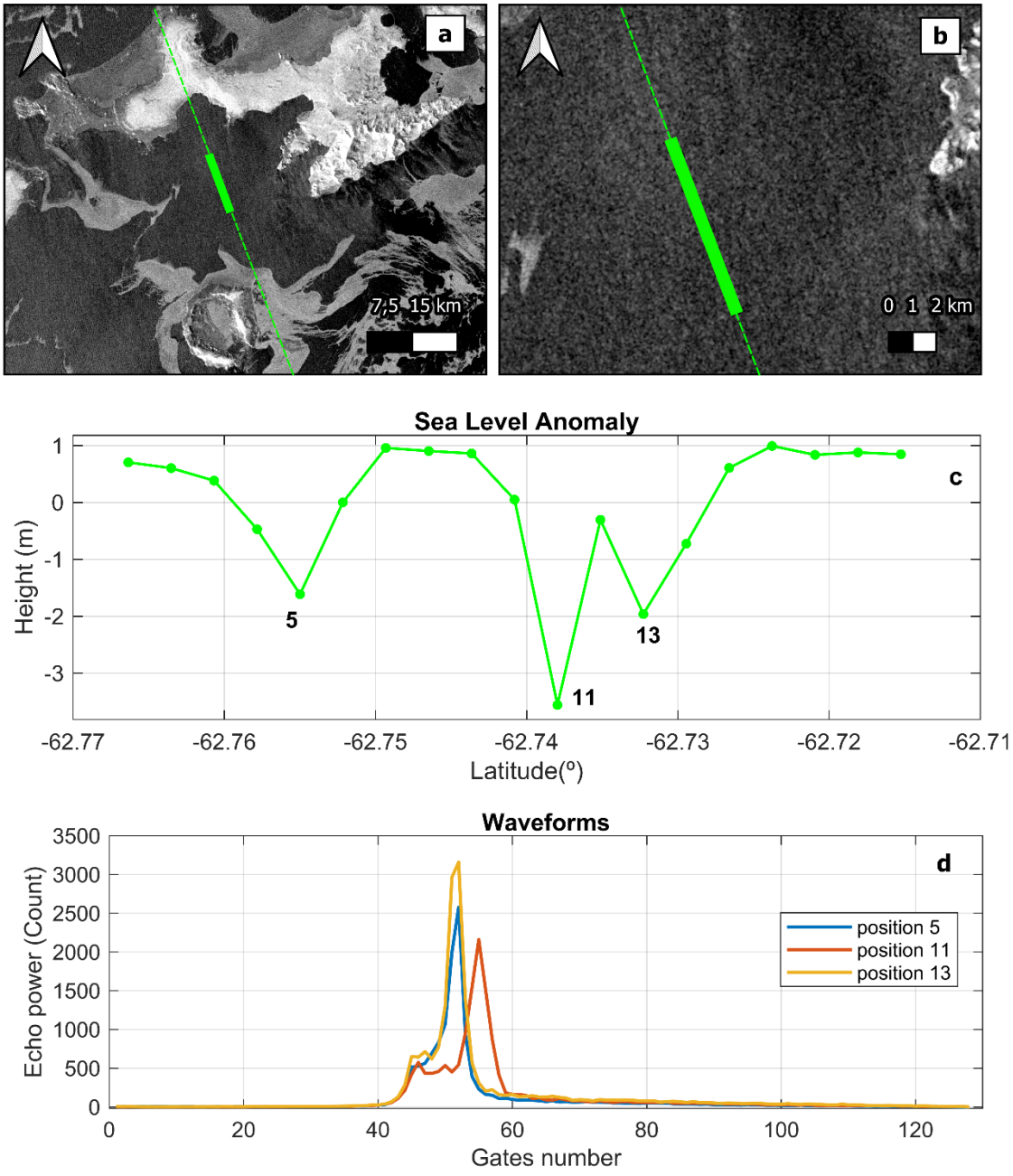


Figure 5.7 a SAR image of Livingston Island obtained with Sentinel-1 (24/09/2020). The green line is the ascending track #374 of S3B. **b** Zoom-in of the study area. **c** SLA along the study section (Figure 5.7b, green continuous line). Numbers (5, 11 and 13) mark analysed positions. **d** S3B SAR waveform from Level-1B data.

Although sea ice conditions can vary significantly over short timescales, the waveforms observed appear to correspond to areas covered by sea ice. In the case of S3A, the time difference between the Sentinel-1 SAR image and the Sentinel-3 overpass is approximately 20 hours, while for S3B, the offset is around 12 hours. Despite these temporal mismatches, the waveform signatures, particularly their bimodal shape and shifts, are consistent with those expected over ice-covered surfaces, supporting the interpretation that sea ice is influencing the observed SLA anomalies. These results are consistent with previous studies (Mugunthan et al., 2023; Shu et al., 2020; Tang et al., 2023), reinforcing the hypothesis that SLA outliers during the austral winter are influenced by the presence of sea ice, compromising their reliability for oceanographic applications if not properly filtered or corrected.

5.7 Conclusions

This study demonstrates the relevance of optimising SLA processing parameters, particularly the number of measurements and SSB correction percentage, to improve consistency between satellite altimetry and tide gauge observations. The use of a 5% SWH threshold proved effective for both S3A and S3B, supporting findings from previous studies.

Both SDD and MAD values were relatively low (6.9 and 5.1 cm for S3A, and 5.8 and 4.5 cm for S3B, respectively), indicating good overall agreement between the altimetric and in-situ sea-level data. However, the correlation coefficients remained moderate, suggesting that the altimetry captures the general sea-level signal but not the full short-term variability observed by the tide gauges. The most significant factor affecting data quality could be the presence of sea ice. More than 70% of invalid or outlier SLA observations occurred during the austral autumn and winter, coinciding with periods of sea ice formation. Sentinel-1 SAR imagery and Sentinel-3 radar waveforms confirmed the presence of ice on dates with anomalous altimeter returns, supporting the conclusion that sea ice contamination degrades waveform quality and affects SLA retrieval.

Seasonal analysis further demonstrated that altimetry and tide gauge agreement improved substantially during ice-free months, with standard deviations decreasing to 5.6 – 5.1 cm approximately. These results emphasise the need to consider ice presence in polar altimetry studies and suggest that future approaches could benefit from adaptive retracking algorithms or dynamic masking techniques tailored for icy surfaces.

5.8 Connecting text

The results of this chapter highlight the influence of sea ice on the quality of satellite altimetry records, underscoring the importance of considering environmental factors when interpreting sea level variability in polar regions. Among these factors, seawater temperature plays a central role through its impact on density, seasonal ice formation, and freshwater input from glacial melt. To address this, Chapter 6 focuses on the establishment and analysis of long-term temperature records at Livingston and Deception Islands.

CHAPTER 6

Long-term seawater temperature records at Livingston and Deception Islands, Antarctica

This study investigates seawater temperature patterns on Livingston and Deception Islands in Antarctica, where LIVMAR and DECMAR oceanographic stations are located, respectively. The research spans the period from 2015 to 2024, focusing on seasonal variations, long-term trends, and differences between the two stations. Over these eight years, minimum temperatures have decreased, with DECMAR notably failing to record temperatures below the freezing point during the last two winters. The analysis reveals pronounced seasonality in both locations, with higher temperature peaks during the austral summer. DECMAR consistently registers higher maximum temperatures compared to LIVMAR, attributed to the volcanic activity of Deception Island. This volcanic influence introduces thermal anomalies, delays in minimum temperature occurrence, and greater variability in summer signals due to increased subsurface water flow within the volcanic plumbing system. During the austral winters, the stations exhibit distinct patterns. LIVMAR shows earlier and more variable temperature drops, while DECMAR demonstrates shorter but more stable freezing periods. These differences may result from freshwater input from the Johnson Glacier, which modifies local freezing conditions at Livingston Island, combined with the geothermal influence of Deception Island. The study also identifies an overall upward trend in seawater and air temperatures, aligning with global and regional climate change patterns. The reduction in the frequency of extreme low temperature events that occurred between 2020 and 2022 during the volcano-tectonic event in the Bransfield Strait due to the eruption of the Orca volcano highlights the environmental changes affecting the South Shetland Islands region. This work underscores the importance of local geophysical processes, such as volcanic activity and glacier melt, in the regional thermal dynamics. While the similarities between LIVMAR and DECMAR reflect overarching climatic drivers, the observed differences illustrate the complexity introduced by local factors.

Luengo-S, O., Rosado, B., Jiménez-Morales, V., De Gil, A., Gómez-Enri, J., Bruno, M., & Berrocoso, M. (2025). Long-term seawater temperature records at Livingston and Deception Islands, Antarctica. Frontiers In Marine Science, 12. https://doi.org/10.3389/fmars.2025.1566852

6.1 Statement of the chapter

This article aims to present a detailed analysis of seawater temperature dynamics around Deception Island, an active volcanic system, and Livingston Island, a non-volcanic landmass, both located within the South Shetland Archipelago, Antarctica. Based on a decade-long dataset, the study examines temporal variations in seawater temperature and investigates the influence of volcanic activity, geodynamic processes, and climatic factors. The findings provide valuable insights into the local and regional drivers of thermal variability in Antarctic waters.

6.2 Study area

A detailed description of the study area can be found in Chapter 3.

6.3 Data

This chapter makes use of water temperature series from the LIVMAR and DECMAR stations, and atmospheric temperature series from the JCI and GdC stations, all described in Section 4.1. These datasets were recorded at 10-minute intervals and cover the period from 2015 to 2024. As a reference, **Figure 6.1** presents the atmospheric temperature data from the meteorological stations, while the complete set of seawater and atmospheric temperature time series is presented and analyzed in the Results section.

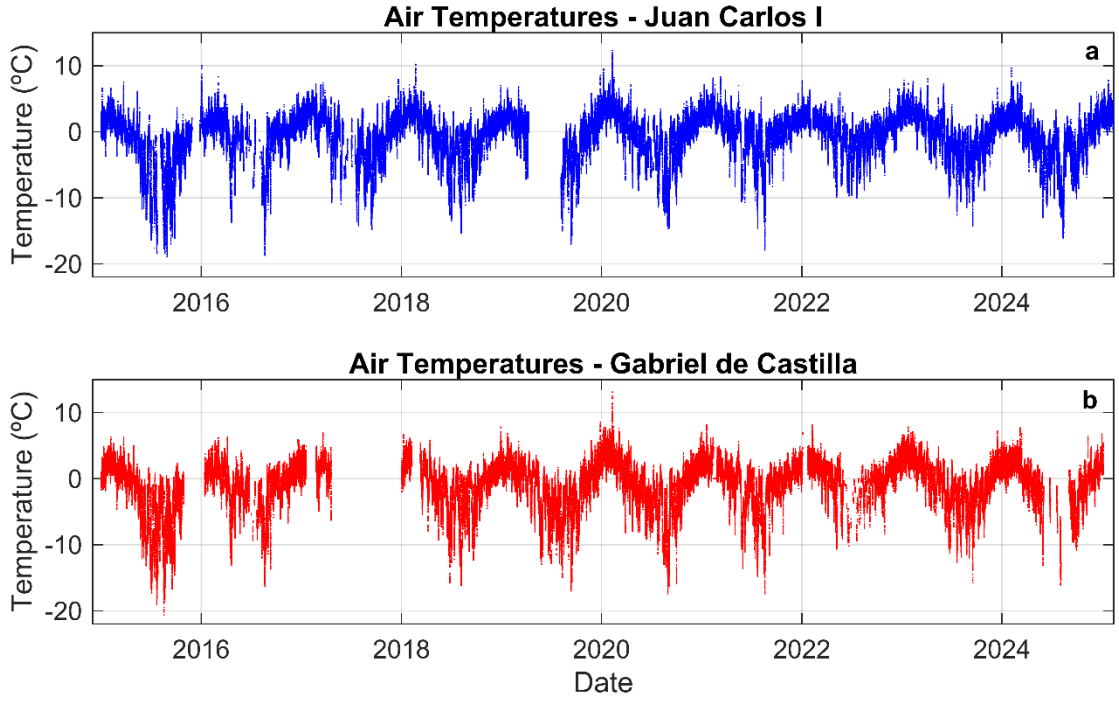


Figure 6.1 a Air temperature at Livingston Island sampled every 20 min from December 2015 to December 2024 (JCI, blue). **b** Air temperature at Deception Island sampled every 20 min from December 2015 to December 2024 (GdC, red). The gaps in the record are due to missing or anomalous data.

6.4 Methodology

The series are obtained on an annual basis, with the initial step involving the merging of the data. Once continuous data were established, both descriptive and analytical analyses were performed. Furthermore, monthly temperature averages were calculated to offer a more detailed foundation for the analysis, thereby facilitating the identification of seasonal trends and patterns.

Moreover, the temperature series were analysed using the procedure followed by an STL (Seasonal and Trend decomposition procedure based on LOESS) decomposition. The STL method is an iterative technique that decomposes time series data into three components: trend, seasonality, and residuals. It allows for flexibility in specifying the amount of variation in the trend and seasonal components and produces robust estimates that are not distorted by transient outliers (Cleveland et al., 1990; Sanchez-Vazquez et al., 2012). The core of STL is the use of LOESS smoothing, a local polynomial regression technique, to estimate these components iteratively. The STL procedure comprises two iterative stages: internal and external. First, the seasonal component is estimated by grouping data points based on their seasonal indices (e.g., months or weeks) and applying LOESS smoothing to capture periodic

variations. This seasonal component is subtracted from the original data to isolate a preliminary trend-cycle component, which is further smoothed over a larger window to estimate the trend. Finally, the residuals are calculated by removing the trend and seasonal components from the original data. These steps are repeated iteratively, refining each component until convergence is achieved. To carry out this decomposition of the series, it was adapted the R program developed by Hafen, (2016) based on the description of the methodology of Cleveland et al. (1990).

In addition, the Root Mean Squared Error (RMSE) and Pearson's correlation coefficient (*r*) between the DECMAR/LIVMAR and GdC/JCI series were calculated in order to see their similarity.

6.5 Results

6.5.1 Temperature time series

The temperature series for both islands since 2011 are shown below (**Figure 6.2**), in this and the following figures, blue represents LIVMAR station (**Figure 6.2a**) and red DECMAR station (**Figure 6.2b**); gaps in the series represent the lack of data. Before starting the comparison between islands, it should be noted that during the austral winter of 2012, at DECMAR station recorded anomalous temperatures, reaching peaks of up to 10 °C (**Figure 6.2b**). The detection was favoured, as it started during the austral winter when Puerto Foster was covered by sea ice, thereby reducing heat exchange at the water-atmosphere interface (Berrocoso et al., 2018). According to this study, these anomalies result from the periodic advection of water previously heated in the island's interior by the injection of submarine magma, which aligns with the higher volcanic activity recorded. Given the presence of sea ice within the bay during the winter of 2018, which inhibited heat loss through water-atmosphere exchange, Berrocoso et al. (2018) confirmed that water masses passing through the Fumarole Bay area warmed significantly and exhibited notable peaks when exiting the bay, coinciding with low tide. This is consistent with the circulation patterns described by Flexas et al. (2017). However, in other winters, such favourable conditions were not observed, and no volcanic activity of comparable magnitude was recorded.

Except for 2012 austral winter at DECMAR, the rest of the years show a clear seasonal variation, reaching the minimums during the austral winter and the maximums in the austral summer. However, the two islands differ in magnitude. Deception reaches higher temperatures during summers (around 4 °C) than Livingston (2 °C). During winters,

temperatures are similar, but have a longer duration in Livingston, this could be due to local behaviour as Deception Island is a volcano.

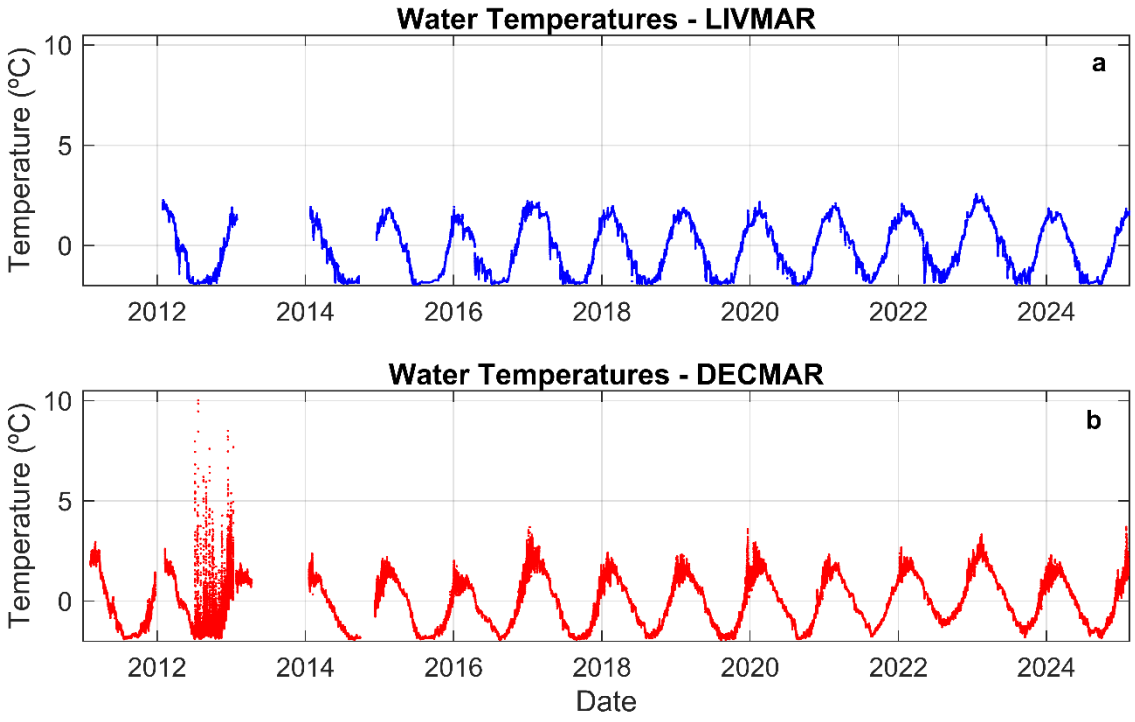


Figure 6.2 a Water temperature series at LIVMAR station (blue). **b** Water temperature series at DECMAR station (red), where temperature anomalies are due to volcanic activity. Gaps in the graphs are due to missing data caused by equipment power failures.

The analysis now focuses on December 2014 to February 2025 as this is the time period for which continuous data from both stations are available (LIVMAR **Figure 6.3a** and DECMAR **Figure 6.3b**). The highest recorded temperatures at LIVMAR occurred during January 2023 (2.59 °C). Regarding DECMAR, the highest temperature is 3.69 °C, observed in January 2017 and January 2025. The lowest temperatures recorded were for DECMAR -1.94 °C in August 2017 and for LIVMAR -1.97 °C in August 2020.

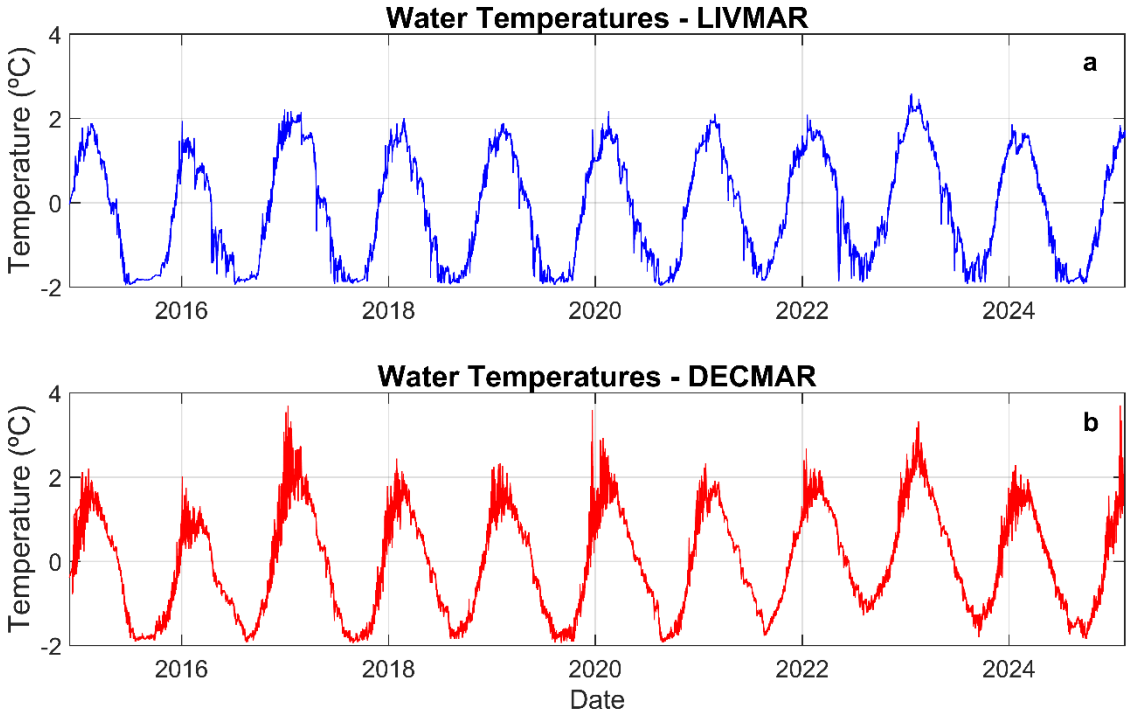


Figure 6.3 a Water temperature records for the period December 2014 to February 2025 at stations LIVMAR (blue). **b** Water temperature records for the period December 2014 to February 2025 at DECMAR station (red).

The temperatures recorded during the austral summers (**Figure 6.4a**) exhibit a similar pattern on both islands. However, temperatures are consistently higher at DECMAR (1.1 °C approximately more than LIVMAR), which could be due to the volcanic character of the island. For both islands, the first two summers (2014/2015 and 2015/2016) recorded the lowest temperatures, while the summers of 2016/2017, 2019/2020, and 2022/2023 saw the highest temperatures.

Focusing now on the lows (**Figure 6.4b**), minimum temperatures are first reached in LIVMAR station in June or July, instead in DECMAR station occurs in July or August; the rise in temperature is usually on similar dates. Based on the salinities recorded during an austral summer on both islands (Vidal et al., 2012), it could be established that in the bays where the oceanographic stations are located the freezing point is around -1.8 °C. During the austral winters of 2015 and 2017, both islands experienced the longest period with temperatures near to the freezing point (**Figure 6.4**). On both islands the duration of low water temperatures during the austral winter is variable. As can be seen in **Figure 6.4**, during the austral winters of 2021, 2022 and 2023 in Deception Island there were no occurrences of temperatures below -1.8 °C. However, during the winter of 2024 temperatures below -1.8 °C

appears again at DECMAR. Periods of temperatures below -1.8 °C, although shorter in DECMAR, are more continuous than in LIVMAR, where temperatures below -1.8 °C start earlier but oscillate.

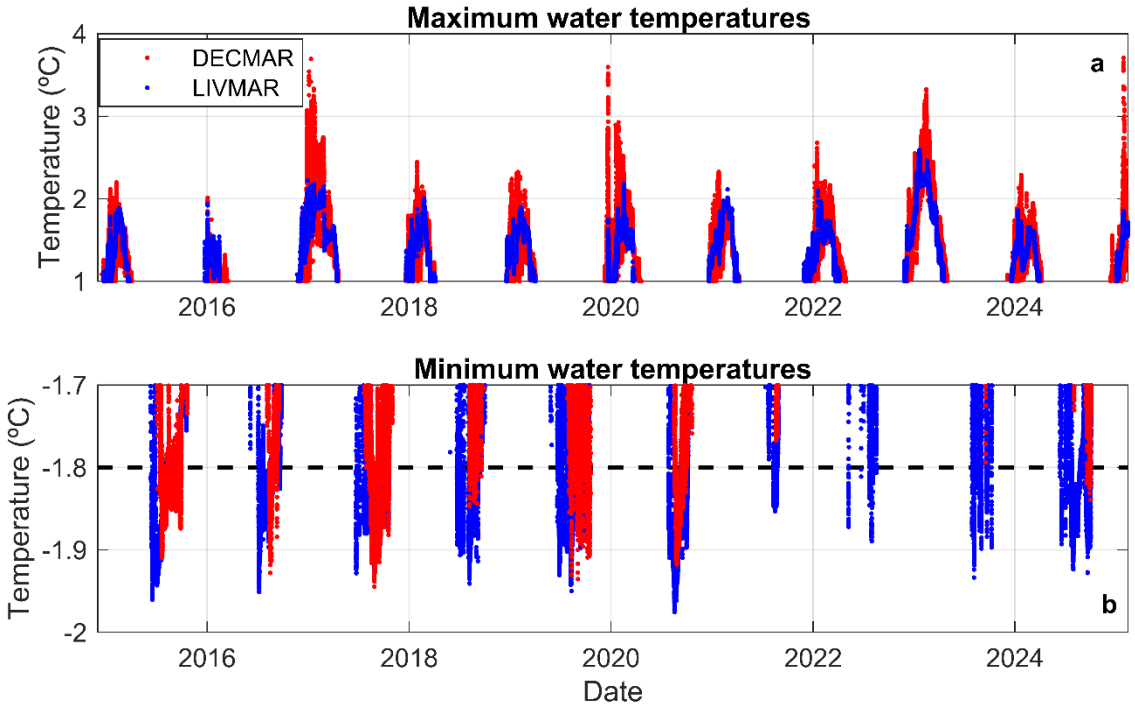


Figure 6.4 a Maximum water temperature records at LIVMAR (blue) and DECMAR (red) stations during austral summers between December 2014 to February 2023. **b** Water temperature records below -1.8 °C at LIVMAR (blue) and DECMAR (red) stations during austral winters between December 2014 to February 2023. The black dashed line indicates a temperature of -1.8 °C, the freezing point.

For a more comprehensive analysis of the summer seasons, they have been plotted overlapping in **Figure 6.5** (DECMAR red and LIVMAR blue), where beginning and end of the austral summer are indicated by vertical dashed lines. DECMAR station shows more oscillations in maximum temperatures than LIVMAR, reaching oscillations of up to 1.44 °C by January 2020 (**Figure 6.5f**). Despite these differences in the magnitude of the temperature oscillations between stations, they behave in a similar way, since when the temperature rises or falls in one of the stations it occurs in the other, although with a different amplitude. This can be clearly seen in **Figure 6.5b**, for example, that when the temperature drops in February 2016 it also drops at DECMAR; and in **Figure 6.5f** when it rises at DECMAR in December 2019 it also rises at LIVMAR, although to a lesser extent.

Also, maximum temperatures have decreased over the years, and DECMAR oscillations have decreased, but this could be due to volcanic activity. It could be suggested that the

summer season is brought forward each year with the exception of summer 2016/2017. Pre-summer temperatures increase earlier at LIVMAR than at DECMAR.

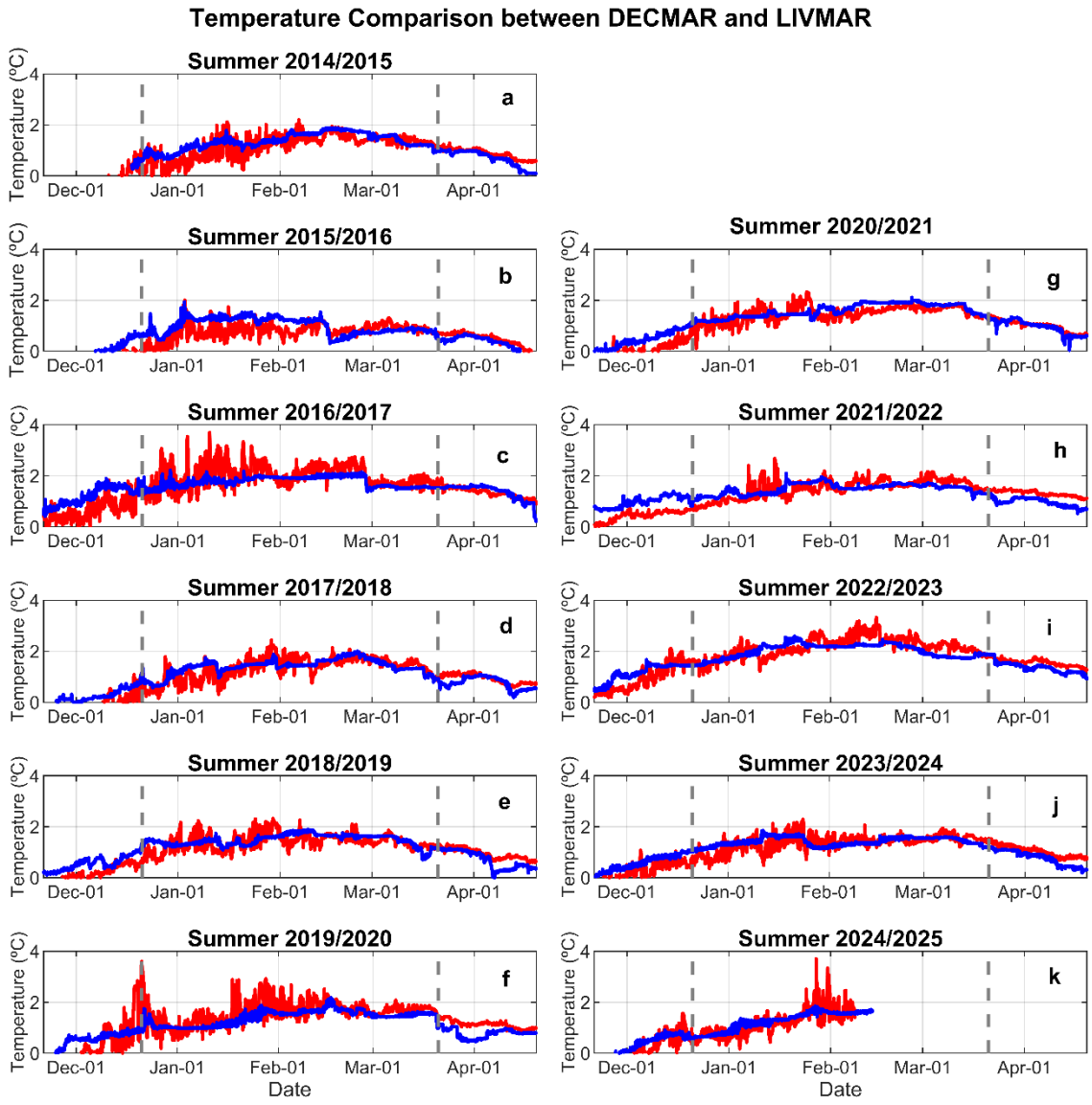


Figure 6.5 Graphs of austral summers from 2014 to 2025 are presented. The red lines represent the DECMAR station, while the blue lines correspond to the LIVMAR station. The dashed vertical lines mark the start and end of the austral winter (December 21 and March 20, respectively). November and April are also included to show the temperature trends before and after summer.

To provide a clearer understanding of the austral winter, **Figure 6.6** presents an overlay of water temperatures for both stations (DECMAR in red and LIVMAR in blue) from November to October each year. These months were chosen to encompass the winter season as well as an additional month at the start and end, offering a more comprehensive view. In

this figure, grey shadow zone indicates temperatures below -1.8 °C and vertical dashed lines austral winter.

From 2015 to 2017 (**Figure 6.6a**, **Figure 6.6b** and **Figure 6.6c**), winter temperatures were more stable and consistently lower, with the onset of cooler temperatures occurring slightly later each year. From 2018 onwards, temperatures became more variable, with greater fluctuations throughout the winter months. The winters of 2019 (**Figure 6.6e**) and 2020 (**Figure 6.6f**) exhibited somewhat more stability in parts of the season. However, in 2021 (**Figure 6.6g**) and 2022 (**Figure 6.6h**), temperatures declined only marginally, failing to reach the minimums observed in DECMAR.

The most notable difference between the two stations is that DECMAR consistently exhibits higher temperatures than LIVMAR and reaches its minimum temperatures later. These graphs also confirm that at LIVMAR low temperatures appear later and later each year, starting in early July in 2016 (**Figure 6.6b**) and in mid-August in 2022 (**Figure 6.6h**). DECMAR is more unstable due to its volcanic nature, however, LIVMAR also presents oscillations. During the winter of 2024 it seems that both islands start to recover their usual behaviour reaching temperatures below -1.8 °C again at DECMAR and more continuously at LIVMAR.

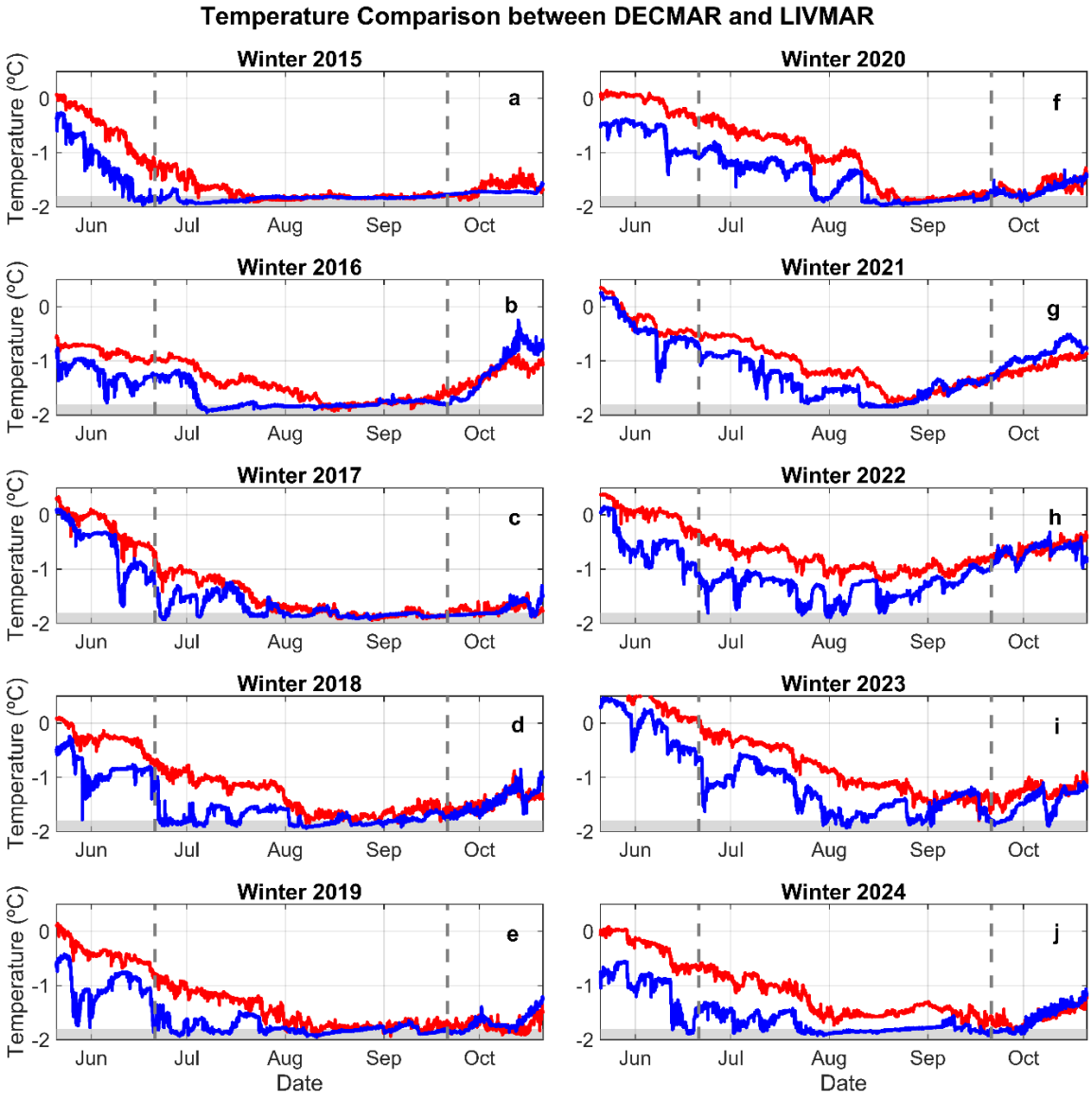


Figure 6.6 Graphs of austral winters from 2015 to 2024 are presented. The red lines represent the DECMAR station, while the blue lines correspond to the LIVMAR station. The shaded grey area highlights temperatures below -1.8°C. The dashed vertical lines mark the start and end of the austral winter (June 22 and September 23, respectively). May and October are also included to show the temperature trends before and after winter.

If the number of records of temperatures below -1.8 °C were classified into days, **Figure 6.7** would be obtained. This figure shows a general decrease in the number of such records over the years for both stations, although this trend is not continuous. The two islands show similar patterns, with the exception of 2020, during which the number of records decreases at LIVMAR but increases at DECMAR. In 2021 and 2022, LIVMAR records its lowest values, while DECMAR does not record any temperatures below this threshold. As it was said previously, during winter of 2024 it seems to be recovering to normal.

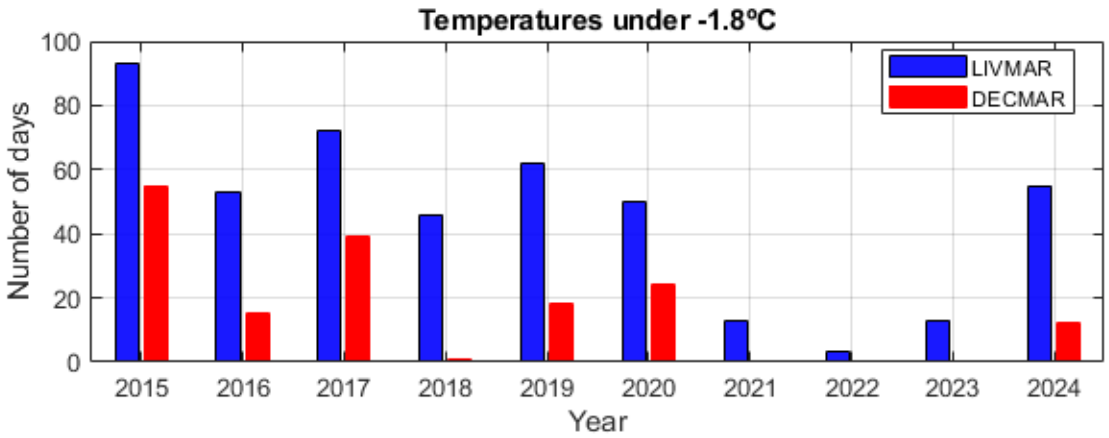


Figure 6.7 Evolution over the years of the number of data in which the temperature record temperatures equal to or below -1.8 °C for each station. LIVMAR station is blue and the DECMAR station is red. From 2021 to 2023 there is no data under -1.8 °C at DECMAR station.

Figure 6.8 shows the monthly means for both islands from January 2015 to December 2024. Monthly averages have been made for each station to see the behaviour over the years, a minimum of 90% of the total data was required for a 20-minute sampling frequency to compute the monthly average.

In both graphs (LIVMAR and DECMAR, **Figure 6.8a** and **Figure 6.8b**), the red line represents the monthly mean, and a trend of increasing winter temperatures has been observed in recent years. During summer, maximum temperatures in DECMAR are consistently higher than in LIVMAR, reaffirming the influence of volcanic activity on Deception Island.

In the early years of the record (2015–2017), winter temperatures reached lower values; however, in more recent years, there has been a decline in the occurrence of extremely cold temperatures. In DECMAR, winter temperatures barely reach the -1.9 °C threshold in recent years, indicating a reduction in the duration of periods with temperatures near seawater freezing levels.

In LIVMAR, the standard deviation narrows in winter, particularly in August, suggesting lower variability and greater thermal stability. In contrast, DECMAR exhibits a wider and relatively consistent standard deviation throughout the year, except between March and May, when it decreases. This indicates that temperatures in DECMAR are more variable, likely due to the influence of volcanic and oceanographic processes. Notably, the months exhibiting the most pronounced temperature differences are from October to December in LIVMAR, and from July to December in DECMAR.

Moreover, DECMAR has shown a more pronounced increase in summer temperatures in recent years (2021/2024). In LIVMAR, variations are more stable, with a lower amplitude of fluctuation, reinforcing the idea that DECMAR's thermal dynamics are more strongly influenced by geothermal factors.

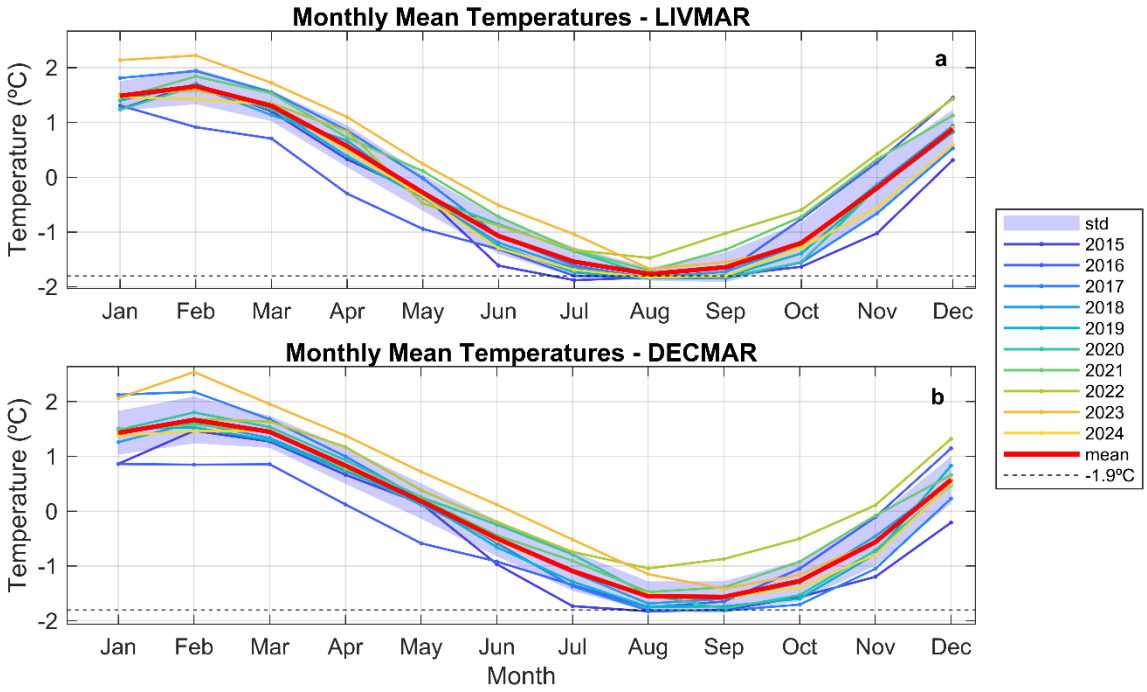


Figure 6.8 a Monthly averages of water temperatures from January 2015 to December 2024 at LIVMAR station. The blue shaded area corresponds to the standard deviation. **b** Monthly averages of water temperatures from January 2015 to December 2024 at DECMAR station. The black dashed line indicates a temperature of -1.8 °C, the freezing point. The blue shaded area corresponds to the standard deviation and red line to the mean of all years.

Subsequently, the monthly averages for both stations are presented together (**Figure 6.9**). As observed with the 20-minute interval temperature data, the behaviour of temperatures at both stations in the monthly means is remarkably similar, likely reflecting regional climatic patterns. At the LIVMAR station, temperatures decrease earlier than at DECMAR as the winter season sets in, and also reach lower values. These differences fluctuate over the years, with the most significant disparity occurring in 2022. For minimum temperatures, the graph clearly shows that winters are getting shorter and temperatures are gradually increasing in the winters of 2021, 2022 and 2023, with a recovery in 2024. Maximum temperatures tend to occur at the DECMAR station, but these too exhibit variability, which may be influenced by local factors, particularly the volcanic characteristics of Deception Island. Furthermore, it is again that temperatures are rising in both stations.

After the winter period, temperatures begin to rise earlier at LIVMAR. Although DECMAR recorded the highest values in the previous analysis of the 20-minute interval temperatures, when assessing the monthly averages, the temperatures between the two island stations become more comparable. While DECMAR consistently reaches the highest maxima, over the years, the station with the highest monthly average during spring and summer shifts between the two islands.

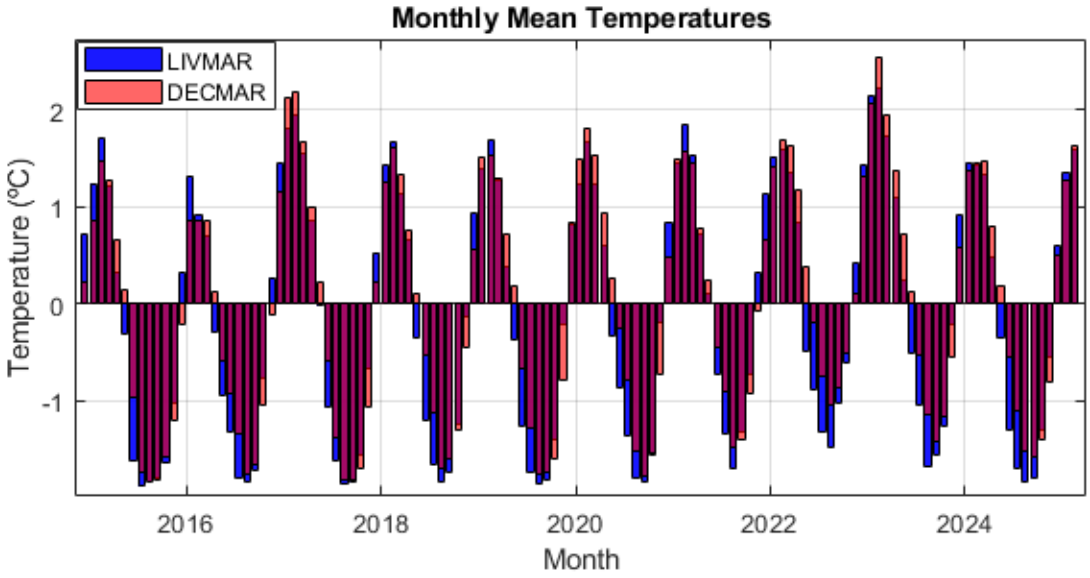


Figure 6.9 Monthly mean temperatures superimposed of LIVMAR (blue) and DECMAR (red) stations.

6.5.2 Statistical description of the series

The STL decomposition has been applied to the temperature time series of the DECMAR and LIVMAR stations (**Figure 6.10**). The results, displayed from top to bottom, include: the raw temperature series (**Figure 6.10a**), the trend (**Figure 6.10b**), the seasonality (**Figure 6.10c**), and the residuals (**Figure 6.10d**).

As illustrated in **Figure 6.10b**, the trends of both series exhibit similar behaviours, with notable exceptions in the maximum peaks of DECMAR during the summers of 2017 and 2020, and abrupt changes in the minimum temperatures of LIVMAR during the winter of 2022. Additionally, throughout 2022, a noticeable rise in the DECMAR trend is observed in comparison to that of LIVMAR. Additionally, temperature variations in DECMAR and LIVMAR were analysed in specific time intervals to evaluate the impact of the geodynamic of the Bransfield rift over the seawater series (see **Table 6.1**). Three distinct phases can be observed: the first (2015/2017) is characterized by strong fluctuations, with a trend increase followed by a decrease between 2016 and 2017. The second phase (2018/2022) shows a

constant upward trend, reaching its peak between 2021 and 2022. Finally, the third phase (2023/2025) exhibits a downward trend, eventually stabilizing at levels similar to those of 2018.

Table 6.1 Slope (°C/year) and total temperature change (°C) for each period.

	Slope (°C /year)		**Change in temperature (°C)**	
	DECMAR	LIVMAR	DECMAR	LIVMAR
2015/2017	0.15	0.13	0.61	0.51
2018/2022	0.11	0.10	0.70	0.60
2023/2025	-0.10	-0.20	-0.10	-0.2

Through the application of the STL, it is once again evident that the seasonality of both islands is pronounced, with slight variations between them (**Figure 6.10c**). The seasonality recorded at DECMAR shows a specific pattern during the months of December and January with large temperature oscillations during which the maximum annual temperatures are reached. However, in LIVMAR, despite reaching its maximums also in this period, it does not show oscillations of such magnitude.

The remainder of both series (**Figure 6.10d**) reveal significant differences. On one hand, LIVMAR has a constant noise throughout the series with some small exceptions during the summers. On the other hand, DECMAR has a similar behaviour to LIVMAR during the winters, while in the summers there is more noise as a consequence of the large oscillations described in **Figure 6.10c**.

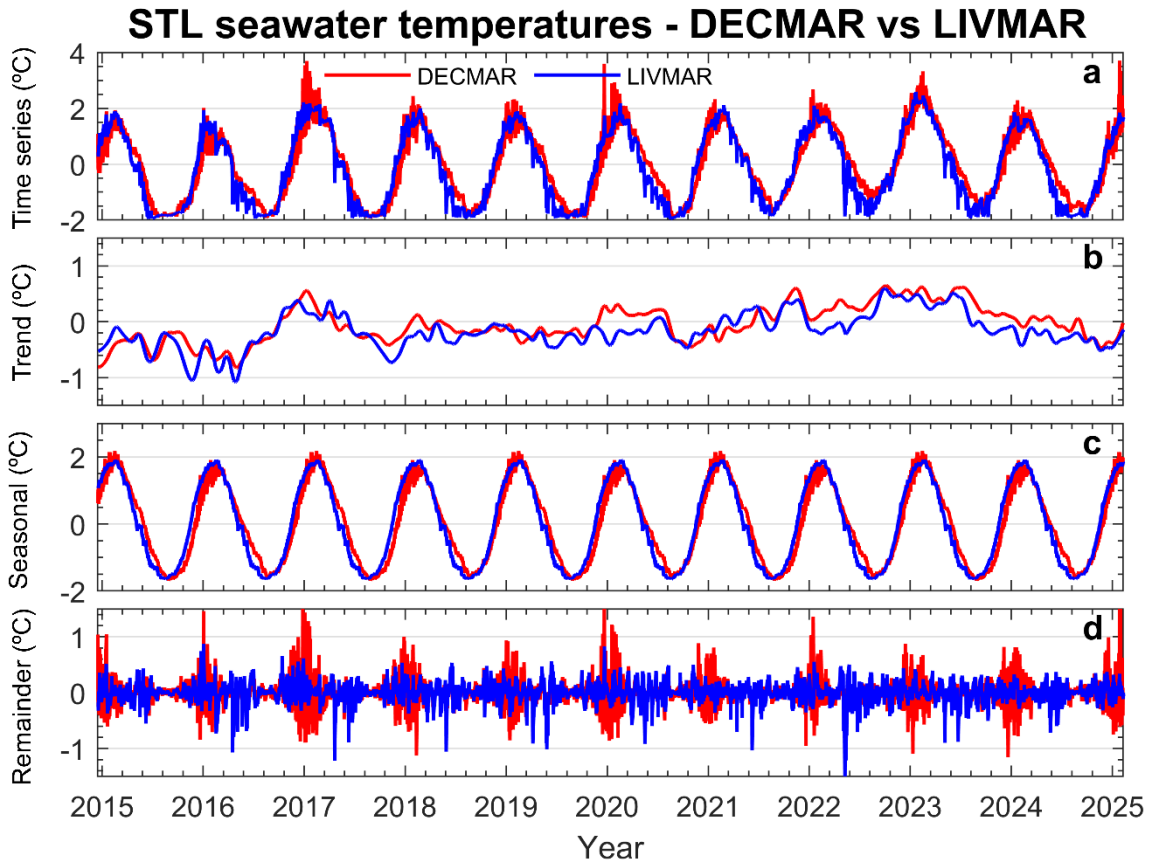


Figure 6.10 STL decomposition to DECMAR (red) and LIVMAR (blue) stations. **a** Raw series of seawater temperatures. **b** Trend of the series. **c** Seasonal component of the records. **d** Remainder of the series.

In terms of similarity, the DECMAR and LIVMAR series exhibited an RMSE of 0.4 °C and an *r*-value of 0.95, indicating a strong correlation. Similarly, the GdC and JCI meteorological series yielded an RMSE of 1.69 °C and an r-value of 0.88, also demonstrating a high degree of similarity.

To assess long-term trends, linear regressions were applied to determine the temperature increase across different seasons over the 10-year period. The results indicate a rise of 0.42 °C in DECMAR, 0.28 °C in LIVMAR, 1.18 °C in JCI, and 0.77 °C in GdC.

6.6 Discussion

The data collected from 2011 to 2025 at the LIVMAR (Livingston Island) and DECMAR (Deception Island) stations provide a detailed insight into the variations in water temperatures across both islands. The observed differences between the stations highlight the impact of local factors, such as volcanic activity on Deception Island, and its influence on regional behaviour. During 2012, Deception Island exhibited notable thermal anomalies

attributable to the advection of water heated by submarine magma, consistent with increased volcanic activity (Berrocoso et al., 2018). This phenomenon demonstrates how local geophysical processes can significantly affect the surrounding seawater temperatures.

Analysis of the 2014/2025 period reveals a pronounced seasonality, with temperature peaks during the austral summer and troughs in the winter, aligned with findings from other studies (Clarke et al., 2008; Lenn et al., 2003; Meredith et al., 2008). Maximum temperatures were consistently recorded in the austral summers, with DECMAR exhibiting higher peaks (up to 3.69 °C) compared to LIVMAR (2.59 °C), this disparity can be linked to the volcanic activity on Deception Island, which adds heat to the surrounding seawater (Berrocoso et al., 2018; Moreno-Vacas & Almendros, 2021). In addition, in 2016 a sudden increase in temperature is observed in both stations (**Figure 6.5c**) due to the strong tectonic activity located between Livingston and Deception Islands (Almendros et al., 2018; Moreno-Vacas & Almendros, 2021), reaches its peak at the beginning of 2017 and decreases throughout that same year.

Also, during the austral summer 2019/2020 (**Figure 6.5f**), an increase in Deception Island water temperatures is seen, and also a small rise in Livingston Island, this could be related to regional changes due to volcanic activity recorded at the Orca submarine volcano in August 2020 (Almendros et al., 2020; Cesca et al., 2022; Rosado et al., 2023). This anomalous warming coincided with the intense seismic activity centred around the Orca submarine volcano, which began in August 2020 and lasted for about one year. The sequence comprised more than 80 000 earthquakes, mostly located northeast of the volcano at depths of up to 10 km, making it one of the largest swarms ever recorded along a spreading ridge (Cesca et al., 2022; Poli et al., 2022; Rosado et al., 2023). The activity was marked by two major phases: in November 2020, with the highest number of events exceeding magnitude 4 and an earthquake of Mw 5.9, and in January 2021, with the largest earthquake of the sequence (Mw 6.9) located further east (Rosado et al., 2023). This crisis was accompanied by ground displacements of up to ~11 cm on King George Island, consistent with magma intrusion as the main driving mechanism (Cesca et al., 2022).

As it is mentioned in the Introduction section, this region is characterised by a complex ocean circulation (see **Figure 6.11a** and **Figure 6.11b**; Sangrà et al., 2011; Sangrà et al., 2017; Veny et al., 2022). Authors such as Johnson, (1998), Juteau, (2005) and Kolbusz et al., (2024) mention that in oceanic ridges and subduction zones, due to geothermal heating, seawater can warm up, allowing it to rise and be replaced by cooler, denser water. Furthermore, Rodrigo et al. (2018) show that there is a hydrothermal anomaly in the vicinity

of the Orca volcano of ~ 0.08 °C, confirming a flow of hydrothermal activity from the crater floor of the seamount. Furthermore, they suggest that there is a hydrothermal influence outside the volcano, perhaps related to subsidiary structures of the Orca seamount, or due to the dispersion of hydrothermal plumes from other volcanic structures of the Bransfield Fault and/or active volcanoes in the region (e.g. Deception Island). This could explain why the water temperature of the BC is warmer than the other surrounding water masses.

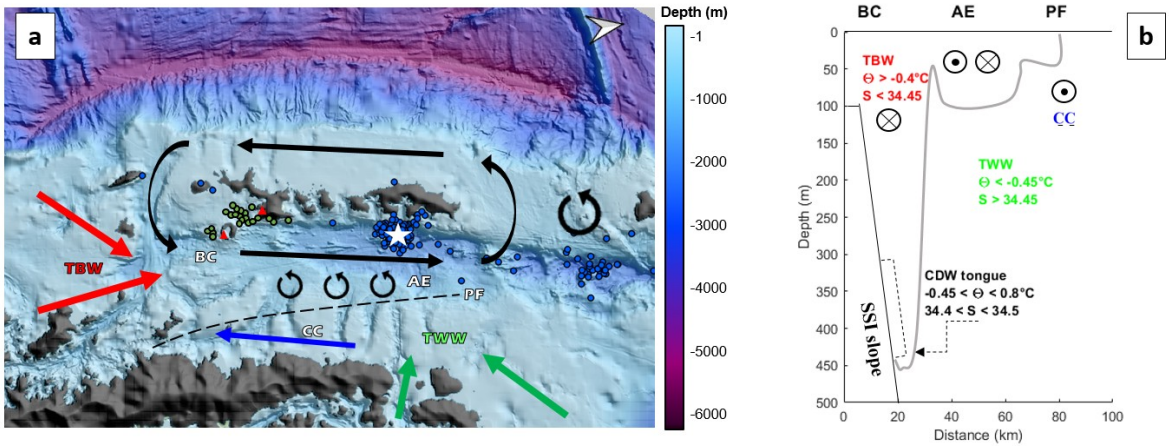


Figure 6.11 a Bathymetric map of the Bransfield Strait and circulation pattern as described in Sangrà et al. 2011, Sangrà et al. 2017 and Veny et al. 2022. The bathymetry used is from the International Bathymetric Chart of the Southern Ocean (IBSCO). Green dots are locations of the seismic swarm of 2015 (adapted from Almendros et al., 2018). The white star is the location of Orca volcano and the blue dots are the locations of the earthquakes higher than 4 Mw from United States Geological Survey (USGS) catalog during this period of geodynamic activity. Red triangles are the locations of the oceanographic stations DECMAR and LIVMAR. **b** Sketch profile of the main components of the currents in the Bransfield Strait adapted from Sangrà et al. 2011 and Veny et al. 2022. The acronyms are: TBW (Transitional Bellingshausen Water, red), BC (Bransfield Current), CC (Antarctic Coastal Current), AE (Anticyclonic Eddy), PF (Polar Front), TWW (Transitional Weddel Water, green), SSI (South Shetland Islands) and CDW tongue (Circumpolar Deep Water).

Considering the circulation around the SSI and the above-mentioned literature on rift and subduction zone waters, it is suggested that the BC has warmer water as the water, as it passes through the entire fracture zone and submarine volcanoes, increases its temperature, and even more so at a time of volcano-tectonic activity. Moreover, focusing on this seismic/geodetic event of the Orca volcano and its impact on the Bransfield region would confirm the rise in sea water temperatures during the winters at the DECMAR and LIVMAR stations between 2021 and 2022, until the volcano-tectonic system decreases its activity. **Figure 6.4** hows that LIVMAR recovers in 2023, but DECMAR does not return to near freezing temperatures until 2024.

Returning to the description of the waters surrounding the islands, also, the reason for the higher noise in the remainder DECMAR signal during the summer could be due to the increased flow of water through the plumbing system of the volcano, which causes an increase in volcanic activity due to differences in the temperature of the ground and water (Caselli et al., 2007; Jiménez Morales et al., 2017). Furthermore, authors such as Anderson et al. (2021) find that the residue is related to weather variations.

During the austral winters, minimum temperatures show significant differences between the two stations. At LIVMAR, temperatures drop earlier and fluctuate more, whereas at DECMAR, periods below -1.8 °C are shorter but more continuous. In areas close to glaciers, the input of meltwater can contribute to a lower salinity in surface waters (Purich & England, 2023; Ribeiro et al., 2021). This lower salinity may lead to increased stratification of the water column, which in turn may reduce mixing with warmer water in deeper layers (Purich et al., 2018; Ribeiro et al., 2021). As a result, surface temperatures in the immediate vicinity of glaciers may reach lower values (Truffer & Motyka, 2016).

The mean value of the distribution of monthly means suggests that although there is not so much difference in January and February maximum temperatures between the stations, temperatures fall earlier at LIVMAR and reach their minimums in August (being lower than at DECMAR). While at DECMAR, the minimums are reached between August and September, and temperatures rise later.

Although the general behaviour is a slight rise in water temperatures, 3 phases of trend behaviour have been identified over the ten years. The first rising phase (2015/2017) is related to the volcano-tectonic activity recorded at Bransfield (Almendros et al., 2018; Moreno-Vacas et al., 2021; see **Figure 6.11a**). The second rise occurred from 2018 to 2023, coinciding with the volcanic activity at Bransfield due to the Orca volcano process (**Figure 6.11a**). And finally, the third phase, lowering, which shows the cessation of the eruption of the Orca seamount volcano. Also, air temperatures have increased over these ten years of study. These results are consistent with those of Turner et al. (2021), whose study in the western Antarctic Peninsula shows an increase in air temperatures as the number of days with maximum temperatures increases and the number of days with minimum temperatures decreases. Furthermore, they state that there is a clear relationship between low air temperatures and the presence of sea ice. Meredith & King, (2005) also state that the evolution of climate is clearly related to trends in temperature and salinity of Antarctic waters. After analysing the trend of the seawater series, it has been found that the Orca volcanic activity in August 2020 has a strong influence on the total trend of these ten years

of study for both stations and that during the last two years the system recovers values from 2018/2019.

The differences in air temperature trends between stations could be attributed to missing data in the series, as GdC lacks records for two warming periods and one cooling period, while JCI is missing data for one cooling period. Additionally, these discrepancies may be influenced by factors identified by Recondo et al. (2022) and Turner et al. (2021) in their study of multiple Antarctic stations in recent years, potentially linked to variables such as station altitude. Recondo et al. (2022) and Oliva et al. (2017) report that atmospheric temperatures in the South Shetland Islands region oscillated between warming and cooling phases during the period from 2006 to 2015. These findings align with the observed pattern in **Figure 6.10b**, where seawater temperatures show three phases with alternating upward and downward trends, although the overall picture is one of rising temperatures.

6.7 Conclusions

The DECMAR and LIVMAR station time series show marked seasonality in water temperature, with peaks in summer and lows in winter. The two stations differ in that DECMAR experiences higher maxima due to thermal anomalies typical of an active volcano, and its minimum temperatures are less stable. In contrast, LIVMAR has lower maximum temperatures, as well as lower and more stable winter temperatures, with its records being influenced by the Johnson Glacier.

Air and seawater temperatures are correlated over the 10 years of the study, both series have a marked seasonality and show a slight increase over the years. However, water temperature is influenced by tectonic and/or volcanic geodynamic activity due to the subduction process of the Phoenix microplate and the spreading rift of the Bransfield Basin. This geodynamic activity causes a rise in the temperature of the surrounding waters, which, carried by the Bransfield Current flowing around the South Shetland Islands, reaches the DECMAR and LIVMAR stations.

In addition, the 2015 and 2020 volcanic events in the Bransfield Strait have been identified in the seawater temperature series as always having a higher impact on Deception Island than on Livingston Island. Two different geodynamic processes have been recorded between 2015 and 2025: between 2015/2017 there was a volcano/tectonic swarm between Livingston and Deception Islands; and a second geodynamic process in 2020/2024 around the area of the Orca seamount in the vicinity of King George Island.

In summary, the analysis of water temperature behaviour highlights both regional climatic influences and the key role of local factors, such as volcano-tectonic activity and freshwater inputs, in shaping thermal patterns. While similarities between the two stations suggest general climatic factors, differences in magnitude, oscillation, and seasonal dynamics underscore the complexity introduced by localised processes. The observed reduction in freezing temperature records, alongside trend changes in maximum and minimum temperatures, reflect the environmental changes occurring in the region. These results highlight the need for continued monitoring to better understand the interaction between climate change and geological activity in polar systems. Ultimately, this work contributes to a broader understanding of polar thermal dynamics, with implications for both climate and geophysical research.

6.8 Connecting text

While long-term temperature records highlight the influence of oceanographic and atmospheric processes on sea level, short-term extreme events can also produce marked anomalies. Chapter 7 addresses this aspect by examining meteotsunamis triggered by the eruption of the HTHH volcano and recorded at Livingston and Deception Islands. The analysis demonstrates how remote explosive events can induce atmospheric pressure waves capable of propagating over global scales and leaving identifiable perturbations in Antarctic sea level observations.

CHAPTER 7

Meteotsunamis triggered by the Hunga Tonga-Hunga Ha'apai eruption in Livingston and Deception Islands, Antarctica. Aliasing, generation place and importance of the water body geometry in determining their amplitude and time-frequency behaviour

The eruption of the Hunga Tonga-Hunga Ha'apai volcano on 15 January 2022 triggered acoustic-gravity (Lamb) waves and meteotsunamis recorded all around the world oceans. These meteotsunamis are analysed on the basis of two tide gauges records in Antarctica along with the atmospheric perturbation, which was obtained by using the atmospheric pressure records from nearby meteorological stations. The instruments are located on Deception and Livingston Islands (sea level and atmospheric pressure sensors). Three meteorological stations and three tide gauge stations along the Pacific Ocean were also used. The atmospheric leading front arrived at the meteorological stations ~ 4 hours before the meteotsunami was recorded by the tide gauges. The passing of two atmospheric acoustic-gravity waves were clearly identified, one propagating eastwards and the other westwards. The meteotsunamis arriving at the study area showed amplitudes of up to 20 cm (Livingston Island) and 5 cm (Deception Island). A time-frequency analysis based on wavelet decomposition and the numerical computation of the meteotsunami refraction while approaching the stations revealed that the meteotsunami oscillations show quite different frequency content between the two stations. This may be explained in terms of the different amplification factors experienced by the meteotsunami while it interacts with the different geomorphological configurations of the corresponding water bodies. The records also evidence a marked difference in the meteotsunami arrival time at the two stations which may be explained by the refraction effects on the meteotsunami fronts while they are approaching the two stations.

Luengo-S, O., Bruno, M., Gómez-Enri, J., & Berrocoso, M. (2025). Meteotsunamis triggered by the Hunga Tonga-Hunga Ha'apai eruption in Livingston and Deception Islands, Antarctica: aliasing, generation place and importance of the water body geometry in determining their amplitude and time– frequency behaviour. Bulletin Of Volcanology, 87(6). https://doi.org/10.1007/s00445-025-01831-2

7.1 Statement of the chapter

The main aim of this work is to analyse the effects of the meteotsunami triggered by the HTHH volcano eruption at sea level and the atmospheric pressure time series recorded on Deception and Livingston Islands, located in the South Shetland Islands (Antarctica). The research is focused on the differences in the arrival time of the atmospheric and sea level perturbations and the different amplitude of the meteotsunami observed at the sea level stations. Wavelet analysis was applied to the time series in order to further study the nature of the different sea level disturbances, which were observed in the in-situ records. Based on the available literature, with exception of the data reported by Stewart et al. (2023) in the Ross Ice Shelf (82º28'13.59"S 152º17'29.91"W), the effect of the HTHH meteotsunami in Antarctica has not previously been analysed due to the lack of accurate in-situ data. A better insight into such events may be of interest to the scientific community as it can help to improve the knowledge of the meteotsunami dynamics generated by volcanic eruption.

7.2 Study area

A detailed description of the South Shetland Islands and the Bransfield Strait is provided in Section 3.1. The expanded study area considered in this chapter, including the Hunga Tonga–Hunga Ha'apai eruption and its transoceanic influence, is described in Section 3.2, where the locations of the oceanographic and meteorological stations used in this study are also shown (**Figure 3.2**).

7.3 Data

This study is based on two main types of data: sea level and atmospheric pressure records. The sea level records were obtained from the LIVMAR and DECMAR stations, sampled at 10-minute intervals, as well as from the NOAA Pacific stations located at Nawiliwili (Kauai), Old Harbor (Alaska) and La Jolla (California). More detailed information is provided in Section 4.1.1. The time period of analysis spanned 48 hours from 15/01/2022 (00:00 UTC) to 16/01/2022 (23:50 UTC). A search for outliers was carried out using the 3 - sigma criterion (Dinardo et al., 2018; Meloni et al., 2019). In addition, a three-month time series from LIVMAR and DECMAR prior to the meteotsunami event was used for a more detailed assessment.

The atmospheric pressure records were obtained from two meteorological stations operated by AEMET (JCI and GdC), as well as the three meteorological stations of the Chilean

Meteorological Directorate (Easter Island, Juan Fernández Island and Antofagasta). Further details are provided in Section 4.1.2.2. The time period of analysis spanned 48 hours from 15/01/2022 (00:00 UTC) to 16/01/2022 (23:50 UTC).

7.4 Methodology

General procedures are provided in Chapter 4. This chapter focuses exclusively on the specific methods used for the analysis of the meteotsunami event.

7.4.1 Wavelet analysis: Maximum overlap Discrete Wavelet Transform and Continuous Wavelet Transform

The wavelet analysis has become the classic technique for analysing non-stationary time series containing sudden and transient signals such as those characteristic of meteotsunamis or acoustic-gravity waves in the atmosphere (Liner, 2010). In this context, it has been used for two main purposes: first, to isolate the high frequency signals characterising the acoustic-gravity waves in the atmospheric pressure records and the meteotsunamis in the sea level records; and second, to analyse the changes in the frequency content of the acoustic-gravity waves and meteotsunamis arriving at the recording stations.

To isolate the high frequency signal, the Signal Multiresolution Analyzer app based on the Maximum Overlap Discrete Wavelet Transform (MODWT) was used (Percival and Walden 2000); while to analyse the changes in the frequency content, the Wavelet Time-Frequency Analyser app is used, based on the Continuous Wavelet Transform (CWT). Both applications are available in the Matlab library.

The Discrete Wavelet Transform (DWT), used in the MODWT, decomposes the input signal into approximation and detail coefficients. The input signal passes through a high-pass filter and a low-pass filter and is then down-sampled by factor 2. From the options available in the app, the option called ‘Morse’ was chosen as the mother wavelet. In addition, there was no appreciable change in the resulting signal when using the other two options offered in the app. The output of the low-pass filter is the approximated signal while the output of the high-pass filter is the time series known as ‘detail’ or ‘level’. The approximated signal represents the low frequency variability while the higher frequency is contained in the detail coefficients. In addition, the specific frequency composition of each ‘detail’ time series lies in different correlative frequency bands, which are ordered from the highest band-averaged frequency to the lowest. Thus, the first detail contains the highest frequencies and the last,

the lowest frequencies. The isolation of the desired signal is then achieved by summing a carefully selected number of appropriate detail coefficients.

As aforementioned, the time-frequency analysis of the isolated signal will be performed by the use of the CWT with the Time Frequency Analyser app. This analysis will allow to track changes in the frequency content of the analysed time series and also identify the dominant frequencies characterising their time variability.

7.4.2 Assessing the effects of aliasing on the meteotsunami records

Although it is known that a 10-minute sampling interval is not ideal for recording meteotsunami signals, it may still contain very valuable information regarding the meteotsunami phenomena arriving at the stations of this study. As it is known, the maximum frequency that can be detected in a time series that is sampled at certain interval dt, the Nyquist frequency (f_{Ny}), is 1/(2dt). This is justified by the fact that at least three values are required at three consecutive time instants (2dt) to detect a cyclic repetition of the values. In this way, the amplitude of any signal with frequency greater than f_{Ny}, will create an aliased (fake) signal in the frequency range ($0 - f_{Ny}$). The frequency of the aliased signal generated by a not time-resolved signal of frequency f_a may be found using Eq. (7.1):

$$f_a = \left| f - (n+2) f_{Ny} \right| \tag{7. 1}$$

where $n = 0,2,4,6$ ... and $f_{Ny} = 1/2dt$, being *dt* the sampling interval (Godin, 1972).

The possible aliasing affecting the records is investigated. To do this, wavelet spectra, computed using the continuous wavelet transform (CWT) methodology, from the three different sea level gauges (Nawiliwili, Old Harbor and La Jolla) recorded at a 1-minute rate have been compared with those that results from the subsample of the original series at 10-minute intervals.

The results have been varied, with frequencies expressed in cycles per hour (cph) to provide a clear and comprehensible measure of how often the given variable fluctuates within one hour. For Old Harbor station (**Figure 7.1a** and **Figure 7.1d**) the wavelet scalogram of the 1-minute sampled records locates the amplitude peaks in the frequency range [0.5 - 2.5] cph, between hours 10 and 30, which is in good agreement with the frequency range where the scalogram of the 10-minute sampled records locate their peaks during the same time lapse. It is worth noting in this scalogram, the amplitude peak close to the hour 40 around the frequency 2.0 cph, which is greater than the peak found in the scalogram corresponding to

the 1-minute sampled records by the same time. The greater amplitude in the former scalogram may be explained by the superposition of the existing amplitude in the true scalogram plus an additional contribution coming from the aliasing of the peaks located around the frequency of 4 cph in the true scalogram which, as can be checked through Eq. (7.1) (with n = 0), would produce a signal with an aliased frequency of 2 cph.

However, for the other two stations the amplitude peaks of the 1-minute sampled series are located in the frequency range of [1 - 12.5] cph for the two stations, while the spectra of the 10-minute sampled series are in the range [1 - 2.5] cph. This shifting in frequencies is concomitant to the expected aliasing effect arising when the Nyquist frequency, f_{Ny}, of our sampling is lesser than the dominant frequencies of the actual signal.

Attention is now turned to the La Jolla record, as it is an open ocean station unaffected by the natural oscillation periods of any semi-enclosed body. Applying the previous formula to the frequency range where the scalogram of this station locates the highest amplitude (f = 2.5 - 12 cph) yield contribution to the aliased scalogram in the frequency range f_a = 0 - 3 cph. The greatest amplitude peaks appearing in the true scalogram lie in the band centred at 10 cph (**Figure 7.1c**) and they could be responsible for the peak of the scalogram centred at 2.25 cph (**Figure 7.1f**). Nevertheless, it must be noted that the true scalogram also shows amplitude peaks around 2.25 cph. Therefore, in terms of the aliased spectrum, the frequency band centred at the aliased frequency of 2.25 cph could receive contribution from the two true frequencies commented above. However, a greater contribution from the band centred at 10 cph is expected because of its greater amplitude peaks. In fact, the peak in the aliased scalogram lying around 2.0 - 2.25 cph shows a very similar amplitude to that shown around 10 cph in the true scalogram. Following the same reasoning, the amplitude peaks appearing within the band centred at 6.75 cph in the true scalogram would give rise to the amplitude peak of the aliased frequency centred at 0.75 cph. It must be also noted that the scalogram shows certain amplitude in true frequencies close to 0.75 cph.

Therefore, it can be concluded that although the true frequency distribution of the meteotsunami signal is not resolved by 10-minute interval sampling, the increase in amplitude detected in the scalogram spectrum allows to detect the arrival of the meteotsunami. Thus capturing approximately, the maximum amplitude exhibited in the true spectrum.

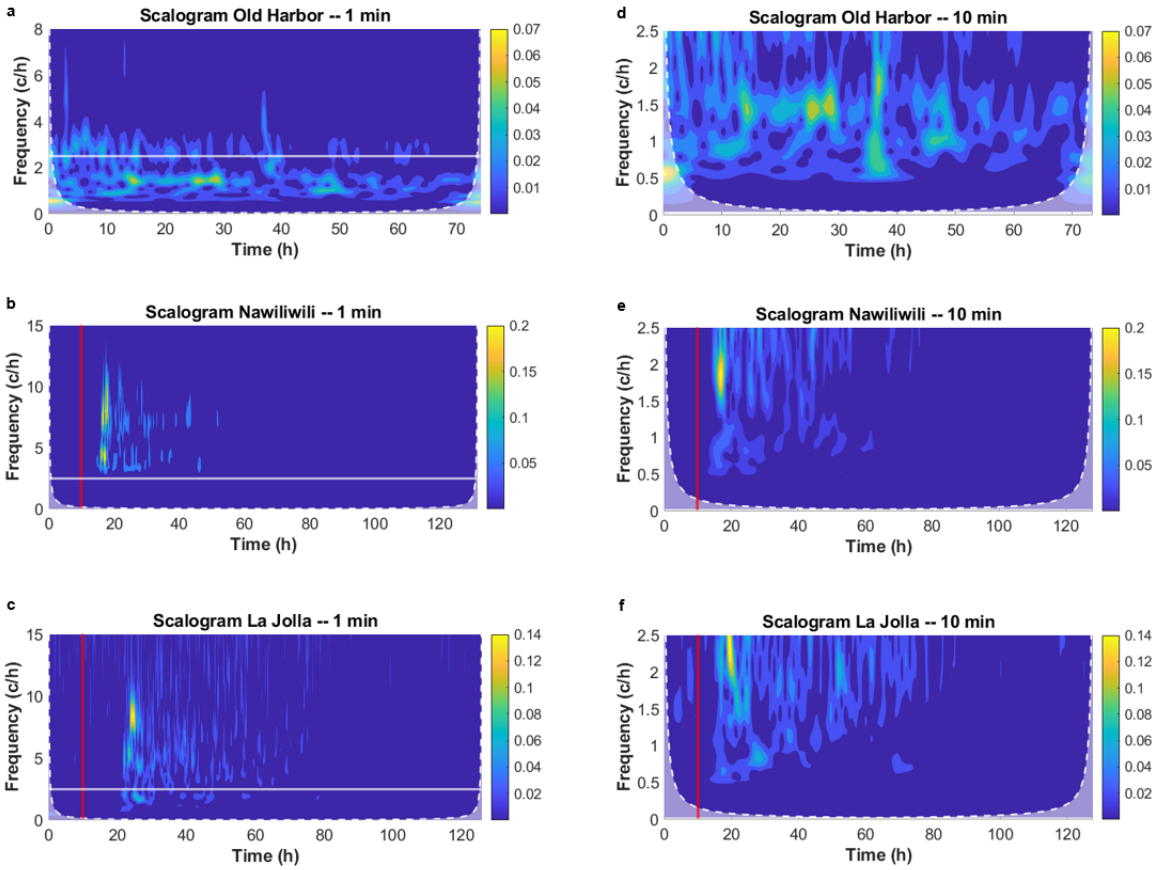


Figure 7.1 a b c Scalograms of the 1-minute record of the Old Harbor (a), Nawiliwili (b) and La Jolla (c) stations. White horizontal lines indicate the maximum frequency of the 10-minute scalograms (~2.5 cph). **d e f** Scalograms of the 10-minute record of the Old Harbor (d), Nawiliwili (e) and La Jolla (f) stations. Records start on 14/01/2022 at 18:10 for Nawiliwili and La Jolla, and on 16/01/2022 at 12:40 for Old Harbor. The red vertical line indicates the time of the eruption of the HTHH volcano (15/01/2022 at 04:10 UTC).

7.4.3 Computation of the amplification factor by using simulations from a 2D hydrodynamic model

The 2D hydrodynamical model described in Bolado-Penagos et al. (2021) was used to compute the amplification factor experienced by the long waves entering the water bodies that housed the pressure sensors. To streamline the process and avoid the extensive time required for model implementation and calibration in real domains, which exceed this manuscript's scope, idealised rather than real domains were used for the water bodies (**Figure 7.2**). This approach involved the numerical integration of the long-wave hydrodynamic equations within these simplified spatial domains of the semi-enclosed water bodies, as shown in **Figure 7.2**. Note that for Deception Island, the idealisation of the semi enclosed water body has been simplified by using rectilinear boundaries. While this simplification creates non-realistic additional areas in the corners of the idealised domain, it

is very helpful to facilitate the numerical stability of the model. In spite of this fact, the idealised geometry fits quite well the main volumetric features of the actual water body.

Using the model proposed by Bolado-Penagos et al. (2021) provides a more accurate alternative to relying on the approximate analytical formulas currently available. Further technical details of the model may be found in Bolado-Penagos et al. (2021). This model is forced at the open boundaries of the two water bodies (see **Figure 7.2**) by an incident long wave with an amplitude of 0.1 m for different frequencies (0.25 to 20 cph). After each simulation, the amplification factor is computed for each long-wave as the quotient A_1/A_0, where A_1 is the amplitude within the water body, at the nodes of the numerical model mesh closest to the measurement stations, and A_0 (always equal to 0.1 m) is the amplitude of the incident wave at the open boundary. This methodology is quite similar to that used in Marcos et al. (2009) and Kim & Woo (2021). It is worth noting that no other forcing apart from that introduced by the long waves has been considered.

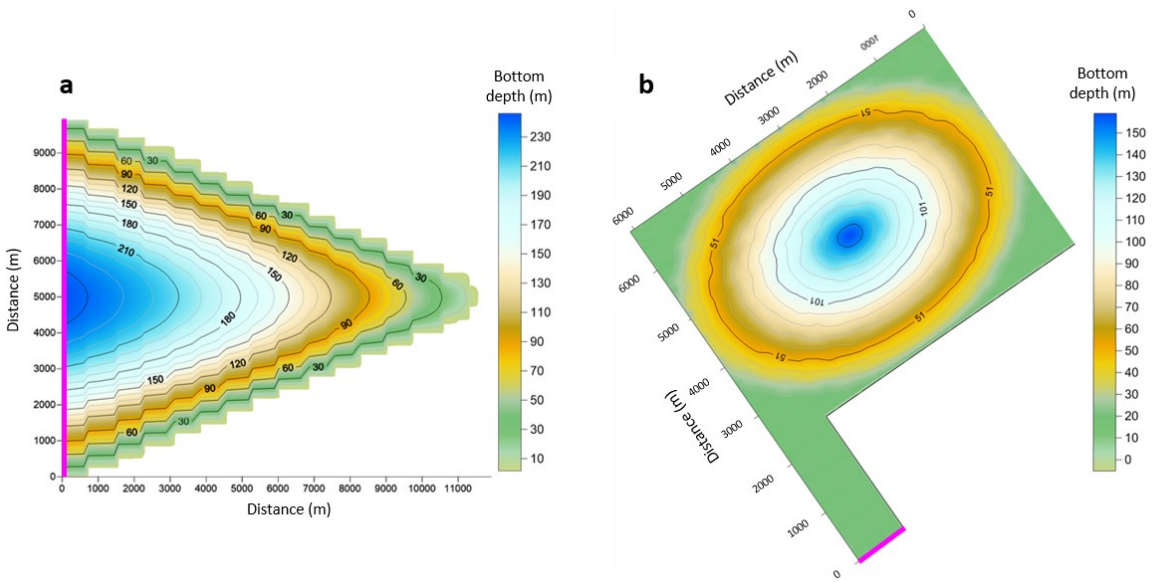


Figure 7.2 Idealised bathymetries used for computing the amplification factors of long waves as a function of the incident long-wave frequency (Figure 7.8). **a** For the water body housing LIVMAR station (Livingston Island). **b** For the water body housing DECMAR station (Deception Island). The open boundaries are identified by a pink line.

7.4.4 Wave refraction maps

To improve the understanding of the transformation that is experienced in amplitude and propagation direction of the incoming meteotsunami arriving at LIVMAR and DECMAR stations, the calculation of the refraction map for a given meteotsunami entering the area was

performed. In order to do this, the method explained in Koutitas (1988) was followed. The computation starts by specifying the position of a long-wave front of 1-m amplitude on the western (left hand) side of the spatial domain heading east. Then the front evolution is tracked every 5 seconds, by following the change of position of initially equispaced points over the front while the front is moving at the long-wave speed, which can be quantified using Eq. (7.2):

$$c = \sqrt{gh} \tag{7.2}$$

where g is the gravitational acceleration and h the water depth (Kasahara, 1977). Hence, for water depths of ~ 4000 m, the propagation speed is ~ 200 m/s. Additionally, by applying the energy conservation between front orthogonals, wave height changes along the fronts are also computed.

7.5 Results and discussion

This section analyses the atmospheric pressure and sea level signals registered at recording stations in Antarctica and the Pacific Ocean after the HTHH eruption, using wavelet-based analysis. Furthermore, the likely location point of the meteotsunami origin is discussed, as well as the differences between the meteotsunami records of the two sea level stations.

7.5.1 Observations of atmospheric pressure and sea level perturbations at Livingston and Deception Islands after the HTHH eruption

Figure 7.3 shows the time series (from 15/01/2022 to 19/01/2022) of atmospheric pressure from the JCI meteorological station (**Figure 7.3a**), GdC meteorological station (**Figure 7.3b**) and the bottom pressure from the tide gauges: LIVMAR (**Figure 7.3c**) and DECMAR (**Figure 7.3d**). The vertical red line indicates the time of the eruption. A small anomaly in the atmospheric pressure can be observed a few hours after the eruption that might indicate the arrival of the atmospheric perturbation in the study area. The LIVMAR tide gauge records a slight bottom-pressure undulation that could suggest the arrival of the meteotsunami. This is not the case of the DECMAR station where no clear evidence of bottom-pressure anomalies is observed. Tidal oscillation is clearly seen in the sea level records.

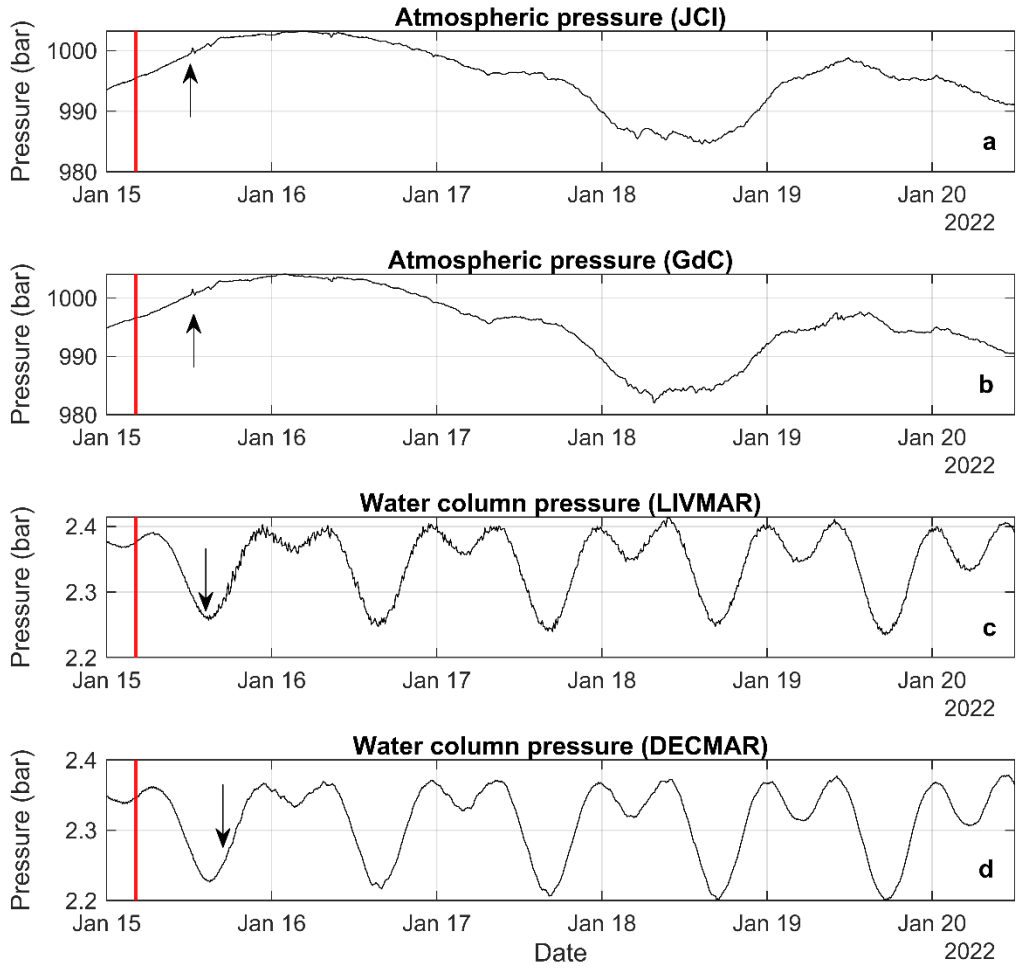


Figure 7.3 a Time series of atmospheric pressure from JCI station. **b** Time series of atmospheric pressure from GdC station. **c** Bottom pressure from LIVMAR station. **d** Bottom pressure from DECMAR station. The vertical red line indicates the time of the eruption of the HTHH volcano (15/01/2022 at 04:10 UTC). The black arrows mark the points at which anomalies in the records become visually noticeable. The record of JCI is analysed with the one of LIVMAR and the GdC record with the DECMAR record due to the proximity between stations.

The lower frequency components of the time series in **Figure 7.3** make a detailed analysis of the effects of the atmospheric / sea level perturbations in our study area difficult. For this reason, it was necessary to filter out the signals of lower frequencies not related to the perturbations triggered by the HTHH eruption. This filtering procedure is achieved by applying the MODWT to the original records. This procedure is applied on bottom-pressure records before they are converted to sea level following Eqs. (4.1) and (4.2). **Figure 7.4** shows the resulting filtered signals, for January 15 and 16 2022, of atmospheric pressure (JCI: **Figure 7.4a**; GdC: **Figure 7.4b**) and sea level (LIVMAR: **Figure 7.4c**; DECMAR: **Figure 7.4d**). The arrival of the atmospheric-pressure perturbation created by the volcano explosion is seen followed by the sea level oscillations associated with the meteotsunami,

now more visible, which show significantly greater amplitudes in LIVMAR when compared with DECMAR. In order to establish the arrival time of the first sea level disturbance, the 1 - standard deviation (1-σ) criterion was used (Shaheen et al., 2024; Soltanpour et al., 2018; Trisirisatayawong et al., 2011). This is not necessary in the atmospheric pressure signal as the perturbation is clearly observed, the classical N shape in the atmospheric pressure record associated with the Lamb wave is easily recognized in the two meteorological stations (Heinrich et al., 2023). The first sea level oscillation outside the $\pm(1\sigma)$ envelope is the first perturbation due to the arrival of the meteotsunami. **Table 7.1** summarises the arrival times of both atmospheric and sea level perturbations at the four stations. Some other atmospheric pressure perturbations were observed three days after the HTHH eruption, but their analysis is out of the scope of this paper.

The first atmospheric perturbation has an amplitude of about 1 mbar, with a sea level maximum amplitude of 20 / 5 cm for LIVMAR / DECMAR, respectively. The arrival time of the atmospheric pressure perturbation is observed before the sea level records (**Table 7.1**). The first signal of the meteotsunami arrived 3.83 / 4.67 h (LIVMAR / DECMAR) after the arrival of the acoustic-gravity wave. This clearly indicates that the primary meteotsunami corresponding to the sea level response to the atmospheric anomaly (inverse barometer response) was not detected at our station. This had previously been observed by Heidarzadeh et al. (2022) and Ramírez-Herrera et al. (2022) in locations such as Norkfolk Island (Australia) and Puerto Chiapas (Mexico). Thus, the sea level oscillations recorded at DECMAR and LIVMAR some hours after are not related to local forcing but to remote forcing in a place far from the recording stations. At some locations, the primary atmospheric pressure and sea level perturbations were observed simultaneously (Kataoka et al., 2022; Omira et al., 2022).

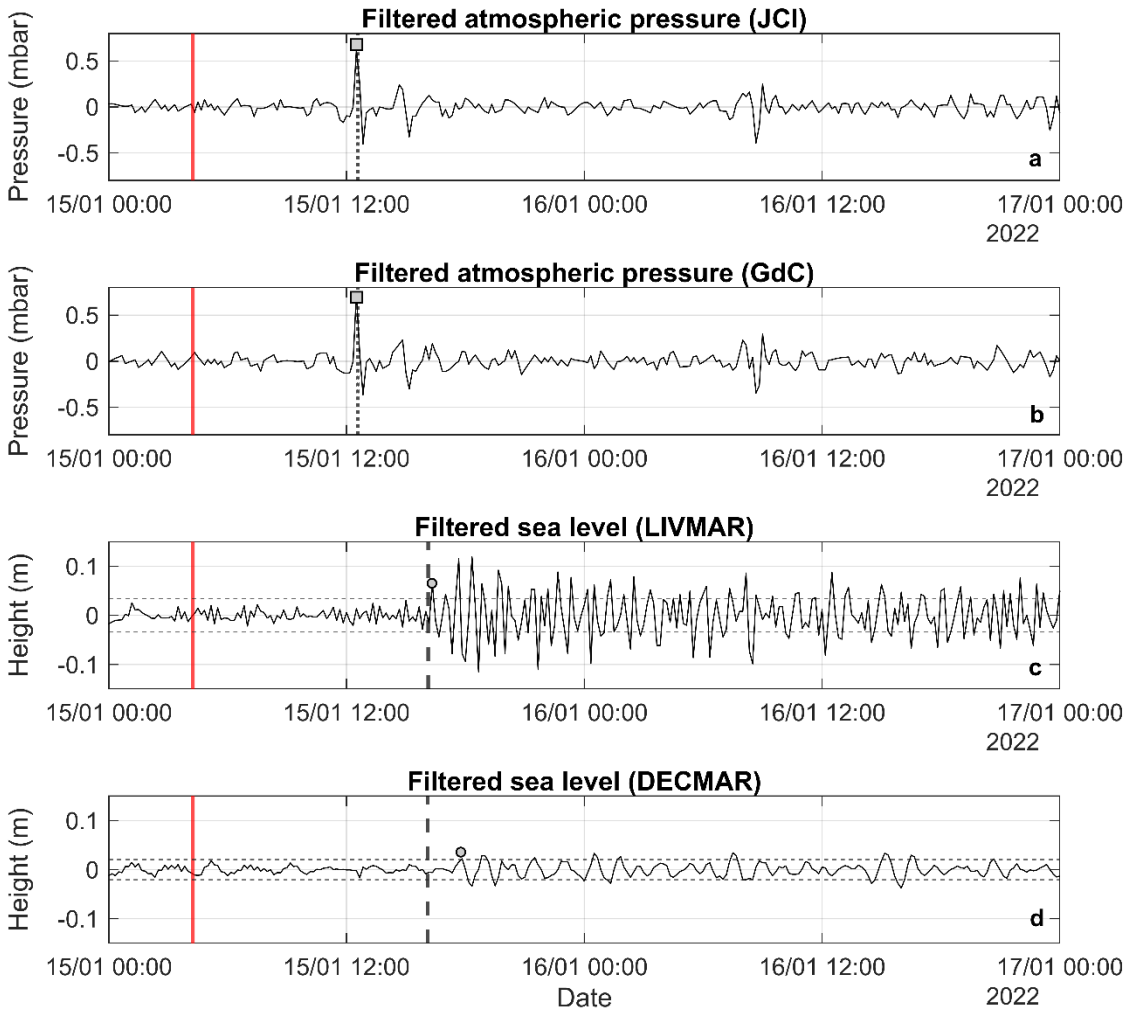


Figure 7.4 Wavelet filtered records for January 15 and 16 2022. **a** Filtered atmospheric pressure at JCI station. **b** Filtered atmospheric pressure at GdC station. **c** Filtered atmospheric pressure at LIVMAR station. **d** Filtered atmospheric pressure at DECMAR station. Dashed horizontal lines in 7.4c and 7.4d give the (1-σ) interval. The vertical red line in all the plots indicates the time of the eruption of the Hunga Tonga-Hunga Ha'apai volcano (15/01/2022 - 4:10 UTC). The grey squares indicate the first record associated with the atmospheric perturbation (Figures 7.4a and 7.4b) and grey dots indicate the first record associated with the meteotsunami (Figures 7.4c and 7.4d). The dotted black line indicates the theoretical arrival time for atmospheric pressure waves if the mean propagation velocity is as calculated from all stations used in this article (see **Table 7.1**). Dashed black line indicates the theoretical arrival at the tide gauges if it were a conventional tsunami originating in the trench near HTHH. The record of JCI is analysed with the one of LIVMAR and the GdC record with the DECMAR record due to the proximity between stations.

The analysis of the atmospheric pressure disturbance using additional meteorological stations might help to achieve a better understanding of its propagation behaviour. The wavelet filtered time series are shown in **Figure 7.5** for the Chilean stations (Easter Island, Juan Fernandez and Antofagasta) along with the Spanish ones (JCI and GdC). The atmospheric disturbance arrived at the stations twice: on 15 January and on 16 January (very much attenuated). These different arrivals are related to the acoustic-gravity wave traveling

either way around the globe (SE/NW) from the eruption point. One distinctive characteristic of the second atmospheric wave was that it was first sensed at the stations located further east (Antofagasta and Juan Fernandez). This indicates that the second acoustic gravity wave was initially directed toward the northwest (NW) and later returned from the southeast (SE) after travelling around the Earth.

The amplitude of the eastward propagating wave ranges between 2 mbar (Easter Island and Antofagasta) and 1 mbar (JCI, GdC and Juan Fernandez), being < 1 mbar in all the stations recording the westward propagating wave. The magnitude of the signal is weaker due to the loss of energy as the perturbation propagates a longer distance throughout the atmosphere (Kataoka et al., 2022; Nishida et al., 2014). The arrival time of the perturbation to the meteorological stations and their distances to HTHH are given in **Table 7.1**. There is a direct correlation between the time of arrival at the stations and their distances to the HTHH volcano except for the Antofagasta station, as it is found behind the Morro Moreno National Park (Chile), which reaches a maximum altitude of 1148 m.a.s.l. According to other sources, atmospheric pressure waves may be amplified as they pass through steep terrain (Ren et al., 2023; Vilibić, 2008). The atmospheric pressure disturbances at JCI and GdC associated with the generated wave front are recorded 8.3 h (eastward) and 27.8 h (westward) after the eruption. The relationship between the distances and arrival times of the atmospheric pressure perturbations agrees with those recorded by Stewart et al. (2023) in the Ross Ice Shelf.

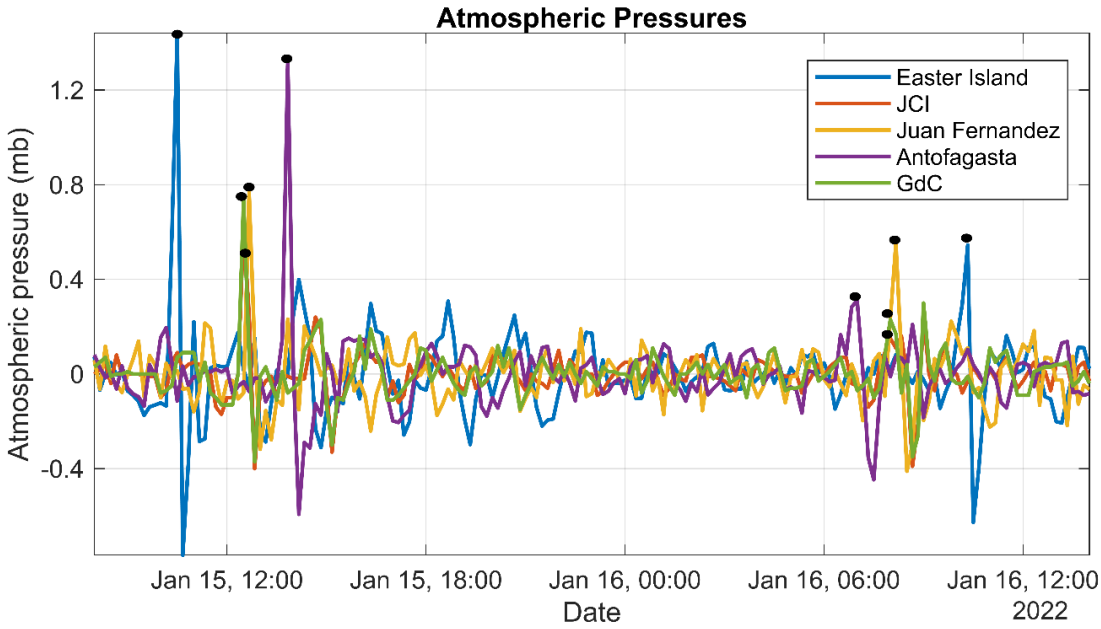


Figure 7.5 Atmospheric pressure filtered data (wavelet-based) recorded at the meteorological stations: Easter Island (blue), JCI (orange), Juan Fernandez Island (yellow), Antofagasta (purple) and GdC (green). Black dots indicate the first (eastward) and second pulse (westward) of the atmospheric perturbation.

On average, the propagation speed of the acoustic-gravity wave leading front is about 302 m/s, as previously noted by Gusman et al. (2022), Kataoka et al. (2022) and Ramírez-Herrera et al. (2022). Regarding the arrival time of the sea level perturbation, it is observed that it arrives at DECMAR after LIVMAR. This aspect will be discussed further.

Table 7.1 Arrival time of the atmospheric Lamb wave and meteotsunamis at the meteorological and tide gauge stations (eastward / westward propagation), shortest distance between HTHH volcano and recording stations and propagation speed of the atmospheric pressure leading front (eastward).

Station	Arrival time (eastward propagation: 15/01/2022) (UTC)	Shortest distance between the station and Tonga (km)	Propagation speed (m/s) (eastward propagation)	Arrival time (westward propagation: 16/02/2022) (UTC)
Atmospheric Lamb wave				
Easter Island	10:30	6683.07	293.11	10:20
Juan Carlos I	12:30	9191.61	306.38	9:00
Gabriel de Castilla	12:30	9162.69	305.42	9:00
Juan Fernández Island	12:40	9350.73	305.58	8:10
Antofagasta	13:50	10538.18	302.82	7:00
Meteotsunami				
LIVMAR	16:20	9192.49	209.82	-
DECMAR	17:10	9171.9	195.98	-

7.5.2 Origin of the meteotsunamis recorded at Livingston and Deception Islands

As mentioned, the atmospheric pressure disturbance originated by a huge volcano eruption generates an oceanic sea level perturbation by the so-called inverse barometer response (Kataoka et al., 2022; Omira et al., 2022; Tonegawa & Fukao, 2022; Vilibić, 2008; Yamada et al., 2022). This ocean response is produced all along the propagation of the atmospheric pressure leading front. The amplitude of the sea level barometric response is related to the magnitude of the atmospheric disturbance and it moves at its same speed (~ 310 m/s). This meteotsunami component is constantly generated whereby the atmospheric acoustic-gravity

wave is passing and henceforth it would reach the recording station at the same time as the atmospheric wave. As commented in the previous section, the signal of this meteotsunami was not detected in our records.

Taking into account that the location of DECMAR station does not receive directly the meteotsunami front LIVMAR will be used for propagation speed computation. Considering that the shortest distance between LIVMAR station and the HTHH volcano (9192.49 km) and the time difference between the volcano explosion and the meteotsunami arrival time at LIVMAR (12.17 h), if it is accepted that the recorded meteotsunami was generated very close to the explosion site, an average propagation speed of 210 m/s is obtained.

Moreover, the mean propagation speed of long waves, computed through the Eq. (7.2) taking h as the mean depth along the line (shown in **Figure 7.6a**) separating the two points (h = 433.63 m) yields a value of 208.55 m/s which agrees quite well with the average propagation speed of 210 m/s. This result indicates that the meteotsunami arriving at the stations was triggered very close to the volcanic explosion. Considering the depth of the trench (9000 m) located a few kilometres eastward from the volcano allows for a meteotsunami propagation speed very close to that of the acoustic-gravity waves in the atmosphere, making the occurrence of Proudman resonance possible here, and in turn the meteotsunami amplification. Therefore, this area is identified as the most plausible for the meteotsunami generation. Omira et al. (2022) have also highlighted the possible occurrence of Proudman resonance in this region due to the same meteotsunamis.

It is worth noting that even when the Proudman resonance conditions are not met, the meteotsunami could also experience amplification by the non-linear energy transfer to the initially created meteotsunami from the less energetic secondary acoustic-gravity waves (within the envelope of the wave group), moving behind the leading front (Harkrider & Press, 1967; Omira et al., 2022). After the described amplification processes, the meteotsunami is decoupled from the atmospheric disturbance and left behind the latter, while it continues moving at the long wave speed. From now on, the meteotsunami will undergo a progressive loss of amplitude. However, when it reaches the continental slope and shelf, it could experience an additional amplification caused by the bottom depth reduction encountered while approaching these areas. Finally, once the meteotsunami enters a semi-enclosed water body where the recording stations are located, it can experience additional amplification if the main frequencies of the meteotsunami-induced oscillations match with the natural oscillation frequencies of that water body. This kind of amplification

will be very relevant to understand the frequency content of the recorded meteotsunami signal as will be seen in the next section.

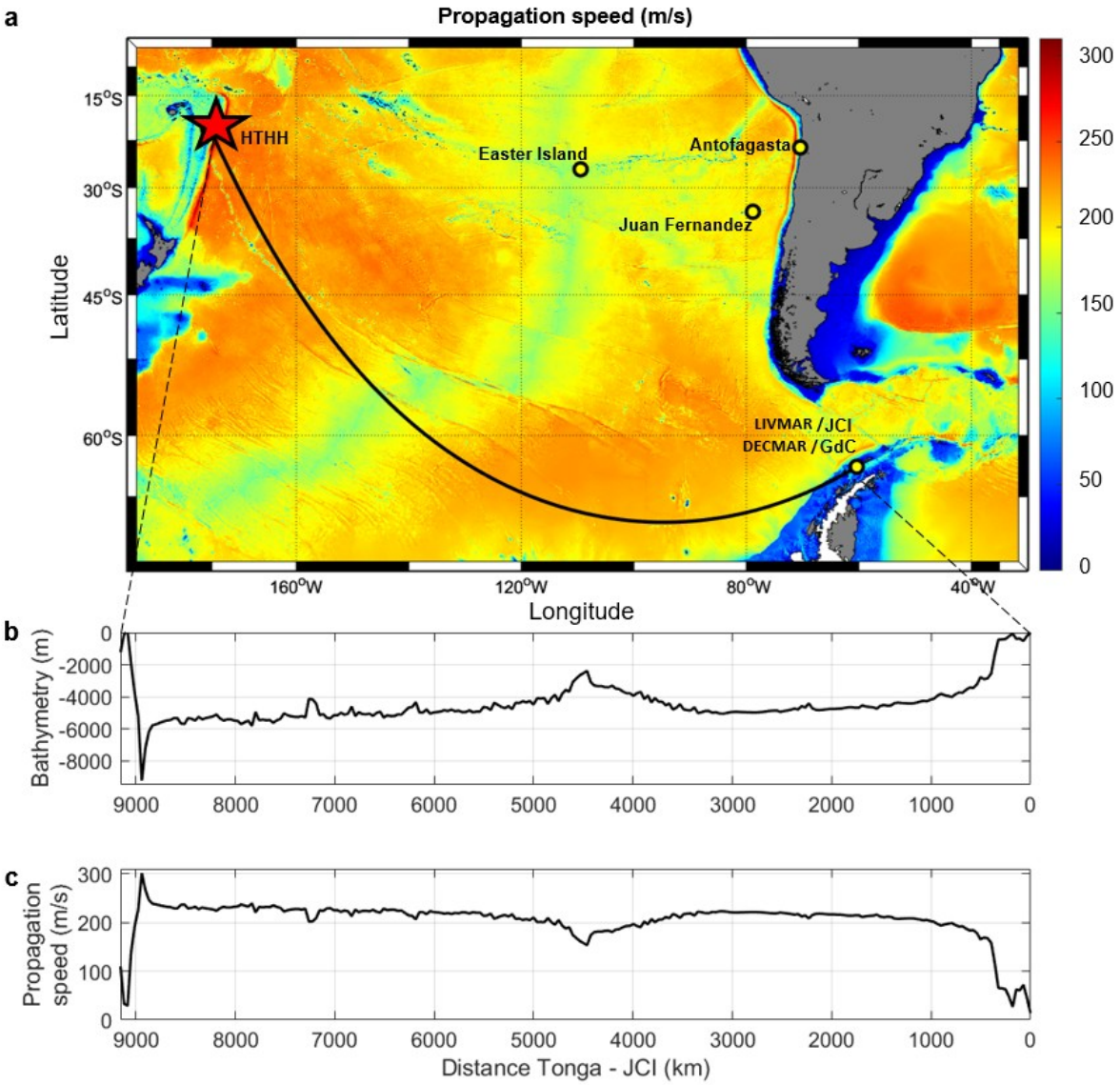


Figure 7.6 a Ocean wave propagation phase speed map (Mercator projection), showing HTHH volcano (red star), tide gauge and meteorological stations (yellow dots). Black line represents the shortest distance from the HTHH volcano to the JCI station taking into account the curvature of the Earth. **b** Bathymetry profile between HTHH and JCI (black line in Figure 7.6a) for the shortest distance between HTHH volcano and JCI. The mean depth along the line depicting the shortest distance is 4433.63 m. **c** Same as Figure 7.6a for the propagation speed.

7.5.3 Analysis of the frequency content characterising the meteotsunami records in LIVMAR and DECMAR

As described in the data and methods section, a compulsory issue to deal with in the analysis of the frequency content is the effect of the aliasing on the meteotsunami records. It should be noted that all the identified frequencies of our recorded signals (taken at a sample rate of 10 minutes) will not be true frequencies if the actual signal contains frequencies greater than 3 cph (the Nyquist frequency of the records). In that section it was seen (taking the 1-minute sampled record of the meteotsunami in La Jolla station as a reference) that a meteotsunami signal with a frequency of 10 cph (period of 6 minutes) sample at a 10-minute interval, would produce an aliased signal with a frequency of 2.25 cph (26.67 minutes). Assuming that the expected frequency content in our stations is similar to that at La Jolla station and that here the meteotsunami record showed its amplitude peaks in the frequency range (5 - 12 cph), it is expected that the entire meteotsunami signal recorded in the stations will be affected by aliasing, since this frequency range is above the Nyquist frequency of the records. In order to establish a reference background to interpret the changes in the frequency content produced by the meteotsunami arrival, the high frequency signal of sea level records spanning three months prior to the meteotsunami records were analysed at each station. This signal was obtained by the MODWT-based filtering procedure. Later the spectra of the filtered series, containing the meteotsunami signals, will be assessed in the two stations.

7.5.4 Analysis of the three-month record prior to the meteotsunami event

Figure 7.7 shows the wavelet scalogram corresponding to the CWT application on the filtered time series recorded in LIVMAR and DECMAR for a three-month period prior to the meteotsunami records. The LIVMAR scalogram (**Figure 7.7a**) shows the dominant frequency bands where most of the amplitude peaks lie: [2 - 2.5], [1.25 - 1.75] and [0.75 - 1.00] cph. Meanwhile, the DECMAR scalogram (**Figure 7.7b**) shows another dominant band in the frequency range [0.5 - 1] cph and the band [1.25 - 1.75] cph with eventual occurrence of amplitude peaks. The persistence of these peaks suggests that they could be related to the natural oscillation periods of the semi-enclosed bodies where the corresponding records are located.

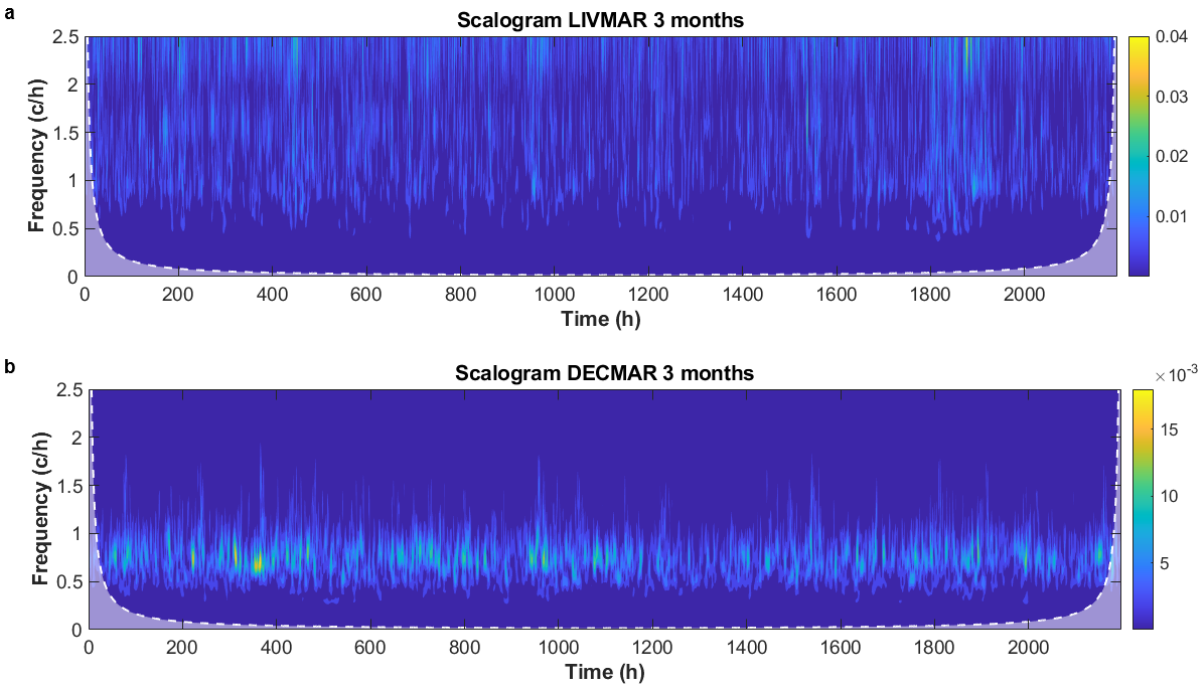


Figure 7.7 a Scalogram of the 10-minute record of LIVMAR station for the 3-month period. **b** Scalogram of the 10-minute record of DECMAR station for the 3-month period. White area is the cone of influence where the edge effects can distort the results.

The amplification factor of long waves in the idealised water bodies are shown in **Figure 7.8**. For the water body of LIVMAR the amplification shows a rather flat maximum centred at the frequency of 4.8 cph which indicates an amplification of roughly 2 times for long-waves with frequencies lying in the frequency interval ranging from 4 to 8.5 cph. This is translated to the aliased frequency interval that ranges from 1 to 2.5 cph. This frequency range is in good agreement with the dominant bands shown by the corresponding scalogram (**Figure 7.7a**). The dominant bands can then be justified by the regular amplification which the incident long waves (with frequencies within the mentioned range) experience.

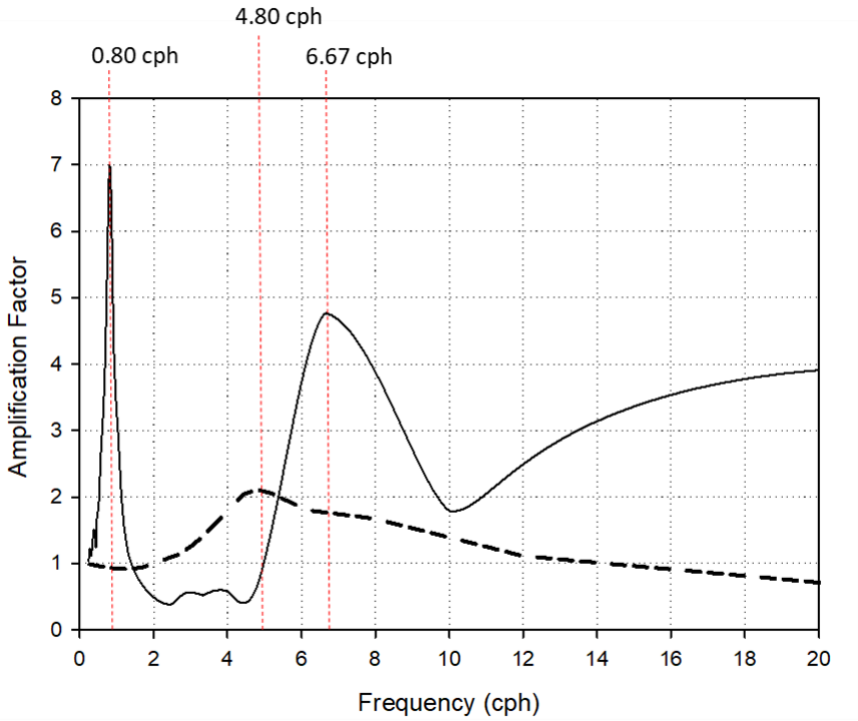


Figure 7.8 Amplification factors as a function of incident long-wave frequency, for the idealised water bodies housing LIVMAR (dotted line) and DECMAR (solid line) tidal gauge stations (shown in **Figure 7.2**).

Regarding the results for DECMAR station, **Figure 7.8** shows that the greatest amplification is reached by the frequency of 0.8 cph (period of 1.25 hours) followed by the frequency of 6.67 cph (period of 8.99 minutes). The first frequency is well resolved by the sampling interval of the records while the second one will be translated to a frequency of 0.67 cph in terms of the aliased signal. Therefore, both signals will be located within a very narrow frequency interval in the aliased spectrum. In the scalogram of **Figure 7.7b** some amplitude peaks are located at frequencies of up to 1.5 cph which could be associated with a true frequency of 7.5 cph. This true frequency shows, according to the function of **Figure 7.8**, an amplification factor as high as 4.5. This fact is supported by the rather flattened peak centred at the frequency of 0.75 cph.

7.5.5 Meteotsunami records at LIVMAR and DECMAR

The scalograms corresponding to the filtered sea level records taken while the meteotsunami was arriving at the stations are shown in **Figure 7.9a** and **Figure 7.9b**. For the LIVMAR scalogram the two most dominant frequency bands are the same ones previously identified in **Figure 7.8**, in the analysis of the three-month long record. It could be then thought that

the meteotsunami arrival at the semi-enclosed body of water housing the station could bring energy in those frequencies that are amplified for the water body geomorphology. Note that during the previous hours no sea level oscillation was recorded at the station, this is the reason why the higher amplitude oscillations are associated with the arrival of the meteotsunami. Recalling the scalogram of the meteotsunami record at La Jolla station (**Figure 7.1c**), if the LIVMAR record had been sampled at a rate of 1 minute, oscillations caused by meteotsunamis could be expected within the frequency bands centred at 2.25, 6.75 and 10 cph which will be translated to the aliased scalogram (corresponding to the 10-minute sampling) at the frequencies 2.25, 0.75 and 2.0 cph respectively. It can be seen that the recorded signal in the frequency bands [2.00 - 2.25] cph and [0.5 - 1] cph is the one expected from the meteotsunami oscillations with true-frequency bands centred at 2.25, 10 and 6.75 cph. However, there is an additional signal in the aliased-frequency band centred at 1.5 cph, which was also recognised in the three-month scalogram. This could be related to a true-frequency of 4.5 cph. Even when a high amplitude in the meteotsunami record of La Jolla is not shown, it could have benefited from the amplification that it would experience according to the amplification function shown in **Figure 7.6**. Finally, with much lesser amplitude, a signal centred in the aliased frequency of 0.75 cph can be recognised, which could correspond to the amplitudes contained in the true-frequency band centred at 0.75 and 6.75 cph, previously identified in the La Jolla station scalogram.

Regarding the meteotsunami record in DECMAR (**Figure 7.9b**), the most remarkable feature is a clear dominant band centred at 0.75 cph which corresponds with a true frequency of 6.75 cph, although, as previously noted, it could be related to a true-frequency of 0.75 cph brought by the meteotsunami. According to the amplification function for the semi-enclosed water body of Deception Island, both frequencies would be amplified and it would justify the dominance of that frequency in the meteotsunami record of DECMAR station. At the same time, other oscillations brought with the meteotsunami, as those with frequencies of 2.25 and 10 cph, are not amplified to the same extent as the former ones. It should be noted that the frequency of 2.25 cph even shows an amplification factor less than 1 (~ 0.5).

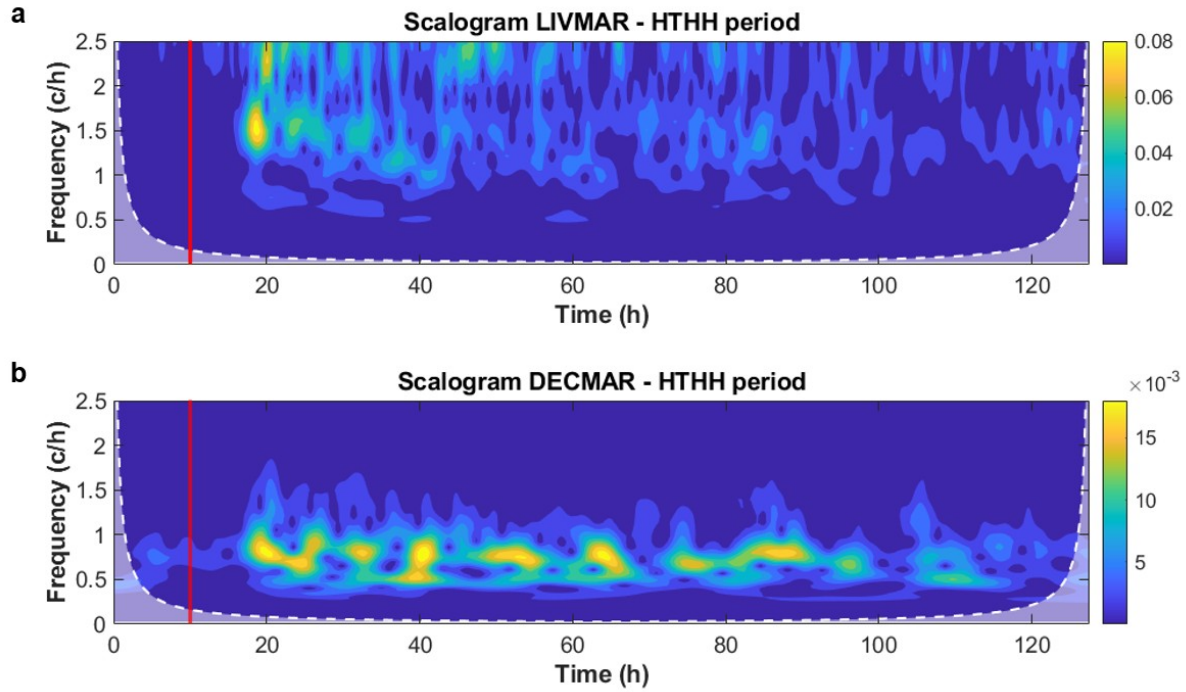


Figure 7.9 a Scalogram of the 10-minute record of LIVMAR station for the selected period of the HTHH eruption. **b** Scalogram of the 10-minute record of DECMAR station for the selected period of the HTHH eruption. Records begin on 14/01/2022 at 23:20 and the red vertical line indicates the time of the eruption of the HTHH volcano (15/01/2022 at 04:10 UTC).

7.5.6 Inferring the differences in meteotsunami arrival time between LIVMAR and DECMAR as deduced from numerically-computed long wave refraction map

The resulting refraction map after following the methodology described in the data and methods section is shown in **Figure 7.10**. The initial orientation of the front on the western side (left hand) of the spatial dominion has been taken from the meteotsunami simulation shown in Omira et al. (2022) (their **Figure 7.3**). As expected, the front first reaches Deception Island wrapping itself along its left side while the wave height increases where the wave touches the coast. The front takes 24 minutes to reach the entrance to the inner water body of Deception Island and 42 minutes to arrive at LIVMAR station. This time difference in arrival time at the two stations contradicts what has been shown in **Figure 7.4**, where the meteotsunami oscillations are recorded 50 minutes earlier at LIVMAR station. In order to explain this discrepancy, it is worth noting that when the front approaches the Deception Island entrance it has not been refracted enough to enter the aperture of the inner water body frontally. Instead, it moves eastward away from the coast. This fact can lead to limited penetration of the front into the inner water body which barely reaches the recording station. This therefore explains why a small amplitude (5 cm) is recorded at this station when

compared with the one at LIVMAR station. In addition, it could be possible that the recorded oscillations come from edge waves propagating along the insular shelf which could be generated by the meteotsunami interaction with the coastal margins (Niu, 2021). These trapped waves would move slower than the open sea fronts and would spend more time in reaching DECMAR station. Following Niu (2021), edge waves of lower frequency are able to surround a greater perimeter around the island. This favours the edge wave reaching points located on the opposite side (lee side) to the one on which the incident long-wave gave rise to the aforementioned edge wave. This could justify the relatively low value of the dominant frequency (0.75 cph) shown in the scalogram of the DECMAR record (**Figure 7.9b**). However, it must be remembered that in the aliased scalogram, that frequency could also be receiving contribution from a signal with a true frequency of 6.75 cph which is not resolved by the sampling interval of the 10-minute record. Therefore, the latter frequency could be that of the aforementioned edge waves. As can be seen in the previous section (**Figure 7.8**) both frequencies (0.75 and 6.75 cph) would be amplified by the inner water body geomorphology of Deception Island.

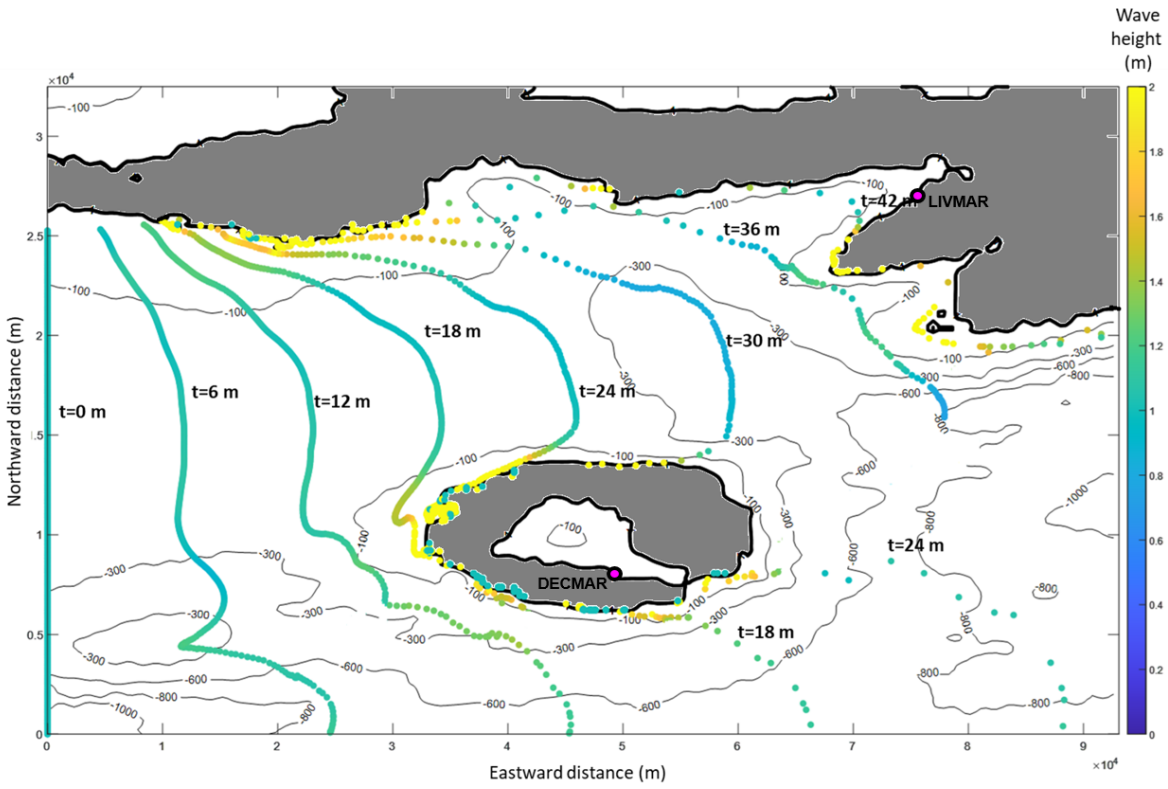


Figure 7.10 Refraction map of a long-wave front entering the western side of the studied region. Front evolution is shown at 6-minute intervals (t). The coastline is indicated by the thick black contour. In addition, some bathymetric contours are presented with thin grey lines and with labels indicating the bottom depth in metres. The two pink dots correspond to the pressure sensors of LIVMAR and DECMAR stations.

On the other hand, if the recorded signal at DECMAR has undergone an amplification process, another plausible cause for the delayed recording at DECMAR could be related to the time needed for this oscillation to gain a high enough amplitude to be detected in the sea level records.

The two previously mentioned mechanisms, together with the amplification factors discussed in the previous section, could explain the different frequency content and arrival time differences in the registered meteotsunami record.

Finally, it is worth noting that **Figure 7.10** reveals several coastal strips where the incident long waves undergo strong amplifications. These zones are those where the yellow and orange circles are located. Unfortunately, there are not any sea level stations in those locations to confirm this modelling.

7.6 Conclusions

In this manuscript, an analysis of the sea level records caused by the arrival of the meteotsunamis generated by the explosion of the Hunga Tonga-Hunga Ha'apai volcano has been presented. This analysis was conducted at two tide gauge stations located on Deception and Livingston Islands. The meteotsunami records are analysed along with atmospheric pressure records from nearby meteorological stations.

The assessing of the associated aliasing effects performed on the 1-minute interval records taken in La Jolla station, has shown that although the true-frequency distribution of the meteotsunami signal is not resolved by 10-minute interval sampling, the increase in amplitude detected in the scalogram spectrum allows to detect the arrival of the meteotsunami. This in turn enables capturing the approximate maximum amplitude exhibited in the true spectrum.

The atmospheric leading front arrived at the meteorological stations ~ 4 hours before the meteotsunami was recorded by the tide gauges. The passings of two atmospheric acoustic-gravity waves were clearly identified, one propagating eastwards and the other westwards. The meteotsunamis arriving in the study area showed amplitudes of up to 20 cm (Livingston) and 5 cm (Deception).

The analysis of the arrival time of the atmospheric pressure disturbances and the meteotsunamis at the corresponding measurement stations indicates that the meteotsunamis were triggered very close to the volcanic explosion.

A time-frequency analysis based on wavelet decomposition and the numerical computation of the meteotsunami refraction while approaching the stations have revealed that the meteotsunami oscillations show quite different frequency content between the two stations. This may be explained in terms of the different amplification factors experienced by the meteotsunami while it interacts with the different geomorphological configurations of the corresponding water bodies. The records also evidence a marked difference in the meteotsunami arrival time at the two stations which may be explained by the refraction effects on the meteotsunami fronts while they are approaching the two stations.

CHAPTER 8

Discussion

The present work has examined the spatio-temporal variability of sea level around Deception and Livingston Islands (South Shetland Islands, Antarctica), integrating in-situ observations, satellite data, and the analysis of extreme events. Chapters 5, 6 and 7 addressed three complementary aspects: the validation of radar altimetry in polar regions, the thermal evolution of coastal waters, and the oceanic response to a remote, planet-scale volcanic event (the Hunga Tonga–Hunga Ha'apai eruption).

The results obtained allow the assessment of the general hypothesis of this thesis. This hypothesis proposed that sea level variability in the South Shetland Islands is governed by a combination of extreme environmental conditions, such as sea ice formation, volcanic activity, atmospheric fluctuations and changes in ocean circulation, and that volcanic events, both local and remote, can produce transient signals detectable in high-resolution records.

To address this hypothesis, the study was guided by five objectives: establishing long-term sea level time series from in-situ data; evaluating the accuracy of Sentinel-3A/B satellite altimetry; assessing the influence of sea-ice presence on altimetric measurements; analysing long-term seawater temperature records; and assessing the impact of local and remote volcanic activity on sea level variability. Within this framework, the discussion develops progressively through the different themes analysed in the study, highlighting the advances achieved, the limitations encountered, and their coherence with previous studies.

A first aspect to consider is that obtaining continuous tide gauge records in polar regions remains a logistical challenge due to extreme weather conditions, seasonal sea-ice presence and constraints on instrument maintenance (Lei et al., 2018; Pytharouli et al., 2018). In this context, the present work has developed a robust protocol for producing continuous sea level series, resolving the jumps and discontinuities present in Antarctic station records. This procedure is also applicable to other polar regions where data continuity is often compromised by similar operational constrains, thereby reinforcing its applicability beyond the study area.

Consistency tests on annual harmonics and cross-comparison between the series confirm the reliability of the procedure and ensure the internal coherence of the data. Despite this, it was not possible to reference the series to the ellipsoid, which makes it impossible to obtain absolute sea level. This limitation, which arises from the difficulty of establishing a robust connection between the tide gauges and the available GNSS benchmarks, hampers direct comparison with other data sources. Even so, the absence of an absolute vertical reference

does not reduce the scientific value of the records, which accurately resolve interannual variability, seasonality and high-frequency fluctuations.

Looking ahead, strengthening the link between tide gauges and the geodetic network is particularly important in a region such as Livingston and Deception Islands, where vertical land motion may result from glacial loading, volcanic deformation and local tectonics. A stable and continuous geodetic-oceanographic reference frame would allow these land movements to be separated from true oceanic variability, improving the long-term interpretation of sea level trends. Overall, this provides a solid basis for long-term sea level monitoring in the South Shetland Islands, one of the most sensitive and least instrumented areas of the Antarctic system.

Complementing this in-situ analysis, the comparison between Sentinel-3A/B altimetric data and the tide gauge records from Livingston Island (Chapter 5) demonstrates that SAR-mode radar altimetry (SRAL) yields consistent results even at sub-Antarctic latitudes when using adapted processing parameters, such as sea state bias corrections and spatial averaging around the crossover point.

Correlation coefficients, together with the mean absolute deviation and the standard deviation of the differences, showed high sensitivity to these adjustments, confirming the need to optimise the processing algorithms for the specific regional and environmental conditions. This behaviour is consistent with findings by Aldarias et al. (2020), Fenoglio-Marc et al. (2015), Gómez-Enri et al. (2018) and Valle-Rodríguez et al. (2023), who highlighted the influence of data processing on altimetry accuracy. Other studies have reported even higher correlations in ice-affected areas, demonstrating that, under favourable conditions, an even stronger agreement between altimetry and tide gauge data may be achieved (Auger et al., 2021; Fenoglio-Marc et al., 2015).

In Antarctic areas, such discrepancies can be enhanced by high oceanic variability, intermittent sea ice presence, surface slope and heterogeneous backscatter, as indicated by Yang et al. (2019). During winter months, a generalized degradation of the signal was observed, associated with partial sea ice cover and extreme weather conditions, highlighting the need for adaptive processing strategies and dynamic ice masks. Nevertheless, the results confirm that the combination of an oceanic retracker and data processing is an effective tool for sea level monitoring in Antarctic regions where in-situ observations are scarce.

The temporal extent of this validation, one of the longest conducted in Antarctica, enables an assessment of altimetric performance across a wide range of environmental conditions, including winters with differing sea-ice coverage, and provides a robust perspective on long-term product stability. These results are relevant not only for Sentinel-3A/B but also for upcoming missions focused on polar monitoring, such as ESA's CRISTAL mission, in which improved SAR retracking and handling of sea ice will be essential for ensuring reliable observations at high latitudes.

Closely related to this, the influence of sea ice presence on altimetry performance is examined. The quality of altimetric measurements showed a marked dependence on sea ice coverage, periods with sea ice presence significantly reduced the correlation between Sentinel-3 data and tide gauge records. These findings are consistent with those of Peng et al. (2024), Prandi et al. (2012) and Rose et al. (2019), who demonstrated that radar retracking over mixed ice-water surfaces distorts waveform shapes, reducing the accuracy of the retracking products.

During ice-free periods, coherence between the two series was high, confirming that the observed errors are mainly seasonal and linked to surface conditions. The combined use of Sentinel-1 SAR imagery allowed mapping of sea-ice extent and its direct correlation with periods of greater altimetric error, providing complementary visual validation. These results align with Passaro et al. (2021) and Venables et al. (2023), who recommend adaptive retracking and dynamic masking for optimising observations in polar regions. In this sense, the integration of SAR altimetry with remote sensing data and in-situ observations emerges as an essential approach for extending continuous sea level monitoring in sea ice affected areas.

In parallel, long-term seawater temperature records provide essential context for understanding the physical environment of the region. The seawater temperature series from LIVMAR and DECMAR stations show that the surface thermal regime in the South Shetland Islands is controlled by the combined influence of regional climatic forcing and local oceanographic and geodynamic processes. Both stations display a marked seasonality, consistent with previous descriptions for the western Antarctic Peninsula (Clarke et al., 2008; Lenn et al., 2003; Meredith et al., 2008), although with systematic differences. Livingston exhibits colder and more regular winters, influenced by water inflow from the Bransfield Strait and seasonal discharge from Johnsons Glacier, while Deception shows a

larger thermal amplitude and more abrupt episodes associated with geothermal input and volcanic activity in Port Foster (Berrocoso et al., 2018; Moreno-Vacas & Almendros, 2021).

The overall warming trend observed in both series is coherent with the documented increase in air temperature in the region (Turner et al., 2021) and suggests a direct coupling between the atmosphere and the ocean surface layer. This reinforces the interpretation that regional warming is a dominant driver of recent thermal evolution in the northern South Shetland Islands.

A notable feature is the reduction in episodes with temperatures close to the freezing point (-1.8 °C) during recent winters. This may be explained by the combination of regional atmospheric warming and the advection of relatively warmer waters transported by the Bransfield Current, the main exchange pathway with the archipelago (Sangrà et al., 2011, 2017; Veny et al., 2022). The temporal coincidence with the thermal anomaly associated with the Orca volcano eruption (Rodrigo et al., 2018) suggests that volcanic heat input may have contributed locally to reducing the frequency of waters below the freezing point, particularly in Deception. However, determining whether this reduction reflects a sustained trend or a transient effect will require analysis of forthcoming observational campaigns, especially to assess whether winter temperatures fall below -1.8 °C once the volcanic influence has dissipated.

Overall, the evidence indicates a progressive shift towards warmer surface conditions, less favourable to the formation of coastal ice. The sensitivity of marine temperature to regional climatic forcing, Bransfield Strait circulation and volcanic activity underscores the need for continued monitoring to separate climatic variability from local oceanographic and geodynamic signals. This analysis therefore provides an essential oceanographic framework for interpreting the processes analysed throughout the thesis.

Finally, the impact of volcanic activity on sea level variability was considered. The analysis of the Hunga Tonga–Hunga Ha'apai eruption confirms that atmospheric disturbances generated by remote volcanic processes can produce detectable sea level responses at very large distances from their source, even in polar regions such as the South Shetland Islands. The meteorological stations at Juan Carlos I and Gabriel de Castilla clearly recorded the passage of the Lamb wave, with amplitudes consistent with global reports for the eastward travelling disturbance and with the attenuation expected as the wave propagated over long distances (Kataoka et al., 2022; Nishida et al., 2014). The double arrival of the perturbation,

first from the east and later from the west with reduced amplitude, is consistent with the concentric propagation of acoustic-gravity waves, as reported in recent studies (Omira et al., 2022).

Regarding the oceanic response, the comparison between the arrival times of the Lamb wave and the sea level oscillations allowed ruling out a meteotsunami generated by the direct barometric mechanism (inverse barometer; Vilibić, (2008). As described in the chapter, such a component should have arrived simultaneously with the atmospheric disturbance but did not appear in the Antarctic records, consistent with cases documented elsewhere where the primary signal is too weak to be detected by tide gauges with moderate sampling rates.

Consequently, the oscillations recoded at Livingston and Deception Islands are interpreted as secondary meteotsunamis (Omira et al., 2022). Amplitudes reached ~20 cm at LIVMAR and ~5 cm at DECMAR, reflecting clear modulation by local bathymetry and basin geometry. This behaviour is consistent with theories of amplification controlled by seafloor relief and local resonance (Koutitas, 1988; Vilibić, 2008).

A methodological aspect to consider is the temporal resolution of the Antarctic series. The 10-minute sampling interval introduces limiting factors such as aliasing, which reduces the ability to resolve the higher frequency components of the event. This highlights the need for greater sampling rates in future deployments to capture such high frequency disturbances.

Regarding local volcanic activity, it was initially intended to assess whether the location of DECMAR within an active caldera could introduce specific signals in sea level distinct from those recorded in a non-volcanic setting such as Livingston. However, the complexity of the Deception Island records, characterised by internal variability that exceeds the scope of the present analysis, has so far prevented robust identification of a possible volcanic contribution. Addressing this question requires a multiparametric approach combining tide gauge, thermal, geodetic and seismic observations, and is therefore proposed as a priority for future studies.

Taken together, these findings provide an integrated understanding of the processes analysed in this thesis. The establishment of continuous tide gauge series provides the observational foundation required to validate and contextualise satellite altimetry, while the analysis of sea ice influence clarifies the conditions under which altimetry yields reliable estimates in polar environments.

The incorporation of the surface thermal regime adds an essential physical framework for interpreting both sea level dynamics and the differences between Livingston and Deception, integrating regional climatic processes, ocean circulation and local geodynamic factors. Finally, the response of Antarctic stations to the Hunga Tonga-Hunga Ha'apai eruption acts as a cohesive element, testing simultaneously the sensitivity of the tide gauges, instrumental limitations and the modulatory role of coastal geomorphology.

In synthesis, this research establishes a multidisciplinary framework in which in-situ observations, satellite data and environmental forcing analysis converge to provide an integrated view of the system. This complementarity constitutes one of the major methodological strengths of the work and establishes a solid basis for future research.

CHAPTER 9

Conclusions

- The optimisation of processing parameters (number of measurements, SSB correction and the percentege of Significant Wave Height) improves the consistency between satellite altimetry and tide gauge observations.
- The presence of sea ice is the main factor degrading the quality of altimetric measurements, reducing correlations and increasing standard deviations.
- Adaptive retracking techniques or dynamic masking approaches are recommended as potential future improvements for altimetry in ice-affected regions.
- Seawater temperature series at DECMAR and LIVMAR stations exhibit marked seasonality, but with contrasting patterns linked to volcanic influence at Deception Island and glacial influence at Livingston Island.
- A positive correlation between air and sea water temperatures was observed over the past decade, with a slight upward trend in both series.
- Regional tectonic and volcanic activity, associated with the Phoenix microplate and the Bransfield Rift, contributes to local seawater warming.
- Volcanic events in 2015 and 2020 are clearly recorded in the temperature series, with stronger effects at Deception, demonstrating the impact of geodynamic processes on regional thermal variability.
- Tide gauges in the South Shetland Islands recorded meteotsunamis with amplitudes of up to 20 cm at Livingston and 5 cm at Deception.
- The delay of approximately four hours between the arrival of atmospheric pressure disturbances and the tide gauge signals confirms their direct connection to the volcanic explosion.
- Spectral and refraction analyses revealed differences in frequency and arrival times between the two stations, attributed to local amplification factors and coastal geomorphological effects.
- Sea level records highlight the importance of high-resolution datasets for meteotsunami detection and spectral analysis.
- The combined studies demonstrate the interplay between local processes (sea ice, volcanic activity, coastal morphology) and remote forcings (HTHH meteotsunami) in influencing sea level and temperature variability in the Antarctic region.

Future Research Lines

The results obtained throughout this thesis are consistent with the proposed objectives and contribute to advancing the understanding of sea level variability in the South Shetland Islands. At the same time, they highlight the importance of refining observational methods and enhancing collaboration across disciplines and institutions to ensure more robust and continuous datasets. The following points outline the main lines for future investigation:

▪ Development of alternative referencing methods for establishing a consistent vertical datum in the sea level series from the DECMAR and LIVMAR stations.

▪ Implementation of absolute sea level comparisons between tide gauge records and Sentinel-3A/B altimetry, once suitable levelling data become available.

▪ Comparative analysis of sea level variability between Deception Island, an active volcanic setting, and Livingston Island, a non-volcanic environment, to assess potential differences in local sea level response considering tectonic and/or volcanic deformation and glacial isostatic adjustment.

▪ Investigation of volcanic activity impacts on sea level, with particular emphasis on events such as the Orca seamount activity of August 2020.

▪ Assessment of seismic influences on sea level perturbations, including the detection and characterisation of anomalies caused by nearby earthquakes (case in the Sothern Drake Passage, August 2025).

▪ Application of machine learning techniques for the classification of sea-ice conditions and improved identification of open-water leads in Antarctic altimetry data.

▪ Inter-annual variability of tidal constituents.

References

Aldarias, A., Gómez-Enri, J., Laiz, I., Tejedor, B., Vignudelli, S., & Cipollini, P. (2020). Validation of Sentinel-3A SRAL Coastal Sea Level Data at High Posting Rate: 80 Hz. *IEEE Transactions on Geoscience and Remote Sensing*, *58*(6), 3809–3821. https://doi.org/10.1109/TGRS.2019.2957649

Alevropoulos-Borrill, A., Golledge, N. R., Cornford, S. L., Lowry, D. P., & Krapp, M. (2024). Sustained ocean cooling insufficient to reverse sea level rise from Antarctica. *Communications Earth & Environment*, *5*(1), 1–9. https://doi.org/10.1038/s43247-024-01297-8

Almendros, J., Carmona, E., Jiménez, V., Díaz-Moreno, A., & Lorenzo, F. (2018). Volcano-Tectonic Activity at Deception Island Volcano Following a Seismic Swarm in the Bransfield Rift (2014–2015). *Geophysical Research Letters*, *45*(10), 4788–4798. https://doi.org/10.1029/2018GL077490

Almendros, J., Wilcock, W., Soule, D., Teixidó, T., Vizcaíno, L., Ardanaz, O., Granja-Bruña, J. L., Martín-Jiménez, D., Yuan, X., Heit, B., Schmidt-Aursch, M. C., Geissler, W., Dziak, R., Carrión, F., Ontiveros, A., Abella, R., Carmona, E., Agüí-Fernández, J. F., Sánchez, N., … Schmahl, L. (2020). BRAVOSEIS: Geophysical investigation of rifting and volcanism in the Bransfield strait, Antarctica. *Journal of South American Earth Sciences*, *104*, 102834. https://doi.org/10.1016/j.jsames.2020.102834

Amores, A., Monserrat, S., Marcos, M., Argüeso, D., Villalonga, J., Jordà, G., & Gomis, D. (2022). Numerical Simulation of Atmospheric Lamb Waves Generated by the 2022 Hunga-Tonga Volcanic Eruption. *Geophysical Research Letters*, *49*(6), e2022GL098240. https://doi.org/10.1029/2022GL098240

Andersen, O. B., Nielsen, K., Williams, S. D. P., Khan, S. A., & Kern, M. (2019). *Artic water level and tides from GNSS-R and satellite altimetry—The Greenland case.*

2019, G51A-02. AGU Fall Meeting Abstracts. https://ui.adsabs.harvard.edu/abs/2019AGUFM.G51A..02A

Anderson, E. J., Stow, C. A., Gronewold, A. D., Mason, L. A., McCormick, M. J., Qian, S. S., Ruberg, S. A., Beadle, K., Constant, S. A., & Hawley, N. (2021). Seasonal overturn and stratification changes drive deep-water warming in one of Earth's largest lakes. *Nature Communications*, *12*(1), 1688. https://doi.org/10.1038/s41467-021-21971-1

Anup, N., Rohith, B., Vijith, V., Rose, L., Sreeraj, P., Sabu, A., Krishnamohan, K. S., Sudeepkumar, B. L., Sunil, A. S., & Sunil, P. S. (2024). Volcanic Eruption Triggers a Rare Meteotsunami in the Indian Ocean. *Geophysical Research Letters*, *51*(2), e2023GL108036. https://doi.org/10.1029/2023GL108036

Armitage, T. W. K., Bacon, S., Ridout, A. L., Thomas, S. F., Aksenov, Y., & Wingham, D. J. (2016). Arctic sea surface height variability and change from satellite radar altimetry and GRACE, 2003–2014. *Journal of Geophysical Research: Oceans*, *121*(6), 4303–4322. https://doi.org/10.1002/2015JC011579

Armitage, T. W. K., & Davidson, M. W. J. (2014). Using the Interferometric Capabilities of the ESA CryoSat-2 Mission to Improve the Accuracy of Sea Ice Freeboard Retrievals. *IEEE Transactions on Geoscience and Remote Sensing*, *52*(1), 529–536. https://doi.org/10.1109/TGRS.2013.2242082

Armitage, T. W. K., Kwok, R., Thompson, A. F., & Cunningham, G. (2018). Dynamic Topography and Sea Level Anomalies of the Southern Ocean: Variability and Teleconnections. *Journal of Geophysical Research: Oceans*, *123*(1), 613–630. https://doi.org/10.1002/2017JC013534

Auger, M., Morrow, R., Kestenare, E., Sallée, J.-B., & Cowley, R. (2021). Southern Ocean in-situ temperature trends over 25 years emerge from interannual variability. *Nature Communications*, *12*(1), 514. https://doi.org/10.1038/s41467-020-20781-1

Auger, M., Prandi, P., & Sallée, J.-B. (2022). Southern ocean sea level anomaly in the sea ice-covered sector from multimission satellite observations. *Scientific Data*, *9*(1), 70. https://doi.org/10.1038/s41597-022-01166-z

Baraldo, A. (1999). *Evolución geológica de la isla Decepción, islas Shetland del Sur, Antártida* [Buenos Aires University]. http://digital.bl.fcen.uba.ar/Download/Tesis/Tesis_3174_Baraldo.pdf

Barker, D. H. N., & Austin, J. A. (1998). Rift propagation, detachment faulting, and associated magmatism in Bransfield Strait, Antarctic Peninsula. *Journal of Geophysical Research: Solid Earth*, *103*(B10), 24017–24043. https://doi.org/10.1029/98JB01117

Barker, P. F. (1982). The Cenozoic subduction history of the Pacific margin of the Antarctic Peninsula: Ridge crest–trench interactions. *Journal of the Geological Society*, *139*(6), 787–801. https://doi.org/10.1144/gsjgs.139.6.0787

Barnes, D. K. A., & Conlan, K. E. (2007). Disturbance, colonization and development of Antarctic benthic communities. *Philosophical Transactions of the Royal Society B: Biological Sciences*, *362*(1477), 11–38. https://doi.org/10.1098/rstb.2006.1951

Barnes, D. K. A., Fuentes, V., Clarke, A., Schloss, I. R., & Wallace, M. I. (2006). Spatial and temporal variation in shallow seawater temperatures around Antarctica. *Deep Sea Research Part II: Topical Studies in Oceanography*, *53*(8–10), 853–865. https://doi.org/10.1016/j.dsr2.2006.03.008

Beckley, B. D., Callahan, P. S., Hancock, D. W., Mitchum, G. T., & Ray, R. D. (2017). On the "Cal-Mode" Correction to TOPEX Satellite Altimetry and Its Effect on the

Global Mean Sea Level Time Series. *Journal of Geophysical Research: Oceans*, *122*(11), 8371–8384. https://doi.org/10.1002/2017JC013090

Benveniste, J., Cazenave, A., Vignudelli, S., Fenoglio-Marc, L., Shah, R., Almar, R., Andersen, O., Birol, F., Bonnefond, P., Bouffard, J., Calafat, F., Cardellach, E., Cipollini, P., Le Cozannet, G., Dufau, C., Fernandes, M. J., Frappart, F., Garrison, J., Gommenginger, C., … Wöppelmann, G. (2019). Requirements for a Coastal Hazards Observing System. *Frontiers in Marine Science*, *6*, 348. https://doi.org/10.3389/fmars.2019.00348

Berrocoso, M., Prates, G., Fernández-Ros, A., Peci, L. M., De Gil, A., Rosado, B., Páez, R., & Jigena, B. (2018). Caldera unrest detected with seawater temperature anomalies at Deception Island, Antarctic Peninsula. *Bulletin of Volcanology*, *80*(4), 41. https://doi.org/10.1007/s00445-018-1216-2

Birkett, C. M., & Beckley, B. (2010). Investigating the Performance of the Jason-2/OSTM Radar Altimeter over Lakes and Reservoirs. *Marine Geodesy*, *33*(sup1), 204–238. https://doi.org/10.1080/01490419.2010.488983

Bohoyo, F., Galindo-Zaldívar, J., Maldonado, A., Schreider, A. A., & Suriñach, E. (2002). Basin development subsequent to ridge-trench collision: The Jane Basin, Antarctica. *Marine Geophysical Researches*, *23*(5/6), 413–421. https://doi.org/10.1023/B:MARI.0000018194.18098.0d

Bolado-Penagos, M., Sala, I., Gomiz-Pascual, J. J., Romero-Cózar, J., González-Fernández, D., Reyes-Pérez, J., Vázquez, A., & Bruno, M. (2021). Revising the Effects of Local and Remote Atmospheric Forcing on the Atlantic Jet and Western Alboran Gyre Dynamics. *Journal of Geophysical Research: Oceans*, *126*(2), e2020JC016173. https://doi.org/10.1029/2020JC016173

Bonnefond, P., Haines, B. J., & Watson, C. (2011). In situ Absolute Calibration and Validation: A Link from Coastal to Open-Ocean Altimetry. In S. Vignudelli, A. G. Kostianoy, P. Cipollini, & J. Benveniste (Eds.), *Coastal Altimetry* (pp. 259–296). Springer Berlin Heidelberg. https://doi.org/10.1007/978-3-642-12796-0_11

Brenna, M., Cronin, S. J., Smith, I. E. M., Pontesilli, A., Tost, M., Barker, S., Tonga'onevai, S., Kula, T., & Vaiomounga, R. (2022). Post-caldera volcanism reveals shallow priming of an intra-ocean arc andesitic caldera: Hunga volcano, Tonga, SW Pacific. *Lithos*, *412–413*, 106614. https://doi.org/10.1016/j.lithos.2022.106614

Bruni, S., Fenoglio, L., Raicich, F., & Zerbini, S. (2022). On the consistency of coastal sea-level measurements in the Mediterranean Sea from tide gauges and satellite radar altimetry. *Journal of Geodesy*, *96*(6), 41. https://doi.org/10.1007/s00190-022-01626-9

Bulczak, A. I., Bacon, S., Naveira Garabato, A. C., Ridout, A., Sonnewald, M. J. P., & Laxon, S. W. (2015). Seasonal variability of sea surface height in the coastal waters and deep basins of the Nordic Seas. *Geophysical Research Letters*, *42*(1), 113–120. https://doi.org/10.1002/2014GL061796

Calleja, J. F., Corbea-Pérez, A., Fernández, S., Recondo, C., Peón, J., & De Pablo, M. Á. (2019). Snow Albedo Seasonality and Trend from MODIS Sensor and Ground Data at Johnsons Glacier, Livingston Island, Maritime Antarctica. *Sensors*, *19*(16), 3569. https://doi.org/10.3390/s19163569

Cárdenas, C. A., González-Aravena, M., & Santibañez, P. A. (2018). The importance of local settings: Within-year variability in seawater temperature at South Bay, Western Antarctic Peninsula. *PeerJ*, *6*, e4289. https://doi.org/10.7717/peerj.4289

Carrasco, J. F., Bozkurt, D., & Cordero, R. R. (2021). A review of the observed air temperature in the Antarctic Peninsula. Did the warming trend come back after the

early 21st hiatus? *Polar Science*, *28*, 100653. https://doi.org/10.1016/j.polar.2021.100653

Carrère, L., & Lyard, F. (2003). Modeling the barotropic response of the global ocean to atmospheric wind and pressure forcing—Comparisons with observations. *Geophysical Research Letters*, *30*(6). https://doi.org/10.1029/2002GL016473

Cartwright, D. E., & Tayler, R. J. (1971). New Computations of the Tide-generating Potential. *Geophysical Journal of the Royal Astronomical Society*, *23*(1), 45–73. https://doi.org/10.1111/j.1365-246X.1971.tb01803.x

Caselli, A. T., Badi, G., Bonatto, A. L., Bengoa, C. L., Agusto, M. R., Bidone, A., & Ibáñez, J. (2007). Seismic activity and an anomalous fumarolic chemical composition due to seal effect in the volcanic system of Deception Island (Antarctica). *Revista de La Asociacion Geologica Argentina*, *62*(4), 545–552. https://bibliotecadigital.exactas.uba.ar/collection/paper/document/paper_00044822_v62_n4_p545_Caselli

Cazenave, A., & Remy, F. (2011). Sea level and climate: Measurements and causes of changes. *WIREs Climate Change*, *2*(5), 647–662. https://doi.org/10.1002/wcc.139

Cesca, S., Sugan, M., Rudzinski, Ł., Vajedian, S., Niemz, P., Plank, S., Petersen, G., Deng, Z., Rivalta, E., Vuan, A., Plasencia Linares, M. P., Heimann, S., & Dahm, T. (2022). Massive earthquake swarm driven by magmatic intrusion at the Bransfield Strait, Antarctica. *Communications Earth & Environment*, *3*(1), 1–11. https://doi.org/10.1038/s43247-022-00418-5

Church, J., Clark, P., Cazenave, A., Gregory, J., Jevrejeva, S., Levermann, A., Merrifield, M., Milne, G., Nerem, R., Nunn, P., Payne, A., Pfeffer, W., Stammer, D., & Unnikrishnan, A. (2013). “Chapter 13: Sea Level Change” in Climate Change 2013: The Physical Science Basis: Contribution of Working Group I to the Fifth

Assessment Report of the Intergovernmental Panel on Climate Change. *State & Federal Reports and Publications*. https://digitalcommons.humboldt.edu/hsuslri_state/25

Clarke, A., Meredith, M. P., Wallace, M. I., Brandon, M. A., & Thomas, D. N. (2008). Seasonal and interannual variability in temperature, chlorophyll and macronutrients in northern Marguerite Bay, Antarctica. *Deep Sea Research Part II: Topical Studies in Oceanography*, *55*(18–19), 1988–2006. https://doi.org/10.1016/j.dsr2.2008.04.035

Cleveland, R. B., Cleveland, W. S., McRae, J. E., & Terpenning, I. (1990). STL: A seasonal-trend decomposition. *J. off. Stat*, *6*(1), 3–73. http://www.nniiem.ru/file/news/2016/stl-statistical-model.pdf

Codiga, D. L. (2011). *Unified tidal analysis and prediction using the UTide Matlab functions*. Graduate School of Oceanography, University of Rhode Island. https://doi.org/10.13140/RG.2.1.3761.2008

Cook, A. J., Holland, P. R., Meredith, M. P., Murray, T., Luckman, A., & Vaughan, D. G. (2016). Ocean forcing of glacier retreat in the western Antarctic Peninsula. *Science*, *353*(6296), 283–286. https://doi.org/10.1126/science.aae0017

Dählmann, A., Wallmann, K., Sahling, H., Sarthou, G., Bohrmann, G., Petersen, S., Chin, C. S., & Klinkhammer, G. P. (2001). Hot vents in an ice-cold ocean: Indications for phase separation at the southernmost area of hydrothermal activity, Bransfield Strait, Antarctica. *Earth and Planetary Science Letters*, *193*(3–4), 381–394. https://doi.org/10.1016/S0012-821X(01)00535-0

Damini, B. Y., Kerr, R., Dotto, T. S., & Mata, M. M. (2022). Long-term changes on the Bransfield Strait deep water masses: Variability, drivers and connections with the

northwestern Weddell Sea. *Deep Sea Research Part I: Oceanographic Research Papers*, *179*, 103667. https://doi.org/10.1016/j.dsr.2021.103667

Defant, A. (1961). *Physical Oceanography: Vol. I*. New York: Pergamon Press.

Dieng, H. B., Cazenave, A., Gouzenes, Y., & Sow, B. A. (2021). Trends and inter-annual variability of altimetry-based coastal sea level in the Mediterranean Sea: Comparison with tide gauges and models. *Advances in Space Research*, *68*(8), 3279–3290. https://doi.org/10.1016/j.asr.2021.06.022

Dinardo, S., Fenoglio-Marc, L., Becker, M., Scharroo, R., Fernandes, M. J., Staneva, J., Grayek, S., & Benveniste, J. (2021). A RIP-based SAR retracker and its application in North East Atlantic with Sentinel-3. *Advances in Space Research*, *68*(2), 892–929. https://doi.org/10.1016/j.asr.2020.06.004

Dinardo, S., Fenoglio-Marc, L., Buchhaupt, C., Becker, M., Scharroo, R., Joana Fernandes, M., & Benveniste, J. (2018). Coastal SAR and PLRM altimetry in German Bight and West Baltic Sea. *Advances in Space Research*, *62*(6), 1371–1404. https://doi.org/10.1016/j.asr.2017.12.018

Dinardo, S., Lucas, B., & Benveniste, J. (2015). Sentinel-3 STM SAR ocean retracking algorithm and SAMOSA model. *2015 IEEE International Geoscience and Remote Sensing Symposium (IGARSS)*, 5320–5323. https://doi.org/10.1109/IGARSS.2015.7327036

Doodson, A. T. (1921). The harmonic development of the tide-generating potential. *Proceedings of the Royal Society of London. Series A, Containing Papers of a Mathematical and Physical Character*, *100*(704), 305–329. https://doi.org/10.1098/rspa.1921.0088

Dotto, T. S., Naveira Garabato, A., Bacon, S., Tsamados, M., Holland, P. R., Hooley, J., Frajka-Williams, E., Ridout, A., & Meredith, M. P. (2018). Variability of the Ross

Gyre, Southern Ocean: Drivers and Responses Revealed by Satellite Altimetry. *Geophysical Research Letters*, *45*(12), 6195–6204. https://doi.org/10.1029/2018GL078607

Dragani W. C., Drabble M. R., D'Onofrio E. E., & Mazio C. A. (2004). Propagation and amplification of tide at the Bransfield and Gerlache Straits, northwestern Antarctic Peninsula. *Polar geoscience*, *17*, 156–170. https://nipr.repo.nii.ac.jp/records/3141

Elderfield, H. (1972). Effects of volcanism on water chemistry, Deception Island, Antarctica. *Marine Geology*, *13*(1), M1–M6. https://doi.org/10.1016/0025-3227(72)90066-7

ESA. (2023). *Ice loss from Greenland and Antarctica hits new record*. https://www.esa.int/Applications/Observing_the_Earth/FutureEO/CryoSat/Ice_loss_from_Greenland_and_Antarctica_hits_new_record

EUMETSAT For Copernicus & European Organisation For The Exploitation Of Meteorological Satellites. (2022). *SRAL Level 1B (version BC004)—Sentinel-3—Reprocessed* (Version BC004) [SENTINEL-SAFE]. European Organisation for the Exploitation of Meteorological Satellites. https://doi.org/10.15770/EUM_SEC_CLM_0075

EUMETSAT For Copernicus & European Organisation For The Exploitation Of Meteorological Satellites. (2023). *SRAL Level 2 Altimetry Global (version BC005)—Sentinel-3—Reprocessed* (Version BC005) [SENTINEL-SAFE]. European Organisation for the Exploitation of Meteorological Satellites. https://doi.org/10.15770/EUM_SEC_CLM_0089

Fenoglio, L., Dinardo, S., Uebbing, B., Buchhaupt, C., Gärtner, M., Staneva, J., Becker, M., Klos, A., & Kusche, J. (2021). Advances in NE-Atlantic coastal sea level change monitoring by Delay Doppler altimetry. *Advances in Space Research*, *68*(2), 571–592. https://doi.org/10.1016/j.asr.2020.10.041

Fenoglio-Marc, L., Dinardo, S., Scharroo, R., Roland, A., Dutour Sikiric, M., Lucas, B., Becker, M., Benveniste, J., & Weiss, R. (2015). The German Bight: A validation of CryoSat-2 altimeter data in SAR mode. *Advances in Space Research*, *55*(11), 2641–2656. https://doi.org/10.1016/j.asr.2015.02.014

Flexas, M. M., Arias, M. R., & Ojeda, M. A. (2017). Hydrography and dynamics of Port Foster, Deception Island, Antarctica. *Antarctic Science*, *29*(1), 83–93. https://doi.org/10.1017/S0954102016000444

Foldvik, A., & Kvinge, T. (1974). Conditional instability of sea water at the freezing point. *Deep Sea Research and Oceanographic Abstracts*, *21*(3), 169–174. https://doi.org/10.1016/0011-7471(74)90056-4

Foreman, M. G. G., & Henry, R. F. (1989). The harmonic analysis of tidal model time series. *Advances in Water Resources*, *12*(3), 109–120. https://doi.org/10.1016/0309-1708(89)90017-1

Fredensborg Hansen, R. M., Rinne, E., & Skourup, H. (2021). Classification of Sea Ice Types in the Arctic by Radar Echoes from SARAL/AltiKa. *Remote Sensing*, *13*(16), 3183. https://doi.org/10.3390/rs13163183

Frölicher, T. L., Sarmiento, J. L., Paynter, D. J., Dunne, J. P., Krasting, J. P., & Winton, M. (2015). Dominance of the Southern Ocean in Anthropogenic Carbon and Heat Uptake in CMIP5 Models. *Journal of Climate*, *28*(2), 862–886. https://doi.org/10.1175/JCLI-D-14-00117.1

Fu, Y., Zhou, X., Zhou, D., Li, J., & Zhang, W. (2021). Estimation of sea level variability in the South China Sea from satellite altimetry and tide gauge data. *Advances in Space Research*, *68*(2), 523–533. https://doi.org/10.1016/j.asr.2019.07.001

Galassi, G., & Spada, G. (2017). Tide gauge observations in Antarctica (1958–2014) and recent ice loss. *Antarctic Science*, *29*(4), 369–381. https://doi.org/10.1017/S0954102016000729

Gao, F., Wang, X., Gao, Y., Dong, J., & Wang, S. (2019). Sea Ice Change Detection in SAR Images Based on Convolutional-Wavelet Neural Networks. *IEEE Geoscience and Remote Sensing Letters*, *16*(8), 1240–1244. https://doi.org/10.1109/LGRS.2019.2895656

García, M. A., López, O., Sospedra, J., Espino, M., Gràcia, V., Morrison, G., Rojas, P., Figa, J., Puigdefàbregas, J., & S.-Arcilla, A. (1994). Mesoscale variability in the Bransfield Strait region (Antarctica) during Austral summer. *Annales Geophysicae*, *12*(9), 856–867. https://doi.org/10.1007/s00585-994-0856-z

Garnier, F., Bocquet, M., Fleury, S., Bouffard, J., Tsamados, M., Remy, F., Garric, G., & Chenal, A. (2022). Latest Altimetry-Based Sea Ice Freeboard and Volume Inter-Annual Variability in the Antarctic over 2003–2020. *Remote Sensing*, *14*(19), Article 19. https://doi.org/10.3390/rs14194741

Godin, G. (1972). *The Analysis of Tides*. University of Toronto Press.

Gómez-Enri, J., Vignudelli, S., Cipollini, P., Coca, J., & González, C. J. (2018). Validation of CryoSat-2 SIRAL sea level data in the eastern continental shelf of the Gulf of Cadiz (Spain). *Advances in Space Research*, *62*(6), 1405–1420. https://doi.org/10.1016/j.asr.2017.10.042

González-Casado, J. M., Giner Robles, J. L., & López-Martínez, J. (2000). Bransfield Basin, Antarctic Peninsula: Not a normal backarc basin. *Geology*, *28*(11), 1043. https://doi.org/10.1130/0091-7613(2000)28<1043:BBAPNA>2.0.CO;2

Grad, M., Guterch, A., & Środa, P. (1992). Upper crustal structure of Deception Island area, Bransfield Strait, West Antarctica. *Antarctic Science*, *4*(4), 469–476. https://doi.org/10.1017/S0954102092000683

Gusman, A. R., Roger, J., Noble, C., Wang, X., Power, W., & Burbidge, D. (2022). The 2022 Hunga Tonga-Hunga Ha'apai Volcano Air-Wave Generated Tsunami. *Pure and Applied Geophysics*, *179*(10), 3511–3525. https://doi.org/10.1007/s00024-022-03154-1

Hafen, R. (2016). *stlplus: Enhanced Seasonal Decomposition of Time Series by Loess* (p. 0.5.1) [Dataset]. https://doi.org/10.32614/CRAN.package.stlplus

Halimi, A., Mailhes, C., Tourneret, J.-Y., Thibaut, P., & Boy, F. (2014). A Semi-Analytical Model for Delay/Doppler Altimetry and Its Estimation Algorithm. *IEEE Transactions on Geoscience and Remote Sensing*, *52*(7), 4248–4258. https://doi.org/10.1109/TGRS.2013.2280595

Hamlington, B. D., Bellas-Manley, A., Willis, J. K., Fournier, S., Vinogradova, N., Nerem, R. S., Piecuch, C. G., Thompson, P. R., & Kopp, R. (2024). The rate of global sea level rise doubled during the past three decades. *Communications Earth & Environment*, *5*(1), 1–4. https://doi.org/10.1038/s43247-024-01761-5

Harkrider, D., & Press, F. (1967). The Krakatoa Air-Sea Waves: An Example of Pulse Propagation in Coupled Systems. *Geophysical Journal International*, *13*(1–3), 149–159. https://doi.org/10.1111/j.1365-246X.1967.tb02150.x

Harrison, G. (2022). Pressure anomalies from the JANUARY 2022 HUNGA TONGA-HUNGA HA'APAI eruption. *Weather*, *77*(3), 87–90. https://doi.org/10.1002/wea.4170

Heidarzadeh, M., Gusman, A. R., Ishibe, T., Sabeti, R., & Šepić, J. (2022). Estimating the eruption-induced water displacement source of the 15 January 2022 Tonga volcanic

tsunami from tsunami spectra and numerical modelling. *Ocean Engineering*, *261*, 112165. https://doi.org/10.1016/j.oceaneng.2022.112165

Heinrich, P., Gailler, A., Dupont, A., Rey, V., Hébert, H., & Listowski, C. (2023). Observations and simulations of the meteotsunami generated by the Tonga eruption on 15 January 2022 in the Mediterranean Sea. *Geophysical Journal International*, *234*(2), 903–914. https://doi.org/10.1093/gji/ggad092

Henriet, J. P., Meissner, R., Miller, H., & The Grape Team. (1992). Active margin processes along the Antarctic Peninsula. *Tectonophysics*, *201*(3–4), 229–253. https://doi.org/10.1016/0040-1951(92)90235-x

Hersbach, H., Bell, B., Berrisford, P., Hirahara, S., Horányi, A., Muñoz-Sabater, J., Nicolas, J., Peubey, C., Radu, R., Schepers, D., Simmons, A., Soci, C., Abdalla, S., Abellan, X., Balsamo, G., Bechtold, P., Biavati, G., Bidlot, J., Bonavita, M., … Thépaut, J. (2020). The ERA5 global reanalysis. *Quarterly Journal of the Royal Meteorological Society*, *146*(730), 1999–2049. https://doi.org/10.1002/qj.3803

Hofmann, E. E., Klinck, J. M., Lascara, C. M., & Smith, D. A. (1996). Water mass distribution and circulation west of the Antarctic Peninsula and including Bransfield Strait. In E. E. Hofmann, R. M. Ross, & L. B. Quetin (Eds.), *Antarctic Research Series* (Vol. 70, pp. 61–80). American Geophysical Union. https://doi.org/10.1029/AR070p0061

Huneke, W. G. C., Huhn, O., & Schröeder, M. (2016). Water masses in the Bransfield Strait and adjacent seas, austral summer 2013. *Polar Biology*, *39*(5), 789–798. https://doi.org/10.1007/s00300-016-1936-8

Hunt, B. M., Hoefling, K., & Cheng, C.-H. C. (2003). Annual warming episodes in seawater temperatures in McMurdo Sound in relationship to endogenous ice in notothenioid

fish. *Antarctic Science*, *15*(3), 333–338. https://doi.org/10.1017/S0954102003001342

Intergovernmental Panel on Climate Change (IPCC). (2022). *The Ocean and Cryosphere in a Changing Climate: Special Report of the Intergovernmental Panel on Climate Change* (1st ed.). Cambridge University Press. https://doi.org/10.1017/9781009157964

Intergovernmental Panel on Climate Change (IPCC). (2023). *Climate Change 2021 – The Physical Science Basis: Working Group I Contribution to the Sixth Assessment Report of the Intergovernmental Panel on Climate Change* (1st ed.). Cambridge University Press. https://doi.org/10.1017/9781009157896

Jacobs, S. S., Helmer, H. H., Doake, C. S. M., Jenkins, A., & Frolich, R. M. (1992). Melting of ice shelves and the mass balance of Antarctica. *Journal of Glaciology*, *38*(130), 375–387. https://doi.org/10.3189/S0022143000002252

Jiménez Morales, V., Almendros, J., & Carmona, E. (2017). Detection of long-duration tremors at Deception Island volcano, Antarctica. *Journal of Volcanology and Geothermal Research*, *347*, 234–249. https://doi.org/10.1016/j.jvolgeores.2017.09.016

Jiménez-Morales, V., Almendros, J., & Carmona, E. (2022). Long-Term Evolution of the Seismic Activity Preceding the 2015 Seismic Crisis at Deception Island Volcano, Antarctica (2008-2015). *Surveys in Geophysics*, *43*(3), 959–994. https://doi.org/10.1007/s10712-021-09690-0

Johnson, G. (1998). Deep water properties, velocities, and dynamics over ocean trenches. *Journal of Marine Research*, *56*(2). https://elischolar.library.yale.edu/journal_of_marine_research/2273

Jones, J. M., Gille, S. T., Goosse, H., Abram, N. J., Canziani, P. O., Charman, D. J., Clem, K. R., Crosta, X., de Lavergne, C., Eisenman, I., England, M. H., Fogt, R. L., Frankcombe, L. M., Marshall, G. J., Masson-Delmotte, V., Morrison, A. K., Orsi, A. J., Raphael, M. N., Renwick, J. A., … Vance, T. R. (2016). Assessing recent trends in high-latitude Southern Hemisphere surface climate. *Nature Climate Change*, *6*(10), 917–926. https://doi.org/10.1038/nclimate3103

Joughin, I., & Padman, L. (2003). Melting and freezing beneath Filchner-Ronne Ice Shelf, Antarctica. *Geophysical Research Letters*, *30*(9). https://doi.org/10.1029/2003GL016941

Juteau, T. (2005). LAS DORSALES OCEÁNICAS: VULCANISMO, HIDROTERMALISMO Y YACIMIENTOS DE METALES DE MAÑANA. *DYNA*, *80*(9), Article 9. https://revista-dyna.com/index.php/DYNA/article/view/5952

Kadri, U., & Akylas, T. R. (2016). On resonant triad interactions of acoustic–gravity waves. *Journal of Fluid Mechanics*, *788*, R1. https://doi.org/10.1017/jfm.2015.721

Kasahara, A. (1977). Numerical Integration of the Global Barotropic Primitive Equations with Hough Harmonic Expansions. *Journal of the Atmospheric Sciences*, *34*(5), 687–701. https://doi.org/10.1175/1520-0469(1977)034<0687:NIOTGB>2.0.CO;2

Kataoka, R., Winn, S. D., & Touber, E. (2022). Meteotsunamis in Japan Associated with the Tonga Eruption in January 2022. *SOLA*, *18*(0), 116–121. https://doi.org/10.2151/sola.2022-019

Khaleghian, S., Ullah, H., Kræmer, T., Hughes, N., Eltoft, T., & Marinoni, A. (2021). Sea Ice Classification of SAR Imagery Based on Convolution Neural Networks. *Remote Sensing*, *13*(9), 1734. https://doi.org/10.3390/rs13091734

Kim, M. S., & Woo, S. B. (2021). Propagation and amplification of meteotsunamis in multiple harbors along the eastern Yellow Sea coast. *Continental Shelf Research*, *225*, 104474. https://doi.org/10.1016/j.csr.2021.104474

Kim, M. S., Woo, S. B., Eom, H., & You, S. H. (2021). Occurrence of pressure-forced meteotsunami events in the eastern Yellow Sea during 2010–2019. *Natural Hazards and Earth System Sciences*, *21*(11), 3323–3337. https://doi.org/10.5194/nhess-21-3323-2021

Klinck, J. M. (1998). Heat and salt changes on the continental shelf west of the Antarctic Peninsula between January 1993 and January 1994. *Journal of Geophysical Research: Oceans*, *103*(C4), 7617–7636. https://doi.org/10.1029/98JC00369

Kolbusz, J., Zika, J., Pattiaratchi, C., & Jamieson, A. (2024). Water properties and bottom water patterns in hadal trench environments. *Ocean Science*, *20*(1), 123–140. https://doi.org/10.5194/os-20-123-2024

Koutitas, C. G. (1988). *Mathematical models in coastal engineering*. Pentech Press.

Kubo, H., Kubota, T., Suzuki, W., Aoi, S., Sandanbata, O., Chikasada, N., & Ueda, H. (2022). Ocean-wave phenomenon around Japan due to the 2022 Tonga eruption observed by the wide and dense ocean-bottom pressure gauge networks. *Earth, Planets and Space*, *74*(1), 104. https://doi.org/10.1186/s40623-022-01663-w

Lacanna, G., & Ripepe, M. (2013). Influence of near-source volcano topography on the acoustic wavefield and implication for source modeling. *Journal of Volcanology and Geothermal Research*, *250*, 9–18. https://doi.org/10.1016/j.jvolgeores.2012.10.005

Laignel, B., Vignudelli, S., Almar, R., Becker, M., Bentamy, A., Benveniste, J., Birol, F., Frappart, F., Idier, D., Salameh, E., Passaro, M., Menende, M., Simard, M., Turki, E. I., & Verpoorter, C. (2023). Observation of the Coastal Areas, Estuaries and Deltas

from Space. *Surveys in Geophysics*, *44*(5), 1309–1356. https://doi.org/10.1007/s10712-022-09757-6

Lamb, H. (1932). *Hydrodynamics* (6th ed.). Cambridge University Press.

Latter, J. H. (1981). Tsunamis of volcanic origin: Summary of causes, with particular reference to Krakatoa, 1883. *Bulletin Volcanologique*, *44*(3), 467–490. https://doi.org/10.1007/BF02600578

Lawrence, I. R., Armitage, T. W. K., Tsamados, M. C., Stroeve, J. C., Dinardo, S., Ridout, A. L., Muir, A., Tilling, R. L., & Shepherd, A. (2021). Extending the Arctic sea ice freeboard and sea level record with the Sentinel-3 radar altimeters. *Advances in Space Research*, *68*(2), 711–723. https://doi.org/10.1016/j.asr.2019.10.011

Lawrence, L. A., Sloan, B. J., & Barker, D. H. N. (1997). Distributed, active extension in Bransfield Basin, Antarctic Peninsula: Evidence from multibeam bathymetry. *Oceanographic Literature Review*, *8*(44), 840. https://www.infona.pl//resource/bwmeta1.element.elsevier-65b146ac-1108-3299-9181-a7695cf16ce5

LEGOS/CNRS/CLS. (1992). *Dynamic Atmospheric Correction* [NetCDF]. CNES. https://doi.org/10.24400/527896/A01-2022.001

Lei, J., Li, F., Zhang, S., Xiao, C., Xie, S., Ke, H., Zhang, Q., & Li, W. (2018). Ocean Tides Observed from A GPS Receiver on Floating Sea Ice Near Chinese Zhongshan Station, Antarctica. *Marine Geodesy*, *41*(4), 353–367. https://doi.org/10.1080/01490419.2018.1454370

Lenn, Y.-D., Chereskin, T. K., & Glatts, R. C. (2003). Seasonal to tidal variability in currents, stratification and acoustic backscatter in an Antarctic ecosystem at Deception Island. *Deep Sea Research Part II: Topical Studies in Oceanography*, *50*(10–11), 1665–1683. https://doi.org/10.1016/S0967-0645(03)00085-7

Leuliette, E., Nerem, R. S., & Mitchum, G. T. (2004). Calibration of TOPEX/Poseidon and Jason Altimeter Data to Construct a Continuous Record of Mean Sea Level Change. *Marine Geodesy*, *27*(1–2), 79–94. https://doi.org/10.1080/01490410490465193

Liner, C. (2010). *An overview of wavelet transform concepts and applications*. https://www.semanticscholar.org/paper/An-overview-of-wavelet-transform-concepts-and-Liner/52372db16936b0188f5257b80ef5804fff96c411

Lohse, J., Doulgeris, A. P., & Dierking, W. (2021). Incident Angle Dependence of Sentinel-1 Texture Features for Sea Ice Classification. *Remote Sensing*, *13*(4), 552. https://doi.org/10.3390/rs13040552

López, O., García, M. A., & S. -Arcilla, A. (1994). Tidal and residual currents in the Bransfield Strait, Antarctica. *Annales Geophysicae*, *12*(9), 887–902. https://doi.org/10.1007/s00585-994-0887-5

López, O., García, M. A., Gomis, D., Rojas, P., Sospedra, J., & Sánchez-Arcilla, A. (1999). Hydrographic and hydrodynamic characteristics of the eastern basin of the Bransfield Strait (Antarctica). *Deep Sea Research Part I: Oceanographic Research Papers*, *46*(10), 1755–1778. https://doi.org/10.1016/s0967-0637(99)00017-5

Lyard, F. H., Allain, D. J., Cancet, M., Carrère, L., & Picot, N. (2021). FES2014 global ocean tide atlas: Design and performance. *Ocean Science*, *17*(3), 615–649. https://doi.org/10.5194/os-17-615-2021

Mahoney, A. R., Gough, A. J., Langhorne, P. J., Robinson, N. J., Stevens, C. L., Williams, M. M. J., & Haskell, T. G. (2011). The seasonal appearance of ice shelf water in coastal Antarctica and its effect on sea ice growth. *Journal of Geophysical Research: Oceans*, *116*(C11), 2011JC007060. https://doi.org/10.1029/2011JC007060

Marcos, M., Monserrat, S., Medina, R., Orfila, A., & Olabarrieta, M. (2009). External forcing of meteorological tsunamis at the coast of the Balearic Islands. *Physics and*

Chemistry of the Earth, Parts A/B/C, *34*(17–18), 938–947. https://doi.org/10.1016/j.pce.2009.10.001

Martí, J., Geyer, A., & Aguirre-Diaz, G. (2013). Origin and evolution of the Deception Island caldera (South Shetland Islands, Antarctica). *Bulletin of Volcanology*, *75*(6). https://doi.org/10.1007/s00445-013-0732-3

Martín, R. (2021). *Benthic marine algae from South Shetland Islands (Antarctica): Biodiversity and evolutionary patterns* [Bacelona University]. https://diposit.ub.edu/dspace/handle/2445/184229

Matoza, R. S., Fee, D., Assink, J. D., Iezzi, A. M., Green, D. N., Kim, K., Toney, L., Lecocq, T., Krishnamoorthy, S., Lalande, J.-M., Nishida, K., Gee, K. L., Haney, M. M., Ortiz, H. D., Brissaud, Q., Martire, L., Rolland, L., Vergados, P., Nippress, A., … Wilson, D. C. (2022). Atmospheric waves and global seismoacoustic observations of the January 2022 Hunga eruption, Tonga. *Science*, *377*(6601), 95–100. https://doi.org/10.1126/science.abo7063

Meloni, M., Bouffard, J., Doglioli, A. M., Petrenko, A. A., & Valladeau, G. (2019). Toward science-oriented validations of coastal altimetry: Application to the Ligurian Sea. *Remote Sensing of Environment*, *224*, 275–288. https://doi.org/10.1016/j.rse.2019.01.028

Meredith, M. P., Brandon, M. A., Wallace, M. I., Clarke, A., Leng, M. J., Renfrew, I. A., Van Lipzig, N. P. M., & King, J. C. (2008). Variability in the freshwater balance of northern Marguerite Bay, Antarctic Peninsula: Results from δ18O. *Deep Sea Research Part II: Topical Studies in Oceanography*, *55*(3–4), 309–322. https://doi.org/10.1016/j.dsr2.2007.11.005

Meredith, M. P., & King, J. C. (2005). Rapid climate change in the ocean west of the Antarctic Peninsula during the second half of the 20th century. *Geophysical Research Letters*, *32*(19), 2005GL024042. https://doi.org/10.1029/2005GL024042

Meyssignac, B., Ablain, M., Guérou, A., Prandi, P., Barnoud, A., Blazquez, A., Fourest, S., Rousseau, V., Bonnefond, P., Cazenave, A., Chenal, J., Dibarboure, G., Donlon, C., Benveniste, J., Sylvestre-Baron, A., & Vinogradova, N. (2023). How accurate is accurate enough for measuring sea-level rise and variability. *Nature Climate Change*, *13*(8), 796–803. https://doi.org/10.1038/s41558-023-01735-z

Monserrat, S., Vilibić, I., & Rabinovich, A. B. (2006). Meteotsunamis: Atmospherically induced destructive ocean waves in the tsunami frequency band. *Natural Hazards and Earth System Sciences*, *6*(6), 1035–1051. https://doi.org/10.5194/nhess-6-1035-2006

Moreno-Vacas, A., & Almendros, J. (2021). On the origin of recent seismic unrest episodes at Deception Island volcano, Antarctica. *Journal of Volcanology and Geothermal Research*, *419*, 107376. https://doi.org/10.1016/j.jvolgeores.2021.107376

Mostafavi, M., Delpeche-Ellmann, N., & Ellmann, A. (2021). Accurate Sea Surface heights from Sentinel-3A and Jason-3 retrackers by incorporating High-Resolution Marine Geoid and Hydrodynamic Models. *Journal of Geodetic Science*, *11*(1), 58–74. https://doi.org/10.1515/jogs-2020-0120

Mugunthan, J. S., Duguay, C. R., & Zakharova, E. (2023). Machine learning based classification of lake ice and open water from Sentinel-3 SAR altimetry waveforms. *Remote Sensing of Environment*, *299*, 113891. https://doi.org/10.1016/j.rse.2023.113891

Nerem, R. S., Beckley, B. D., Fasullo, J. T., Hamlington, B. D., Masters, D., & Mitchum, G. T. (2018). Climate-change–driven accelerated sea-level rise detected in the altimeter

era. *Proceedings of the National Academy of Sciences*, *115*(9), 2022–2025. https://doi.org/10.1073/pnas.1717312115

Nerem, R. S., & Mitchum, G. T. (2001). Chapter 8 Sea Level Change. In L.-L. Fu & A. Cazenave (Eds.), *International Geophysics* (Vol. 69, pp. 329–xxiii). Academic Press. https://doi.org/10.1016/S0074-6142(01)80153-4

Nishida, K., Kobayashi, N., & Fukao, Y. (2014). Background Lamb waves in the Earth's atmosphere. *Geophysical Journal International*, *196*(1), 312–316. https://doi.org/10.1093/gji/ggt413

Niu, X. (2021). Resonance of long waves around a circular island and its relation to edge waves. *European Journal of Mechanics - B/Fluids*, *86*, 15–24. https://doi.org/10.1016/j.euromechflu.2020.11.007

Nomitsu, T. (1935). A theory of tsunamis and seiches produced by wind and barometric gradient. *Memoirs of the College of Science, Kyoto Imperial University. Series A*, *18*, 201–2014.

Oliva, M., Navarro, F., Hrbáček, F., Hernández, A., Nývlt, D., Pereira, P., Ruiz-Fernández, J., & Trigo, R. (2017). Recent regional climate cooling on the Antarctic Peninsula and associated impacts on the cryosphere. *Science of The Total Environment*, *580*, 210–223. https://doi.org/10.1016/j.scitotenv.2016.12.030

Omira, R., Ramalho, R. S., Kim, J., González, P. J., Kadri, U., Miranda, J. M., Carrilho, F., & Baptista, M. A. (2022). Global Tonga tsunami explained by a fast-moving atmospheric source. *Nature*, *609*(7928), 734–740. https://doi.org/10.1038/s41586-022-04926-4

Oreiro, F. A., D'Onofrio, E., Grismeyer, W., Fiore, M., & Saraceno, M. (2014). Comparison of tide model outputs for the northern region of the Antarctic Peninsula using satellite

altimeters and tide gauge data. *Polar Science*, *8*(1), 10–23. https://doi.org/10.1016/j.polar.2013.12.001

Paris, R. (2015). Source mechanisms of volcanic tsunamis. *Philosophical Transactions of the Royal Society A: Mathematical, Physical and Engineering Sciences*, *373*(2053), 20140380. https://doi.org/10.1098/rsta.2014.0380

Passaro, M., Müller, F. L., Oelsmann, J., Rautiainen, L., Dettmering, D., Hart-Davis, M. G., Abulaitijiang, A., Andersen, O. B., Høyer, J. L., Madsen, K. S., Ringgaard, I. M., Särkkä, J., Scarrott, R., Schwatke, C., Seitz, F., Tuomi, L., Restano, M., & Benveniste, J. (2021). Absolute Baltic Sea Level Trends in the Satellite Altimetry Era: A Revisit. *Frontiers in Marine Science*, *8*, 647607. https://doi.org/10.3389/fmars.2021.647607

Pawlowicz, R., Beardsley, B., & Lentz, S. (2002). Classical tidal harmonic analysis including error estimates in MATLAB using T_TIDE. *Computers & Geosciences*, *28*(8), 929–937. https://doi.org/10.1016/s0098-3004(02)00013-4

Peacock, N. R., & Laxon, S. W. (2004). Sea surface height determination in the Arctic Ocean from ERS altimetry. *Journal of Geophysical Research: Oceans*, *109*(C7). https://doi.org/10.1029/2001JC001026

Peng, F., & Deng, X. (2020). Validation of Sentinel-3A SAR mode sea level anomalies around the Australian coastal region. *Remote Sensing of Environment*, *237*, 111548. https://doi.org/10.1016/j.rse.2019.111548

Peng, F., Deng, X., & Shen, Y. (2024). Assessment of Sentinel-6 SAR mode and reprocessed Jason-3 sea level measurements over global coastal oceans. *Remote Sensing of Environment*, *311*, 114287. https://doi.org/10.1016/j.rse.2024.114287

Pérez, L. F., Hernández-Molina, F. J., Lodolo, E., Bohoyo, F., Galindo-Zaldívar, J., & Maldonado, A. (2019). Oceanographic and climatic consequences of the tectonic

evolution of the southern scotia sea basins, Antarctica. *Earth-Science Reviews*, *198*, 102922. https://doi.org/10.1016/j.earscirev.2019.102922

Pham, D. T., Llovel, W., Nguyen, T. M., Le, H. Q., Le, M. N., & Ha, H. T. (2024). Sea-level trends and variability along the coast of Vietnam over 2002–2018: Insights from the X-TRACK/ALES altimetry dataset and coastal tide gauges. *Advances in Space Research*, *73*(3), 1630–1645. https://doi.org/10.1016/j.asr.2023.10.041

Poli, P., Cabrera, L., Flores, M. C., Báez, J. C., Ammirati, J. B., Vásquez, J., & Ruiz, S. (2022). Volcanic Origin of a Long-Lived Swarm in the Central Bransfield Basin, Antarctica. *Geophysical Research Letters*, *49*(1), e2021GL095447. https://doi.org/10.1029/2021GL095447

Polukhin, A. A., Morozov, E. G., Tishchenko, P. P., Frey, D. I., Artemiev, V. A., Borisenko, G. V., Vidnichuk, A. V., Marina, E. N., Medvedev, E. V., Popov, O. S., Seliverstova, A. M., & Chultsova, A. L. (2021). Water Structure in the Bransfield Strait (Antarctica) in January 2020: Hydrophysical, Optical, and Hydrochemical Features. *Oceanology*, *61*(5), 632–644. https://doi.org/10.1134/S0001437021050106

Prandi, P., Ablain, M., Cazenave, A., & Picot, N. (2012). A New Estimation of Mean Sea Level in the Arctic Ocean from Satellite Altimetry. *Marine Geodesy*, *35*(sup1), 61–81. https://doi.org/10.1080/01490419.2012.718222

Proudman, J. (1929). The Effects on the Sea of Changes in Atmospheric Pressure. *Geophysical Journal International*, *2*, 197–209. https://doi.org/10.1111/j.1365-246X.1929.tb05408.x

Pugh, D. T. (1987). *Tides, surges and mean sea level*. Wiley.

Purich, A., & England, M. H. (2023). Projected Impacts of Antarctic Meltwater Anomalies over the Twenty-First Century. *Journal of Climate*, *36*(8), 2703–2719. https://doi.org/10.1175/JCLI-D-22-0457.1

Purich, A., England, M. H., Cai, W., Sullivan, A., & Durack, P. J. (2018). Impacts of Broad-Scale Surface Freshening of the Southern Ocean in a Coupled Climate Model. *Journal of Climate*, *31*(7), 2613–2632. https://doi.org/10.1175/JCLI-D-17-0092.1

Pytharouli, S., Chaikalis, S., & Stiros, S. C. (2018). Uncertainty and bias in electronic tide-gauge records: Evidence from collocated sensors. *Measurement*, *125*, 496–508. https://doi.org/10.1016/j.measurement.2018.05.012

Rabinovich, A. B. (2009). Seiches and Harbor Oscillations. In Y. C. Kim, *Handbook of Coastal and Ocean Engineering* (pp. 193–236). WORLD SCIENTIFIC. https://doi.org/10.1142/9789812819307_0009

Rabinovich, A. B., & Monserrat, S. (1998). *Generation of Meteorological Tsunamis (Large Amplitude Seiches) Near the Balearic and Kuril Islands*.

Ramírez, M. E. (2007). *Modelización de la deformación superficial en áreas volcánicas mediante la teoría de wavelets. Aplicación al volcán decepción.* [Universidad de Cádiz]. University of Cádiz https://dialnet.unirioja.es/servlet/tesis?codigo=51985

Ramírez-Herrera, M. T., Coca, O., & Vargas-Espinosa, V. (2022). Tsunami Effects on the Coast of Mexico by the Hunga Tonga-Hunga Ha'apai Volcano Eruption, Tonga. *Pure and Applied Geophysics*, *179*(4), 1117–1137. https://doi.org/10.1007/s00024-022-03017-9

Ray, C., Martin-Puig, C., Clarizia, M. P., Ruffini, G., Dinardo, S., Gommenginger, C., & Benveniste, J. (2015). SAR Altimeter Backscattered Waveform Model. *IEEE Transactions on Geoscience and Remote Sensing*, *53*(2), 911–919. https://doi.org/10.1109/TGRS.2014.2330423

Ray, R. D., Larson, K. M., & Haines, B. J. (2021). New determinations of tides on the north-western Ross Ice Shelf. *Antarctic Science*, *33*(1), 89–102. https://doi.org/10.1017/s0954102020000498

Ray, R. D., Widlansky, M. J., Genz, A. S., & Thompson, P. R. (2023). Offsets in tide-gauge reference levels detected by satellite altimetry: Ten case studies. *Journal of Geodesy*, *97*(12), 1–17. https://doi.org/10.1007/s00190-023-01800-7

Recondo, C., Corbea-Pérez, A., Peón, J., Pendás, E., Ramos, M., Calleja, J. F., De Pablo, M. Á., Fernández, S., & Corrales, J. A. (2022). Empirical Models for Estimating Air Temperature Using MODIS Land Surface Temperature (and Spatiotemporal Variables) in the Hurd Peninsula of Livingston Island, Antarctica, between 2000 and 2016. *Remote Sensing*, *14*(13), 3206. https://doi.org/10.3390/rs14133206

Ren, Z., Higuera, P., & Li-Fan Liu, P. (2023). On Tsunami Waves Induced by Atmospheric Pressure Shock Waves After the 2022 Hunga Tonga-Hunga Ha'apai Volcano Eruption. *Journal of Geophysical Research: Oceans*, *128*(4), e2022JC019166. https://doi.org/10.1029/2022JC019166

Ribeiro, N., Herraiz-Borreguero, L., Rintoul, S. R., McMahon, C. R., Hindell, M., Harcourt, R., & Williams, G. (2021). Warm Modified Circumpolar Deep Water Intrusions Drive Ice Shelf Melt and Inhibit Dense Shelf Water Formation in Vincennes Bay, East Antarctica. *Journal of Geophysical Research: Oceans*, *126*(8), e2020JC016998. https://doi.org/10.1029/2020JC016998

Rieu, P., Moreau, T., Cadier, E., Raynal, M., Clerc, S., Donlon, C., Borde, F., Boy, F., & Maraldi, C. (2021). Exploiting the Sentinel-3 tandem phase dataset and azimuth oversampling to better characterize the sensitivity of SAR altimeter sea surface height to long ocean waves. *Advances in Space Research*, *67*(1), 253–265. https://doi.org/10.1016/j.asr.2020.09.037

Rodrigo, C., Blamey, J. M., Huhn, O., & Provost, C. (2018). Is there an active hydrothermal flux from the Orca seamount in the Bransfield Strait, Antarctica? *Andean Geology*, *45*(3), 344. https://doi.org/10.5027/andgeoV45n3-3086

Rosado, B., Fernández-Ros, A., Berrocoso, M., Prates, G., Gárate, J., De Gil, A., & Geyer, A. (2019). Volcano-tectonic dynamics of Deception Island (Antarctica): 27 years of GPS observations (1991–2018). *Journal of Volcanology and Geothermal Research*, *381*, 57–82. https://doi.org/10.1016/j.jvolgeores.2019.05.009

Rosado, B., Pérez-Peña, A., Barba, P., Ramírez-Zelaya, J., Carmona, E., Martín, R., Jiménez, V., Gárate, J., de Gil, A., & Berrocoso, M. (2023). Analysis of GNSS Time Series Recorded on South Shetland Island and Antarctic Peninsula during the Geodynamic Activity in 2020 of the Orca Underwater Volcano (Brandfield Sea Rift, Antarctica). *Engineering Proceedings*, *39*(1), Article 1. https://doi.org/10.3390/engproc2023039025

Rose, S., Andersen, O., Passaro, M., Ludwigsen, C., & Schwatke, C. (2019). Arctic Ocean Sea Level Record from the Complete Radar Altimetry Era: 1991–2018. *Remote Sensing*, *11*(14), 1672. https://doi.org/10.3390/rs11141672

Rye, C. D., Naveira Garabato, A. C., Holland, P. R., Meredith, M. P., George Nurser, A. J., Hughes, C. W., Coward, A. C., & Webb, D. J. (2014). Rapid sea-level rise along the Antarctic margins in response to increased glacial discharge. *Nature Geoscience*, *7*(10), 732–735. https://doi.org/10.1038/ngeo2230

Saito, T., Kubota, T., Chikasada, N. Y., Tanaka, Y., & Sandanbata, O. (2021). Meteorological Tsunami Generation Due to Sea-Surface Pressure Change: Three-Dimensional Theory and Synthetics of Ocean-Bottom Pressure Change. *Journal of Geophysical Research: Oceans*, *126*(5). https://doi.org/10.1029/2020JC017011

Sanchez-Vazquez, M. J., Nielen, M., Gunn, G. J., & Lewis, F. I. (2012). Using seasonal-trend decomposition based on loess (STL) to explore temporal patterns of pneumonic lesions in finishing pigs slaughtered in England, 2005–2011. *Preventive Veterinary Medicine*, *104*(1–2), 65–73. https://doi.org/10.1016/j.prevetmed.2011.11.003

Sangrà, P., Gordo, C., Hernández-Arencibia, M., Marrero-Díaz, A., Rodríguez-Santana, A., Stegner, A., Martínez-Marrero, A., Pelegrí, J. L., & Pichon, T. (2011). The Bransfield current system. *Deep Sea Research Part I: Oceanographic Research Papers*, *58*(4), 390–402. https://doi.org/10.1016/j.dsr.2011.01.011

Sangrà, P., Stegner, A., Hernández-Arencibia, M., Marrero-Díaz, Á., Salinas, C., Aguiar-González, B., Henríquez-Pastene, C., & Mouriño-Carballido, B. (2017). The Bransfield Gravity Current. *Deep Sea Research Part I: Oceanographic Research Papers*, *119*, 1–15. https://doi.org/10.1016/j.dsr.2016.11.003

Satake, K., Heidarzadeh, M., Quiroz, M., & Cienfuegos, R. (2020). History and features of trans-oceanic tsunamis and implications for paleo-tsunami studies. *Earth-Science Reviews*, *202*, 103112. https://doi.org/10.1016/j.earscirev.2020.103112

Schellart, W. P., Lister, G. S., & Toy, V. G. (2006). A Late Cretaceous and Cenozoic reconstruction of the Southwest Pacific region: Tectonics controlled by subduction and slab rollback processes. *Earth-Science Reviews*, *76*(3–4), 191–233. https://doi.org/10.1016/j.earscirev.2006.01.002

Seliverstova, A. M., Zuev, O. A., Polukhin, A. A., Chultsova, A. L., Masevich, A. V., & Mukhametianov, R. Z. (2023). Hydrological and Hydrochemical Structure of the Waters of the Bransfield Strait in January 2022. *Oceanology*, *63*(4), 510–522. https://doi.org/10.1134/S0001437023040161

Shaheen, B., Haggag, G., & Saleh, S. (2024). Comparison between Microwave Radar Gauge and Pressure Gauge in Monitoring Sea Level Surface at Alexandria Naval Port. *Fayoum University Journal of Engineering*, *7*(2), 1–9. https://doi.org/10.21608/fuje.2024.343757

Shu, S., Liu, H., Beck, R. A., Frappart, F., Korhonen, J., Xu, M., Yang, B., Hinkel, K. M., Huang, Y., & Yu, B. (2020). Analysis of Sentinel-3 SAR altimetry waveform

retracking algorithms for deriving temporally consistent water levels over ice-covered lakes. *Remote Sensing of Environment*, *239*, 111643. https://doi.org/10.1016/j.rse.2020.111643

Smellie, J. L. (2001). Lithostratigraphy and volcanic evolution of Deception Island, South Shetland Islands. *Antarctic Science*, *13*(2), 188–209. https://doi.org/10.1017/S0954102001000281

Smellie, J. L., Baker, P. E., & Thomson, J. W. (1990). D. Graham Land and South Shetland Islands. In W. E. LeMasurier, J. W. Thomson, P. E. Baker, P. R. Kyle, P. D. Rowley, J. L. Smellie, & W. J. Verwoerd (Eds.), *Antarctic Research Series* (Vol. 48, pp. 302–359). American Geophysical Union. https://doi.org/10.1029/AR048p0302

Smith, K. L., Baldwin, R. J., Glatts, R. C., Chereskin, T. K., Ruhl, H., & Lagun, V. (2003). Weather, ice, and snow conditions at Deception Island, Antarctica: Long time-series photographic monitoring. *Deep Sea Research Part II: Topical Studies in Oceanography*, *50*(10–11), 1649–1664. https://doi.org/10.1016/S0967-0645(03)00084-5

Smith, R. I. L. (2005). The thermophilic bryoflora of Deception Island: Unique plant communities as a criterion for designating an Antarctic Specially Protected Area. *Antarctic Science*, *17*(1), 17–27. https://doi.org/10.1017/S0954102005002385

Soltanpour, A., Pirooznia, M., Aminjafari, S., & Zareian, P. (2018). Persian gulf and Oman sea tide modeling using satellite altimetry and tide gauge data (TM-IR01). *Marine Georesources & Geotechnology*, *36*(6), 677–687. https://doi.org/10.1080/1064119X.2017.1366608

Steig, E. J., Schneider, D. P., Rutherford, S. D., Mann, M. E., Comiso, J. C., & Shindell, D. T. (2009). Warming of the Antarctic ice-sheet surface since the 1957 International

Geophysical Year. *Nature*, *457*(7228), 459–462. https://doi.org/10.1038/nature07669

Stewart, C., Horgan, H., & Stevens, C. (2023). Short Note: 2022 Hunga Tonga-Hunga Ha'apai tsunami measured beneath the Ross Ice Shelf. *Antarctic Science*, *36*(3), 181–183. https://doi.org/10.1017/S0954102023000366

Sugiyama, S., Navarro, F. J., Sawagaki, T., Minowa, M., Segawa, T., Onuma, Y., Otero, J., & Vasilenko, E. V. (2019). Subglacial water pressure and ice-speed variations at Johnsons Glacier, Livingston Island, Antarctic Peninsula. *Journal of Glaciology*, *65*(252), 689–699. https://doi.org/10.1017/jog.2019.45

Tahira, M., Nomura, M., Sawada, Y., & Kamo, K. (1996). Infrasonic and acoustic-gravity waves generated by the Mount Pinatubo eruption of June 15, 1991. In *Fire and Mud: Eruptions and Lahars of Mount Pinatubo, Philippines* (pp. 601–614). Philippine Institute of Volcanology and Seismology & University of Washington Press.

Tang, F., Chen, P., An, Z., Xiong, M., Chen, H., & Qiu, L. (2023). A Dual-Threshold Algorithm for Ice-Covered Lake Water Level Retrieval Using Sentinel-3 SAR Altimetry Waveforms. *Sensors*, *23*(24), 9724. https://doi.org/10.3390/s23249724

The IMBIE team. (2018). Mass balance of the Antarctic Ice Sheet from 1992 to 2017. *Nature*, *558*(7709), 219–222. https://doi.org/10.1038/s41586-018-0179-y

Tokarczyk, R. (1987). Classification of water masses in the Bransfield Strait and southern part of the Drake Passage using a method of statistical multidimensional analysis. *Polish Polar Research; 1987; Vol. 8; No 4; 333-366*. https://www.czasopisma.pan.pl/dlibra/publication/127654/edition/111384

Tonegawa, T., & Fukao, Y. (2022). Wave propagation of meteotsunamis and generation of free tsunamis in the sloping area of the Japan Trench for the 2022 Hunga–Tonga

volcanic eruption. *Earth, Planets and Space*, *74*(1), 159. https://doi.org/10.1186/s40623-022-01727-x

Trisirisatayawong, I., Naeije, M., Simons, W., & Fenoglio-Marc, L. (2011). Sea level change in the Gulf of Thailand from GPS-corrected tide gauge data and multi-satellite altimetry. *Global and Planetary Change*, *76*(3–4), 137–151. https://doi.org/10.1016/j.gloplacha.2010.12.010

Truffer, M., & Motyka, R. J. (2016). Where glaciers meet water: Subaqueous melt and its relevance to glaciers in various settings. *Reviews of Geophysics*, *54*(1), 220–239. https://doi.org/10.1002/2015RG000494

Turner, J., Colwell, S. R., Marshall, G. J., Lachlan-Cope, T. A., Carleton, A. M., Jones, P. D., Lagun, V., Reid, P. A., & Iagovkina, S. (2005). Antarctic climate change during the last 50 years. *International Journal of Climatology*, *25*(3), 279–294. https://doi.org/10.1002/joc.1130

Turner, J., Lu, H., King, J., Marshall, G. J., Phillips, T., Bannister, D., & Colwell, S. (2021). Extreme Temperatures in the Antarctic. *Journal of Climate*, *34*(7), 2653–2668. https://doi.org/10.1175/JCLI-D-20-0538.1

Turner, J., Marshall, G. J., Clem, K., Colwell, S., Phillips, T., & Lu, H. (2020). Antarctic temperature variability and change from station data. *International Journal of Climatology*, *40*(6), 2986–3007. https://doi.org/10.1002/joc.6378

UHSLC Legacy Data Portal. (n.d.). Retrieved 1 May 2023, from https://uhslc.soest.hawaii.edu/data/?rq#uh832

United States Geological Survey (USGS). (2022). *M 5.8 Volcanic Eruption—68 km NNW of Nuku'alofa, Tonga*. USGS Earthquake Hazards Program – Latest Earthquakes. https://earthquake.usgs.gov/earthquakes/eventpage/us7000gc8r/executive

Universidad de Cádiz, & Berrocoso Domínguez, M. (2024). *GEO2OCEAN: Seawater temperature and sea level pressure at Deception Island* [Dataset]. Spanish Polar Data Centre. https://doi.org/10.57724/GDC_20160101_GEO2OCEAN_ST

Valle-Rodríguez, J., Gómez-Enri, J., & Trasviña-Castro, A. (2023). Assessment and exploitation of coastal low resolution mode sea level data from CryoSat-2 on the entrance to the Gulf of California. *Advances in Space Research*, *72*(10), 4336–4349. https://doi.org/10.1016/j.asr.2023.08.048

Vaughan, D. G., Marshall, G. J., Connolley, W. M., Parkinson, C., Mulvaney, R., Hodgson, D. A., King, J. C., Pudsey, C. J., & Turner, J. (2003). Recent Rapid Regional Climate Warming on the Antarctic Peninsula. *Climatic Change*, *60*(3), 243–274. https://doi.org/10.1023/A:1026021217991

Venables, H., Meredith, M. P., Hendry, K. R., Ten Hoopen, P., Peat, H., Chapman, A., Beaumont, J., Piper, R., Miller, A. J., Mann, P., Rossetti, H., Massey, A., Souster, T., Reeves, S., Fenton, M., Heiser, S., Pountney, S., Reed, S., Waring, Z., … Clarke, A. (2023). Sustained year-round oceanographic measurements from Rothera Research Station, Antarctica, 1997–2017. *Scientific Data*, *10*(1), 265. https://doi.org/10.1038/s41597-023-02172-5

Veny, M., Aguiar-González, B., Marrero-Díaz, Á., & Rodríguez-Santana, Á. (2022). Seasonal circulation and volume transport of the Bransfield Current. *Progress in Oceanography*, *204*, 102795. https://doi.org/10.1016/j.pocean.2022.102795

Vidal, J., Berrocoso, M., & Fernández-Ros, A. (2012). Study of tides and sea levels at Deception and Livingston islands, Antarctica. *Antarctic Science*, *24*(2), 193–201. https://doi.org/10.1017/S095410201100068X

Vignudelli, S. (Ed.). (2011). *Coastal altimetry*. Springer.

Vignudelli, S., Birol, F., Benveniste, J., Fu, L.-L., Picot, N., Raynal, M., & Roinard, H. (2019). Satellite Altimetry Measurements of Sea Level in the Coastal Zone. *Surveys in Geophysics*, *40*(6), 1319–1349. https://doi.org/10.1007/s10712-019-09569-1

Vilibić, I. (2008). Numerical simulations of the Proudman resonance. *Continental Shelf Research*, *28*(4–5), 574–581. https://doi.org/10.1016/j.csr.2007.11.005

Vorrath, M.-E., Müller, J., Rebolledo, L., Cárdenas, P., Shi, X., Esper, O., Opel, T., Geibert, W., Muñoz, P., Haas, C., Kuhn, G., Lange, C. B., Lohmann, G., & Mollenhauer, G. (2020). Sea ice dynamics in the Bransfield Strait, Antarctic Peninsula, during the past 240 years: A multi-proxy intercomparison study. *Climate of the Past*, *16*(6), 2459–2483. https://doi.org/10.5194/cp-16-2459-2020

Wang, Y., Wang, P., Kong, H., & Wong, C.-S. (2022). Tsunamis in Lingding Bay, China, caused by the 2022 Tonga volcanic eruption. *Geophysical Journal International*, *232*(3), 2175–2185. https://doi.org/10.1093/gji/ggac291

WCRP Global Sea Level Budget Group. (2018). Global sea-level budget 1993–present. *Earth System Science Data*, *10*(3), 1551–1590. https://doi.org/10.5194/essd-10-1551-2018

Yamada, M., Ho, T., Mori, J., Nishikawa, Y., & Yamamoto, M. (2022). Tsunami Triggered by the Lamb Wave From the 2022 Tonga Volcanic Eruption and Transition in the Offshore Japan Region. *Geophysical Research Letters*, *49*(15), e2022GL098752. https://doi.org/10.1029/2022GL098752

Yang, J., Zhang, J., & Wang, C. (2019). Sentinel-3A SRAL Global Statistical Assessment and Cross-Calibration with Jason-3. *Remote Sensing*, *11*(13), 1573. https://doi.org/10.3390/rs11131573

Zakhvatkina, N., Smirnov, V., & Bychkova, I. (2019). Satellite SAR Data-based Sea Ice Classification: An Overview. *Geosciences*, *9*(4), 152. https://doi.org/10.3390/geosciences9040152

Zhao, J., Zhang, Z., Yao, W., Datcu, M., Xiong, H., & Yu, W. (2020). OpenSARUrban: A Sentinel-1 SAR Image Dataset for Urban Interpretation. *IEEE Journal of Selected Topics in Applied Earth Observations and Remote Sensing*, *13*, 187–203. https://doi.org/10.1109/JSTARS.2019.2954850

Zhou, X., Zhu, G., & Hu, S. (2020). Influence of tides on mass transport in the Bransfield Strait and the adjacent areas, Antarctic. *Polar Science*, *23*, 100506. https://doi.org/10.1016/j.polar.2020.100506

APPENDIXES

Appendix I

Complementary analyses to Chapter 5

Statement of the appendix

This appendix presents additional work carried out during the course of the thesis that has contributed to identifying areas for methodological improvement and possible future research. Among these efforts is the attempt to reference tide gauge records to the ellipsoid, with the aim of enabling absolute comparisons between sea level series of DECMAR and LIVMAR and with Sentinel-3A/B altimetry. This approach proved challenging due to inconsistencies in levelling data and discontinuities in some of the campaigns. However, despite several methodological tests, consistent ellipsoidal referencing could not be achieved, and the procedures presented here should be regarded as exploratory.

Further tests were also conducted during a research stay at the National Research Council of Italy (CNR-ISP, Mestre, Venice). In addition, sea level anomalies (SLAs) were calculated using data from alternative sources, such as the Earth Console Parallel Processing Service (P-PRO, https://ui-ppro.earthconsole.eu/), provided by the European Space Agency (ESA).

Georeferencing of sea level records

- **Standard methodology**

In order to compare tide observations recorded at different locations, it is necessary to reference the data, whenever possible, to a common and permanent datum. This enables the identification and analysis of potential spatial variations. Moreover, when tide observations obtained during different campaigns are related to such permanent references, it becomes possible to investigate long-term variations in mean sea level (Vidal et al., 2012).

Before undertaking the relative analysis of sea level series, as presented in Chapter 5, several tests were carried out to reference them to the GRS80 ellipsoid. However, the methodologies applied did not yield satisfactory results. Some examples of the work carried out are presented below.

The first step is the deployment of the pressure sensors approximately 50 m from the coast at low tide, where they remain for one year (Ps1 and Ps2). Once deployed, topographic referencing is carried out on the coast. First, a measurement of the auxiliary benchmark is taken using a level and a ruler (A in **Figure I.1**). Then, a ruler with a pressure sensor attached to its lower end (Auxiliary Ps) is placed at the shoreline at a depth of 0.5 m, and the distance between the level and the ruler is measured (B in **Figure I.1**). In order to reference the

recorded sea level measurements to the auxiliary benchmark, the following operations were performed:

$$h_2 = A - B \quad \text{(I. 1)}$$

$$F = h_2 - (D' + 0.1) \quad \text{(I. 2)}$$

$$X = D + F + \Delta n \quad \text{(I. 3)}$$

$$M = h - X \quad \text{(I. 4)}$$

$$K = D + M \quad \text{(I. 5)}$$

where D′ is the measurement provided by the pressure sensor placed on the ruler, and h_2 is the position of the sensor relative to the Tide Gauge Benchmark (TGBM). The constant value of 0.10 m accounts for the fact that the pressure sensor is positioned 10 cm above the seabed to prevent damage. F represents the levelling connection between the Auxiliary Ps and the TGBM, while X is the sum of D, F, and Δn, the distance between the TGBM and the GPS station. Finally, K corresponds to sea level referred to the ellipsoid. GRS80 was chosen as the reference ellipsoid for the final records (**Figure I.1**).

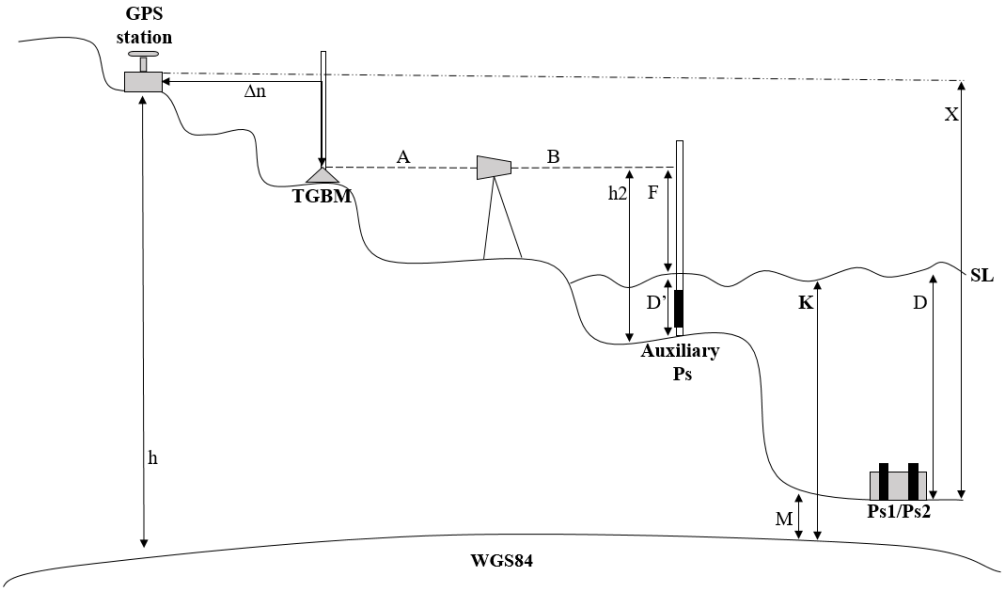


Figure I.1 Levelling scheme between pressure sensors (Ps1, Ps2 and Auxiliary Ps), Tide Gauge Benchmark (TGBM) and the GPS station. D and D' are the measurements of the pressure sensors; Δn the distance between the TGBM and the GPS station; F is the measure between the Auxiliary Ps and the TGBM, and X is the sum of D, F and Δn. K is the sea level to the ellipsoid. GRS80 is the reference ellipsoid chosen to reference the final records.

To obtain the sea level with respect to the reference ellipsoid, the first step is to determine the ellipsoidal height (h in **Figure I.1** and **Figure I.2**) of the auxiliary benchmark selected for the instantaneous tide referencing. This value is calculated from the ellipsoidal height derived from GPS observations at the corresponding TGBM vertex. A local approximation between both points is considered, leading to the following expressions:

$$h \approx H + N \tag{I. 6}$$

$$h' \approx h - \Delta n \tag{I. 7}$$

where h is the known ellipsoidal height, h' the unknown ellipsoidal height to be determined, N the geoid undulation, and Δn the height difference (see **Figure I.2**).

The orthometric heights (H) are calculated as a function of the height difference and gravity. Assuming constant gravity due to the proximity of the points, the height difference between the TGBM can be expressed as:

$$\Delta n \approx H - H' \tag{I. 8}$$

The ellipsoidal height of mean sea level is then obtained from the ellipsoidal height of the reference point (TGBM) and the observed height differences. Thus, the ellipsoidal height of mean sea level corresponds to the ellipsoidal height of the reference point minus the observed height differences between that point and mean sea level.

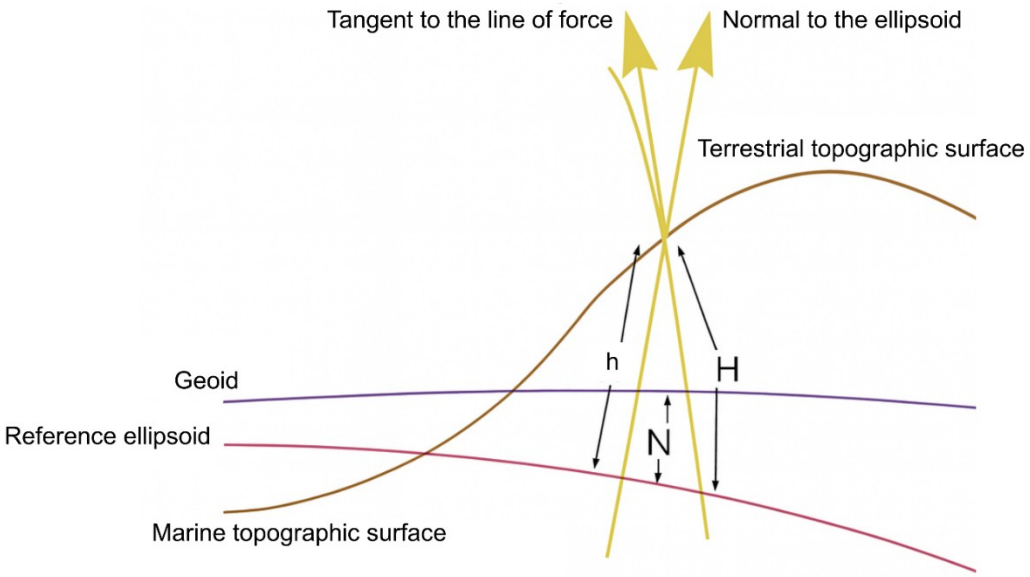


Figure I.2 Terrestrial representation surfaces. H represents orthometric height, h represents ellipsoidal height, and N represents the undulation of the geoid.

The results of the referencing for the LIVMAR station are shown below (**Figure I.3**). This station is characterised by the fact that, in most years, only one levelling measurement is available, or at most two: one when the tide gauges are deployed and another prior to their removal. In some years, the tide gauge required longer to stabilise, resulting in the levelling not coinciding with the record from the deployed sensor. As shown in the figure, there is no continuity in the series; moreover, in those years with two measurements, they do not coincide. Therefore, although the source of the inconsistency remains unknown, this methodology is disregarded.

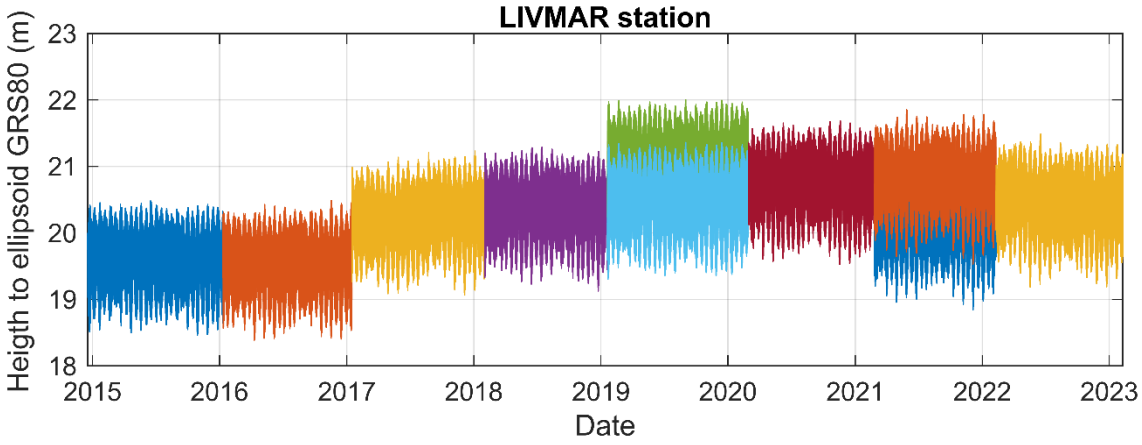


Figure I.3 Sea level records referenced to the GR80 ellipsoid. Each colour represents a different year. The years that appear twice are due to the record being referenced twice, as several measurements were taken of the ellipsoid.

Alternative tests carried out at CNR-ISP

During the research stay at the CNR-ISP, two approaches were tested to reference the sea level series from the LIVMAR station, since some of the records could not be directly tied to the GRS80 ellipsoid.

- **Test A - Referencing through interannual predictions**

The first approach was based on referencing the 2015 record to the ellipsoid, after which subsequent annual series were linked using interannual predictions (**Figure I.4**). These predictions served as the common reference point for merging the records up to 2023, the last year with available data during the research stay.

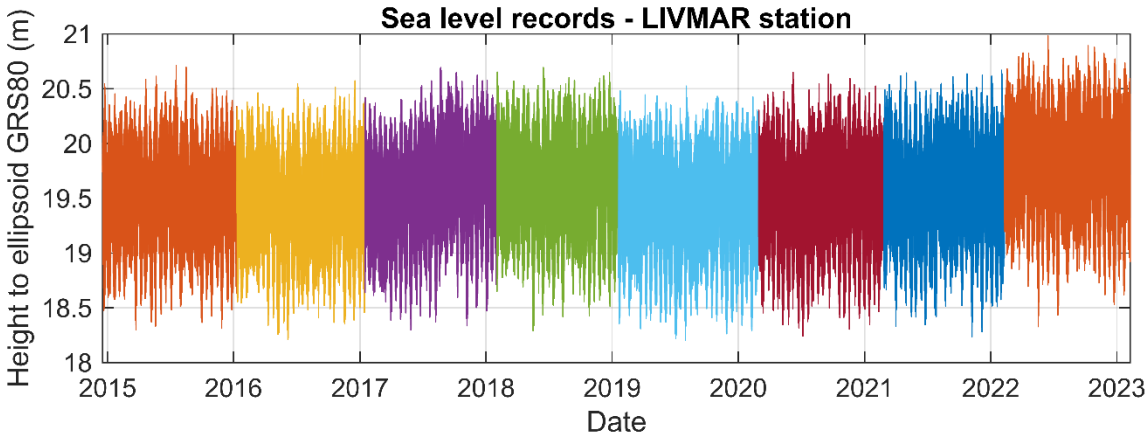


Figure I.4 Sea level series from the tide gauge referenced to the GRS80 ellipsoid. Each colour identifies an annual series.

The resulting Sea Surface Height (SSH), however, was not satisfactory: the series appeared displaced and exhibited an unrealistic long-term trend (**Figure I.5**). As the cause of this behaviour could not be identified, this methodology was discarded.

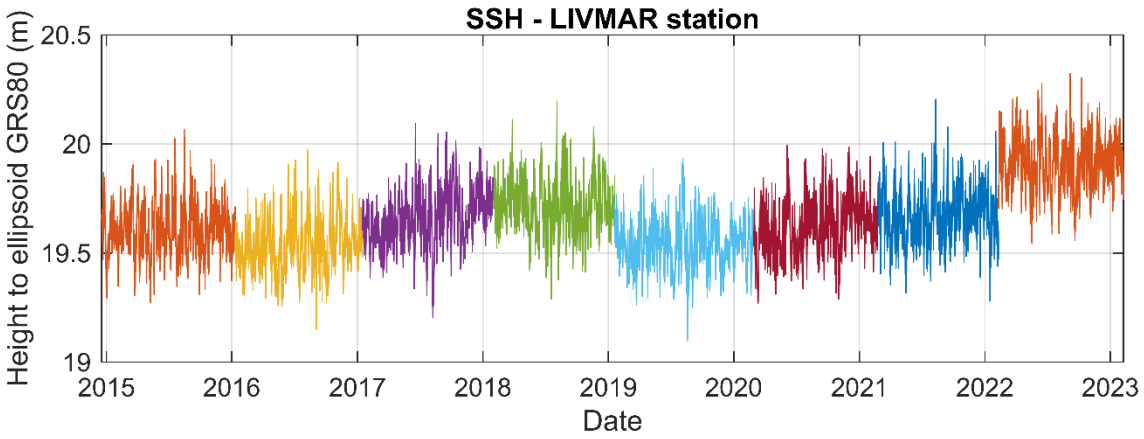


Figure I.5 Sea Surface Height of LIVMAR station. Each colour represents a different record.

- **Test B - Referencing using DAC series**

The second approach used the DAC series as a reference, as it provides continuous records that closely reproduce the short to medium-term variability of tide gauge observations once tidal and atmospheric components are filtered. This similarity enables the estimation of relative biases between fragmented sea level records and their subsequent adjustment to a common reference frame, despite not constituting an absolute datum. It should be noted that in these tests the temporal trend of the series was taken into account, whereas in the Chapter 5 the analyses were performed without considering the trend.

Biases were calculated using the first or last two days of each record, which were then used to adjust the series to the DAC. Although this procedure produced a more consistent result than the first methodology, the SLA records still deviated from the DAC during the initial three years, and the merged series displayed an exaggerated long-term trend. For these reasons, this methodology was also discarded (**Figure I.6**).

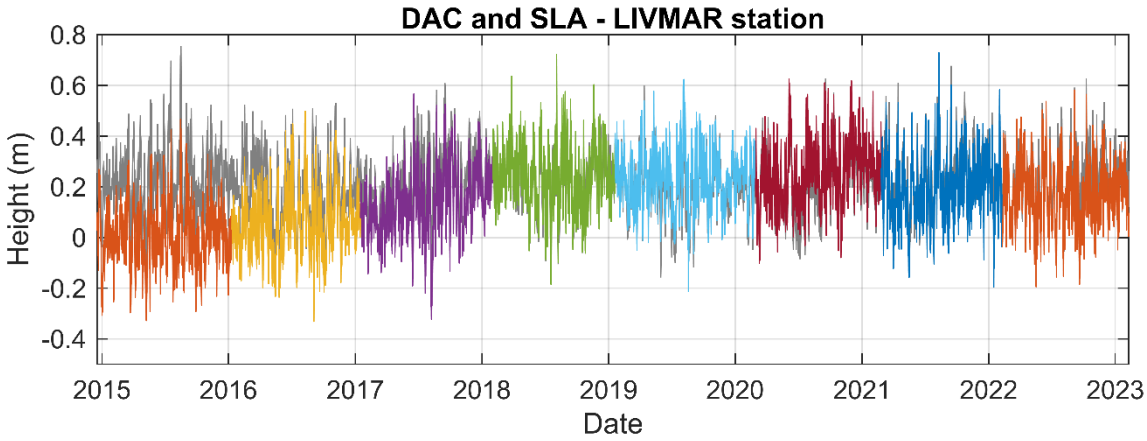


Figure I.6 DAC correction serie (grey colour) and SLA records (different colours).

Comparative Analysis of SLA from Copernicus and GPOD Altimetry Products

Prior to the use of data from the Copernicus platform, Sentinel-3A and Sentinel-3B Level-2 altimetry data were obtained from the ESA Earth Console Parallel Processing Service (P-PRO, https://ui-ppro.earthconsole.eu/). The retracking procedure followed the SAR Altimetry Mode Studies and Applications (SAMOSA++) model (Dinardo et al., 2021), and the resulting product provided sea level measurements at a frequency of 20 Hz.

As the temporal coverage of the study was extended to 2024, the datasets retrieved from this platform for 2023 and 2024 exhibited anomalies that remained unresolved during the preparation of this thesis. For this reason, all datasets were subsequently downloaded from the Copernicus platform, as described in Chapter 5.

To evaluate the robustness of the two sources, both datasets were compared over overlapping periods. For Sentinel-3A, the comparison covered the interval between 19 November 2017 and 6 October 2021, comprising 129 cycles, while for Sentinel-3B the interval spanned from 12 January 2019 to 1 October 2022, comprising 100 cycles. Root mean square errors (RMSE) were calculated for these coincident time frames.

Using the same processing parameters as in Chapter 5 (M = 9; 5% SWH), the standard deviation of differences (SDD) between altimetry and tide gauge records was assessed for both Copernicus and GPOD datasets. For Sentinel-3A, the results are consistent across the two sources, with SDD values of 6.7 cm for Copernicus and 6.2 cm for GPOD, yielding only a minor difference of 0.5 cm. In contrast, for Sentinel-3B, a more pronounced discrepancy is evident: Copernicus reports an SDD of 8.4 cm, while GPOD achieves a considerably lower value of 4.8 cm, corresponding to a difference of 3.6 cm. This suggests that while both datasets provide comparable performance for S3A, GPOD clearly offers improved consistency for S3B, likely reflecting differences in their respective processing approaches.

Appendix II

Curriculum Vitae

Olga Luengo Sánchez

ORCID: 0000-0002-2632-0649

Publications in Indexed Journals

- Luengo-S, O., De Biasio, F., Bruno, M., Vignudelli, S., Berrocoso, M., & Gómez-Enri, J. (2025). Assessment of satellite altimetry accuracy (Sentinel-3A/B) with in-situ sea level data at Livingston Island, Antarctica. *Advances in Space Research.* https://doi.org/10.1016/j.asr.2025.12.088
- Luengo-S, O., Rosado, B., Jiménez-Morales, V., De Gil, A., Gómez-Enri, J., Bruno, M., & Berrocoso, M. (2025). Long-term seawater temperature records at Livingston and Deception Islands, Antarctica. *Frontiers in Marine Science, 12*. https://doi.org/10.3389/fmars.2025.1566852
- Luengo-S, O., Bruno, M., Gómez-Enri, J., & Berrocoso, M. (2025). Meteotsunamis triggered by the Hunga Tonga-Hunga Ha'apai eruption in Livingston and Deception Islands, Antarctica: aliasing, generation place and importance of the water body geometry in determining their amplitude and time–frequency behaviour. *Bulletin of Volcanology, 87(6).* https://doi.org/10.1007/s00445-025-01831-2

Publications in Non-Indexed Journals or Similar

- O. Luengo, J. Benavente, B. Rosado, A. De Gil & M. Berrocoso. Is the Gabriel de Castilla Antarctic Base threatened by coastal erosion? In: Garcia, C., Gómez Pujol, L., Morán Tejeda, E., Batalla, R.J. (eds). (2018). *Geomorfología del Antropoceno. Efectos del cambio global sobre los procesos geomorfológicos.* UIB, SEG, Palma de Mallorca. ISBN: 978-84-09-04850-2.
- O. Luengo, J. Benavente, B. Rosado, A. De Gil & M. Berrocoso. Is the Gabriel de Castilla Base (Deception Island, Antarctica) under erosion risk? In: Rubio, B., Bernabeu, A. M., Rey, D., Varela, R., González-Castro, B., Pedrol, N., Mohamed, K.J. (eds). *Abstracts Volume VI International Symposium on Marine Sciences*, June 2018. University of Vigo. ISBN: 978-84-8158-788-3.

Conference Contributions

- Poster: Luengo-S, O., Bruno, M., Rosado, B., de Gil, A., Gómez-Enri, J. & Berrocoso, M. *Sea level and underwater temperature series at Livingston and*

Deception Islands (Antarctica, 2015-2022). X Polar Studies Symposium, Salamanca, 2024.

- Poster: Luengo-S, O., Bruno, M., Gómez-Enri, J. & Berrocoso, M. *Analysis of the meteotsunamis triggered by the Hunga Tonga-Hunga Ha'apai eruption arriving in Livingston and Deception Islands, Antarctica.* X Polar Studies Symposium, Salamanca, 2024.
- Poster: Luengo-S, O., Gómez-Enri, J., Bruno Mejías, M. & Berrocoso Domínguez, M. (2023). *Towards a long-term sea level ground-truth dataset in Antarctica. Validation of Copernicus Sentinel-3B altimetry data.* XXVIII IUGG General Assembly, Berlin. https://doi.org/10.57757/IUGG23-2335
- Oral: *Analysis of the meteotsunamis generated by the Hunga Tonga-Hunga Ha'apai eruption recorded at Livingston and Deception Islands (Antarctica).* VIII Scientific Symposium of Marine and Environmental Science Students, Faculty of Marine and Environmental Sciences, University of Cádiz, 2023.
- Oral: O. Luengo, B. Rosado, A. de Gil, P. Barba & M. Berrocoso. *Analysis of tidal series of Deception and Livingston Islands (Antarctica).* International Conference on Time Series and Forecasting (ITISE 2022).
- Oral: O. Luengo, B. Rosado, A. de Gil, P. Barba & M. Berrocoso. *Analysis of underwater temperature series of Deception and Livingston Islands (2012-2022, Antarctica).* ITISE 2022.
- Oral: O. Luengo, J. Benavente, B. Rosado, A. De Gil & M. Berrocoso. *Is the Gabriel de Castilla Antarctic Base threatened by coastal erosion?* XV National Geomorphology Meeting, Palma de Mallorca, 2018.
- Poster: O. Luengo-Sánchez, M. Bruno & M. Berrocoso. *Methodology for correcting jumps in sea level records: an application to Deception and Livingston Islands (Antarctica).* Young Marine Researchers Congress, Cádiz, 2018.
- Poster: O. Luengo, B. Rosado, A. de Gil, M. Berrocoso, J. Gómez-Enri & M.B. Mejías. *Establishment of tidal series in Deception and Livingston Islands (Antarctica).* SCAR Open Science Conference, 2022.
- Poster: O. Luengo, B. Rosado, A. de Gil, M. Berrocoso, J. Gómez-Enri & M.B. Mejías. *Study of water temperature in Deception and Livingston Islands (2015-2021, Antarctica).* SCAR Open Science Conference, 2022.

Teaching Collaboration

- Physical Oceanography (BSc in Marine Sciences, 44h)

- Geographic Information Systems and Remote Sensing (BSc in Marine Sciences, 45h; BSc in Environmental Sciences, 15h)

Research Stays / Summer Schools

- Visiting Researcher, National Research Council – Institute of Polar Sciences (CNR-ISP, Mestre – Venice, Italy). October–December 2024.
- TU Delft – IMAU – Deltares, Summer School: *Sea level change: evidence, challenges and policy* (29/08/2022 – 02/09/2022).

Oceanographic Campaigns

- Spanish Antarctic Campaign 23/24
- Spanish Antarctic Campaign 18/19
- Spanish Antarctic Campaign 17/18
- Oceanographic campaign (July 2017). Project *Carbon cycle and greenhouse gas fluxes in the Gulf of Cádiz* (CTM2014-59244-C3-1-R).

Research Contracts

- PhD thesis in Earth and Marine Sciences, University of Ferrara & University of Cádiz (2022 – ongoing).
- Chapter VI Research Contract – Department of Astronomy, Geodesy and Cartography, University of Cádiz (2021/2022).
- Youth Guarantee Researcher – Department of Applied Physics, University of Cádiz (2019/2020).
- Youth Guarantee Technical Support – Department of Applied Physics, University of Cádiz (2017/2018).

Languages

- English: C1 – certified by Aptis and University of Cádiz.
- Italian: B2 – certified by University of Cádiz.

Higher Education

- Master's Degree in Teacher Training, Rey Juan Carlos University (2020/2021).

- Master's Degree in Oceanography, University of Cádiz (2017/2018).
- BSc in Marine Sciences, University of Cádiz (2010/2015).
- BSc in Environmental Sciences, University of Cádiz (2010/2015).

Courses and Science Outreach

- *Prevention of suicidal behaviour and emotional management*, University of Cádiz (5 h).
- Course *Zotero: an open-source reference management tool*, University of Cádiz (25 h).
- Course *Open and reproducible science: introduction to Git and GitHub*, University of Cádiz (5 h).
- Course *Occupational risk prevention – basic functions*, Quirón Prevención (50h).
- *Health and safety in the workplace – general training*, CNR & University of Urbino Carlo Bo (4 h).
- *Virtual information session on open science practices*, University of Cádiz (1h).
- *Users' workshop of the European Coastal Flood Awareness System* (7 h).
- Seminar *Working at the limit: thermodynamics and optimality of the Earth System*, Prof. Axel Kleidon (Jena University, Germany).
- Webinar *Skills to turn problems into opportunities and evaluation methods using creative thinking*, European University of the Seas (SEA-EU).
- *Your City from Space. The Earth Observation Programme: Copernicus*, University of Cádiz.
- Participation in *Aerospace Pedagogical Innovation Project* activities, University of Cádiz (45 h).
- Speaker at *Pint of Science Festival Spain*, 2018.
- Participant in *Climate Change and Sea Level Rising Seminar,* La Salle Buen Consejo School of Puerto Real (Erasmus+ Programme, 2021).
- Volunteer at *European Researchers' Night*, Cádiz, 2017.

Appendix III

Articles already published

Impact factor and quartile of the journal citation reports (SCI and/or SSCI)

I) Article title: *Assessment of Satellite Altimetry Accuracy (Sentinel-3A/B) with In-Situ Sea Level Data at Livingston Island, Antarctica*

Journal: Advances in Space Research

Publication date: 27 December 2025

DOI: https://doi.org/10.1016/j.asr.2025.12.088

Impact factor and Quartile: According to the results published for the year 2024 (as the information for 2025 is not yet available), the journal has an impact factor of 2.8 and is classified in quartile Q1.

II) Article title: *Long-term seawater temperature records at Livingston and Deception Islands, Antarctica*

Journal: Frontiers in Marine Science

Publication date: 15 May 2025

DOI: https://doi.org/10.3389/fmars.2025.1566852

Impact factor and Quartile: According to the results published for the year 2024 (as the information for 2025 is not yet available), the journal has an impact factor of 3 and is classified in quartile Q1.

III) Article title: *Meteotsunamis triggered by the Hunga Tonga-Hunga Ha'apai eruption in Livingston and Deception Islands, Antarctica: aliasing, generation place and importance of the water body geometry in determining their amplitude and time–frequency behaviour*

Journal: *Bulletin of Volcanology*

Publication date: 24 May 2025

DOI: https://doi.org/10.1007/s00445-025-01831-2

Impact factor and Quartile: According to the results published for the year 2024 (as the information for 2025 is not yet available), the journal has an impact factor of 3.2 and is classified in quartile Q2.